

Department of Precision and Microsystems Engineering

A proof-of-concept on Adaptive Control for High-Speed Atomic Force Microscopy

Stefan van der Maarel

Report no	: 2022.080
Coach	: Jacques Noom
Professor	: Gerard Verbiest, Carlas Smith
Specialisation	: High-Tech Engineering
Type of report	: Master thesis
Date	: December 5, 2022

A proof-of-concept on Adaptive Control for High-Speed Atomic Force Microscopy

by

Stefan van der Maarel

to obtain the degree of Master of Science
at the Delft University of Technology,
to be defended publicly on Friday December 9, 2022 at 13:30 PM.

Student number:	4443314	
Project Duration:	September, 2021 - December, 2022	
Thesis Committee:	Ir. J. Noom,	TU Delft, Daily Supervisor
	Dr.Ir. G.J. Verbiest,	TU Delft, Daily Supervisor
	Dr.Ir. C.S. Smith,	TU Delft, Supervisor
	Dr.Ir. F. Alijani,	TU Delft, External Member

Faculty: Faculty of Mechanical, Maritime and Materials Engineering (3mE), Delft

An electronic version of this thesis is available at <http://repository.tudelft.nl/>

Acknowledgement

It would undoubtedly have been impossible to complete this project without the help of my supervisors, family, and friends.

I would like to thank my supervisors Jacques, Gerard, and Carlas for the help they provided throughout this year. I enjoyed the weekly meetings where I learned a lot and I felt motivated when things didn't go my way but eventually could turn them in my favor. Furthermore, I want to thank my family and friends for their motivation and informal conversations.

Stefan van der Maarel

Abstract

The Atomic Force Microscope (AFM) is a microscope introduced by Binnig and Quate in 1986. It was based on the combination of scanning stylus microscopy and a stylus profilometer that contains a sharp probe that touches the surface with ultrasmall forces. Research had been done to improve the scan speed, resulting in High-Speed Atomic Force Microscopy (HS-AFM). During literature research, there is found that parachuting is a common problem within HS-AFM. After that, there is investigated how to improve the control of HS-AFM by decreasing the effect of parachuting. As a result, an adaptive scan speed is proposed to overcome the bottleneck for achieving higher performance in terms of image quality and average scan speed. The following research question has been taken into consideration: *How can a variable scan speed decrease the effect of parachuting and thereby improve the spatial resolution for high-speed atomic force microscopy?* To answer this question, a model has been made in Matlab that describes the dynamics of the AFM together with an LIA filter and PI controller. There has been accounted for the initial step response and two different types of ground truths are defined. A detection algorithm is designed that selects two maxima on a mixed signal where the first and second derivatives are multiplied. A parameter d_{adap} is defined which sets up a distance on the sample that is scanned at a slow scanning speed of $10\mu\text{m/s}$, representing a trade-off between robustness (large d_{adap}) and efficiency (low d_{adap}). Concerning the simulation results, there has been accounted for the step response and performance curves are shown for $d_{adap} = 1, 2, \text{ and } 4\text{nm}$. The detection algorithm has a high repeatability of 97.1% for the uphill events, and 93.6% for the parachuting events. The accuracy of the detection algorithm turned out to have a maximum deviation of one signal period, which has been partly accounted for within the controller. A description is written on how to implement this method in practice, for instance at the JPK Nanowizard at the TU Delft. To conclude, the proof-of-concept of the Adaptive Raster Scanning method shows a large potential that is undoubtedly interesting to perform further research into. It decreases the effect of parachuting severely while enhancing the total same scanning time. There can thus be said that the proof-of-concept on implementing a variable scan speed decreases the effect of parachuting and thereby improves the spatial resolution up to a factor of 9.5.

This method is versatile as well since it is applicable to different shapes such as a circle. An improvement on this method would be to define the detection algorithm based on the RMS value because more events can be measured and the lateral resolution might decrease. The next step would be to perform experiments to see whether this proof-of-concept works as well in reality.

Contents

1	Introduction	4
2	HS-AFM working principle	5
3	Problems and limitations	7
3.1	Noise in the optical detection system	7
3.2	Parachuting	7
3.3	Drift	9
3.4	Hysteresis	10
3.5	Force limitations and nonlinearity	11
3.6	Resolution restrictions	12
3.6.1	Vertical resolution	12
3.6.2	Lateral resolution	13
3.7	Bandwidth limitations	13
3.8	Scan speed limitation	14
3.9	Discussion	15
4	Control methods	17
4.1	Conventional methods	17
4.2	Experimental methods	17
4.2.1	Active Q-control	17
4.2.2	Dynamic PID Control	18
4.2.3	Feed-forward Compensation	18
4.2.4	Multifrequency control	18
4.2.5	Discussion	20
5	Project proposal	23
5.1	Research Question	23
6	Modelling the AFM	24
6.1	Cantilever's dynamics	24
6.2	Input signal \mathbf{u}_c	25
6.3	tip-sample force \mathbf{F}_{ts}	25
6.4	Z-scanner	25
6.5	Lock-In Amplifier	26
6.6	Controller	27
6.7	Imaging	27
6.8	Scanning direction	28
6.9	Accounting for the Step Response	30
6.10	Sample - Ground Truth	31
6.11	Validating the model	32
7	Implementing the Adaptive Scan	33
7.1	Conventional forward scan at very high speed	33
7.2	Designing the Detection Algorithm	33
7.2.1	Implementing the variable speed	38
7.3	Performing the adaptive backward scan	41

8	Simulation results	42
8.1	System Identification on the AFM	42
8.2	Accounting for the Step Response	43
8.3	Results from the Adaptive Raster Scanning Method	45
8.4	Performance Against the Conventional Method	47
8.5	Performance of the detection algorithm	49
	8.5.1 Repeatability	49
	8.5.2 Accuracy	50
8.6	The Circle Scan	54
9	Discussion	55
9.1	Accounting for the Step Response	55
9.2	Performance of the detection algorithm	57
	9.2.1 Repeatability	57
	9.2.2 Accuracy	59
	9.2.3 Limitations	62
9.3	Performance of the Controller	62
	9.3.1 Varying factor d_{adap}	62
	9.3.2 Different sample dimensions	64
9.4	Circle scan	65
9.5	Horizontal drift	67
9.6	Resolution	67
9.7	Simulation time	67
10	Toward Real-life Implementation	68
10.1	JPK Nanowizard	68
10.2	Break-out box	68
10.3	FPGA	68
10.4	Sample	69
10.5	National Instruments and LabVIEW	69
	10.5.1 Hardware	69
	10.5.2 Software	71
11	Conclusions	75
A	Extra formulas from literature	83
A.1	Noise in the optical system	83
A.2	Nonlinear force equation	83
B	Examples of experimental research in practice	84
C	System Identification	86
D	Impulse Response PI controller	87
E	Data points and calculation Ratios	88
F	Repeatability table	89
G	Time Delay table	90

Chapter 1

Introduction

In 1986, Binnig and Quate introduced a new type of microscope that was capable of investigating surfaces of insulators on atomic scale, the Atomic Force Microscope (AFM). The AFM was based on the combination of a scanning tunneling microscope and a stylus profilometer, containing a sharp probe that touches the surface with ultrasmall forces [1]. mAFM was mainly limited by a rather slow time resolution, which made it difficult to study living biological samples on a molecular scale. Therefore, research was done on improving the scan speed, resulting in High-Speed Atomic Force Microscopy (HS-AFM) [2, 3]. HS-AFM was first initiated in 1991 by Barret and Quate who found a technique that increases the scan speed while not having noticeable degradation of the images. This would make it possible to take images in real-time, an absolute milestone [4]. During that decade, a lot of first-stage research has been done in the field of HS-AFM. The main contributors were Quate, Hansma, and Ando who worked parallel with their own research groups on developing HS-AFM [5].

Quate started the research on HS-AFM as a sequel to his research in 1991. Throughout the decade, his research was mainly focused on finding a broader area where AFM could be used. His focus lay on the development of cantilevers, integrated sensors and actuators [6, 7, 8, 9].

After that, Hansma's and Ando's research groups worked parallel on the design of different types of cantilevers and developing faster scanning methods. Within this decade, Hansma's focus lay primarily on small cantilever design and he managed to image DNA at 0.6 frames per second in 1999 [10, 11, 12, 13]. Ando can be seen as the first to report a complete HS-AFM system in 2001 [14], followed by a second research in 2002 that showed biological macromolecules in action [15]. This system can be seen as the starting point for HS-AFM as it demonstrated the possibilities of measuring biological samples at a fast rate successfully.

In general, current techniques reach a scan speed of 10-15 fps (frames per second), mostly used for studying biological samples. Some studies even reach scan speeds up to 50-60 fps, although it is at the expense of the spatial resolution [16, 17, 3, 18]. In most cases, the mechanical components are not setting the limitations, but the control part. It has always been a consideration between scan speed and resolution, which will be further explained in section 3. Wondering how to improve HS-AFM, preferably both speed and resolution, this is an interesting topic to work on.

As a result, the goal of this literature review is to investigate how the control of HS-AFM can be improved. Improving the control of HS-AFM can have different interpretations, such as higher scan speed, decreased forces on the sample, and better spatial or temporal resolution. For this report, the focus will lay on increasing the scan speed and improving spatial resolution.

First, a description of the HS-AFM working principle will be given. In here, the scanning methodology is explained followed by the modulation and imaging techniques. After that, the different noise sources and limiting factors are explained. By considering different practical examples, one specific problem is chosen to focus on. Next, different control methods are considered that tackle this specific problem. From these methods, a new control method is defined and its potential improvement will be discussed. Then, a project proposal will be set up which contains the research questions. After that, the method is explained for the research project followed by the validation technique that is used to verify the results with the conventional methods. Then, the simulation results are discussed and the real-life implementation via Labview and FPGA. Eventually, the results will be discussed and finally, there will be drawn a conclusion for the general report. At the end of the report, a glossary can be found with the list of acronyms that are used.

Chapter 2

HS-AFM working principle

Most conventional microscopical methods emit a light or electron beam signal through multiple lenses to a sample. This signal hits the sample and is processed via reflection or transmission to form an image. Unlike to these conventional microscopical methods, HS-AFM works by measuring the sample height via a sharp probe on a vibrating cantilever along the surface. It reads the topography by touching the surface, more or less how people would read using Braille. However, instead of sliding along the surface, HS-AFM uses a vibrating signal on the cantilever to tap on the surface frequently - also called the tapping mode. An example of an AFM setup used in tapping mode is shown below in figure 2.1.

For every AFM setup in tapping mode, a small cantilever is present with a small sharp probe at the end which makes contact via a sinusoidal signal with the sample. On the cantilever, a laser beam shines on the endpoint of the cantilever. This laser beam reflects towards a photodiode which compares the incoming signal with a reference that has been set as the excitation signal. The sample stage is actuated by three independent piezo actuators for the x, y, and z direction. The interaction between the tip and the sample results in a certain tip-sample interaction force and a deflection of the cantilever itself. Depending on the sample, limitations can be set on the interaction force by tuning the magnitude of the oscillating amplitude. The deflection of the cantilever changes the incoming signal to the photodiode by the laser beam, causing a phase shift and difference in amplitude [19].

The raw signal from the photodiode will be measured and demodulated via an RMS-to-dc converter to be able to use it for the feedback controller [20]. The most common type of converter to use in tapping mode is a Lock-In Amplifier, which measures the amplitude and phase [21]. After the signal has been processed through the LIA, it is compared with its reference signal or setpoint, the cantilever's excitation frequency. From this, a difference in amplitude is taken which is used as input for the PID controller. The controller is connected with the z-piezo driver to compensate for the deflection of the cantilever as it follows its setpoint. The controller will tune the z-stage such that the cantilever goes to its original amplitude, so it modulates the amplitude.

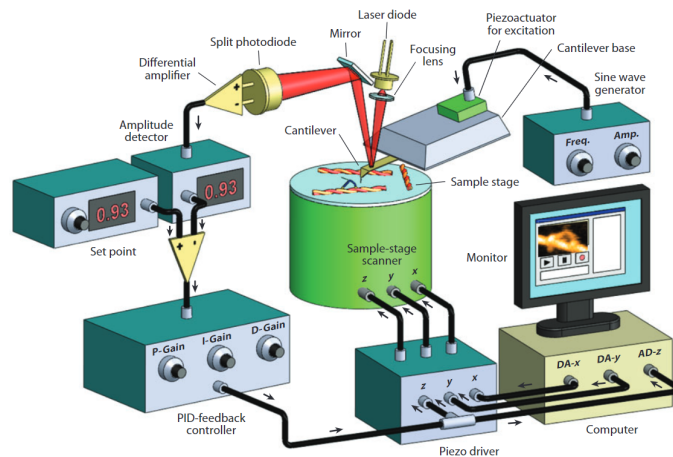


Figure 2.1: Example of an AFM setup made by Ando [19]

After the signals has been demodulated, they must be formed into an image. Following the amplitude modulation technique with the LIA, the signals are processed to a topography via phase imaging [21]. By phase imaging, the phase lag between the excitation signal of the cantilever and its output them the photodiode is monitored. These differences in phase lag are combined with the amplitude signal to form an image.

In the next chapter, the noise sources and limiting factors are explained from which the main problem can be determined.

Chapter 3

Problems and limitations

There are several problems within HS-AFM that influences limitations on the scan speed and spatial resolution. At first, several problems are mentioned such as noise in the optical detection system, drift, parachuting, hysteresis, and nonlinearity of the tapping force. After that, limitations concerning the force, bandwidth, and scan speed are explained.

3.1 Noise in the optical detection system

Measuring the signal from the laser diode, noise is present in the optical detection system which will affect the closed-loop output. It will give an error e_{nor} that is influenced by laser intensity fluctuations, in a lateral direction on the photodiode. Furthermore, there is a friction signal f_{nor} as a result of the first torsional mode, which is in the vertical direction on the photodiode. These errors are visualized below in figure 3.1 below. These errors can be calculated and eliminated (by normalizing them) as well, which is done and its result is given in Appendix A. As both noise factors can be eliminated, a specific type of control method is not necessary [22].

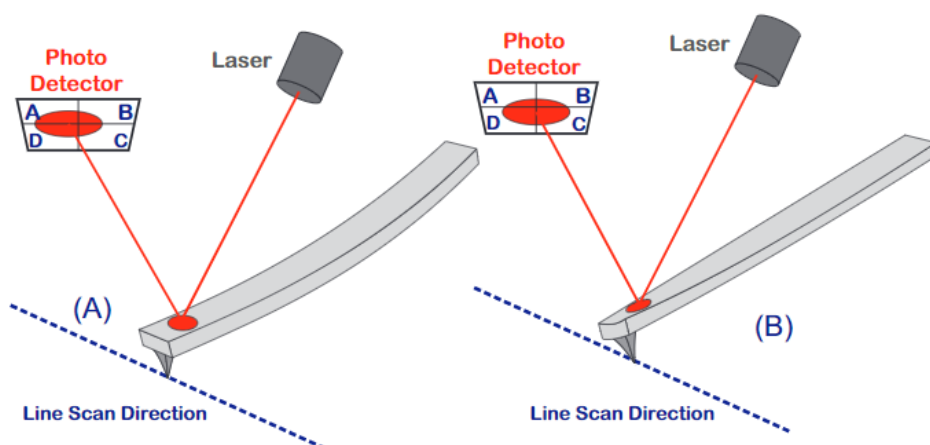
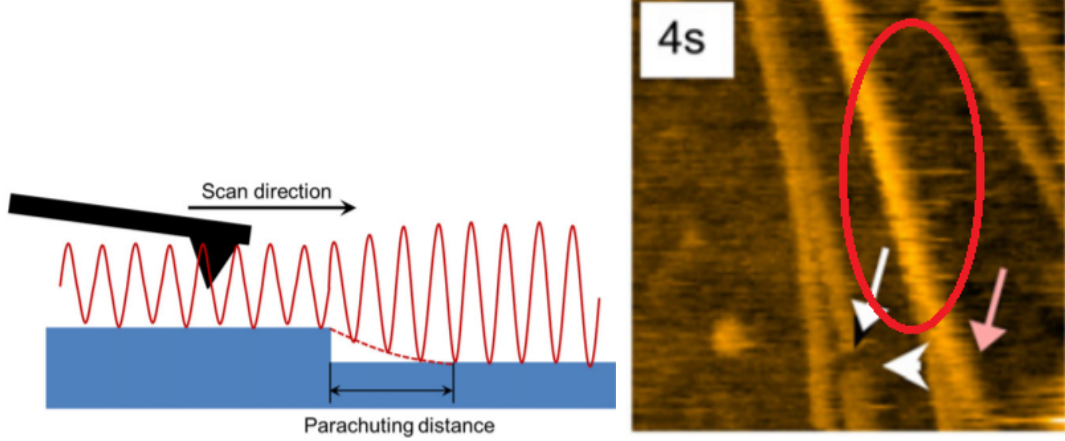


Figure 3.1: Situation A shows the error caused by the laser intensity fluctuations, resulting in an error in the lateral direction of the photodiode. Situation B shows the friction caused by the first torsional mode, resulting in an error in the vertical direction. [22]

3.2 Parachuting

Parachuting is the phenomenon where the probe of the cantilever completely detaches from the sample surface at a steep descending slope of the sample. The feedback controller requires some time to adjust for the increasing amplitude, causing the probe to oscillate towards its free amplitude till the controller adjusts the z-stage to its set point amplitude correctly [23]. This makes it impossible to record the sample topography, meaning that it affects the spatial resolution negatively. From a practical view it can be compared with the Wile E. Coyote effect

[22]. He runs towards a cliff, but it takes some time to fall dramatically. A visualization of the parachuting effect is shown in figure 3.2a, where is seen that the cantilever taps towards its free amplitude till the controller adjusts its gain toward the right sample height. An example of a topography image where parachuting is present is seen below in figure 3.2b.



(a) This shows the effect of parachuting of how the topography is poorly scanned by the cantilever. The scanner 'thinks' it measures a sample height, while this is in practice, not the case. [24]

(b) An example of bad image quality as a result of parachuting. This image is processed from a forward scan where parachuting can only be formed at the right side of the sample as the probe moves from left to right. Parachuting is clearly seen within the red-hatched area. It is recognized by the lighter stripes moving in the right direction of the image. [5]

The probability of parachuting increases for higher scan speeds, as this gives the controller less time to react on steep descending slopes. As it is not possible to record the sample topography during parachuting, a condition is estimated where there is no parachuting at all which is expressed as

$$A_0(1 - r) - h_0 \sin(\theta/2) > 0 \quad (3.1)$$

Where A_0 corresponds to the free oscillating amplitude and h_0 is the maximum sample height. $r = \frac{A_s}{A_0}$ with A_s the cantilever's amplitude set point and the domain of r lie between 0 en 1 as the cantilever can't exceed its free amplitude. Finally, θ corresponds to the total phase delay which will be further discussed in section 3.7.

Considering the control part, it is more interesting to know what time delay the parachuting effect will give, such that there can be compensated for this effect. According to the paper of Ando, [23], the following equation estimates the time delay as a result of the parachuting effect, τ_p (note that f_c is the cantilever resonant frequency, not the feedback frequency):

$$\tau_p = (\tan\beta/\beta - 1)/f_c \quad (3.2)$$

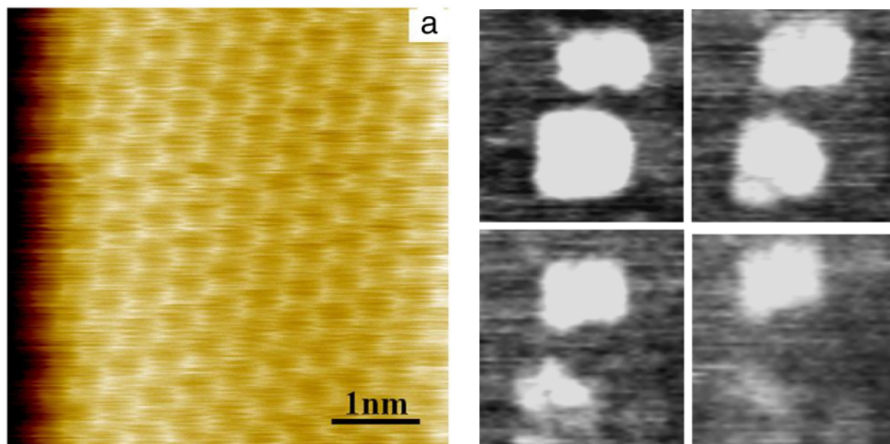
with $\beta = \cos^{-1}[2A_0(1 - r)/h_0 \sin(\theta/2)]$

3.3 Drift

Drift is a phenomenon where the scanner has an uncontrolled movement relatively to the sample. This forms a major problem in AFM, as it causes shifts within the topography of the image. For instance, when applying a line scan on a object, it can turn out in an image that is stretched or skewed as shown by Gan [25]. In tapping mode, the presence of drift in the cantilever-excitation efficiency is quite problematic. Drift-caused changes can be seen as tip-sample interactions on which the controller will react [26]. The main contributors to the drift are instrumental and temperature drift.

Instrumental drift Drift is caused by changes in the instrument, for example, the tolerances of the mechanical components or thermal expansion of the connecting cables. It is difficult to prevent it as many factors are involved [27]. Instrumental drift is usually expressed in a vertical and lateral drift component. Different researches have shown that the effect of instrumental drift in AFM can be reduced by taking higher scan rates [25, 28, 29], which is the case for HS-AFM. An example of instrumental drift is shown in figure 3.3a.

Thermal drift Thermal drift appears when there are temperature differences between the different components of an AFM. This usually happens when there is measured for a longer amount of time, because the components are heated up over time [26, 29, 30]. An example of thermal drift is shown in figure 3.3b.



(a) This image shows the presence of instrumental drift. There are distortions present in the shape across the whole image. Other than for parachuting, instrumental drift shows stripes in both directions causing a complete distortion of the image. There is observed that the drift shows a very random pattern as well, as every distorted molecule is different. This makes it difficult to express it in lateral and vertical drift components. [25]

(b) The effect of thermal drift is made visible by repeating the same passage. The sequence starts from the upper left corner to the right lower corner. A strong reduction of the white areas is seen as more measurements are performed in a row. [31]

Figure 3.3: The presence of instrumental drift (3.3a) and thermal drift (3.3b)

Considering the terminology, the ratio r between the cantilever's amplitude set point and free oscillating amplitude has an influence on the drift as mentioned above. Increasing this ratio would not only worsen the performance of parachuting, but the effects of drift would also increase as well. There can be said that this ratio should thus be lowered. However, this will increase the interaction force between the probe and the sample. All factors should be considered to come up with an optimal value. In most researches, $r = 0.9$ is considered to be most conveniently [5, 23, 26].

3.4 Hysteresis

Hysteresis is the effect that because of the influence of the ferroelectric effect in a piezo driver, or non-local memories, the output displacement and input voltage is nonlinear. [32, 33]. When the input voltage alternately increases and decreases, a certain hysteresis loop is created. This causes a difference between the real and actual output displacement, which is nonlinear. Processing this data, the height information that is obtained cannot be precisely matched, leading to image distortions. Moreover, the hysteresis effect has a memory characteristic as well. This means that the output displacement is not only defined by the value of the input voltage, but also by the history features and change in direction of the input voltage. This effect increases for high-speed scanners [34].

So, there can be said that hysteresis affects its position accuracy and spatial resolution negatively and thus decreases the imaging quality. Especially for HS-AFM, the nonlinear effect of hysteresis plays a more important role since the frequency of the input driving voltage is increased. It affects the spatial resolution by shifting the image along the vertical axis. For instance, it images a square as a parallelogram. An example of hysteresis during an experiment is shown in figure 3.4.

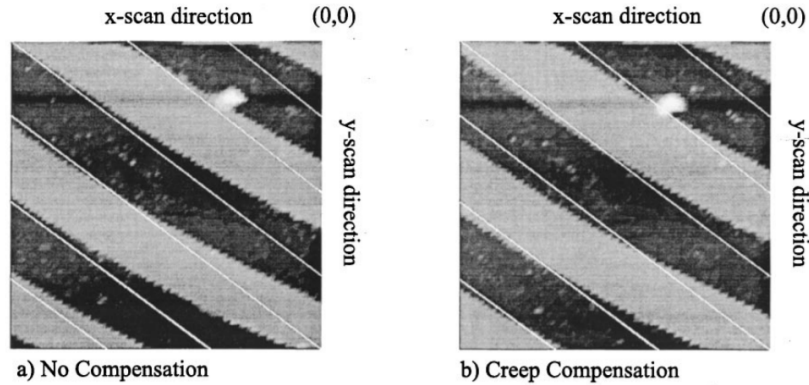


Figure 3.4: The high-scanning probe should follow the white lines. The image is distorted as a result of hysteresis, creep, and vibrations which only gets worse for higher frequencies. The contribution of the hysteresis is the shift of the complete image along a nonlinear curve on the vertical axis. This is shown in the right picture where is only compensated for creep. [35].

Primarily, there are two different types of approaches that describe the hysteresis model, constitutive and phenomenological approaches. The constitutive or microscopic approach is built on the underlying physics of the phenomenon and calculations are based on empirical observations. The phenomenological or macroscopic approach uses mathematics to describe the phenomenon

and does not consider the physics at all [33, 36].

Two different types of controllers are mentioned to improve the positioning accuracy of the lateral scanning by compensating for the hysteresis, feedback control, and feed-forward control. These are derived from the constitutive and phenomenological approaches respectively [37, 33]. This makes sense as the constitutive approach uses underlying physics and empirical observations, which can be used for the next loop inside the feedback control. For the phenomenological approach, mathematics is used to build an inverse of the model for which feed-forward compensation can be used [33]. An example of a feedback control loop for modeling the hysteresis is a Back Propagation Neural Network approach [34]. Hybrid methods are possible as well, where feedback and feed-forward control is combined for modeling the hysteresis. In [37], a dynamic polynomial fitting method is used to generate a hysteresis model of the piezo driver, where based on the inverse a feed-forward controller is built and combined with an intelligent feedback controller.

3.5 Force limitations and nonlinearity

Concerning the interaction between the tip and the sample, it can be useful to know the limitations of these forces to prevent damage to the tip and sample. Tip-sample forces can be deduced into two forces, vertical and lateral forces. The vertical force is meant in general as tip-sample interaction force because this can be used as a control parameter for the cantilever. The lateral forces solely cause torsion modes which are mostly not taken into account for imaging and thus are seen as less relevant. However, the lateral force can be a limiting factor if it hits a steep edge with the end of its tip, causing to damage the tip too. Although, it can be questioned whether there should be taken much attention to this because hitting a steep edge with the end of the tip has a low probability. It would make the cantilever blunt and not destructively broken and useless [22]. Furthermore, Sulchek states that lateral forces are not even exerted between the tip and sample if the tapping frequency of the system is much larger than the raster scan [20].

Considering the theory, different models are built that calculate the tip-sample interaction force. Most of them are deduced from the Derjaguin-Müller-Toporov theory [38], which describes the molecular attraction of a spherical object to a flat surface. From this theory, the Derjaguin-Müller-Toporov model can be directly built to calculate the vertical force. The Kelvin-Voigt model [39] is an example that uses this theory for lateral forces. A different method is used by Pfeiffer [40] to describe these.

Furthermore, there is a strong nonlinearity of the tip-sample interaction forces, which mainly affects the vertical force. This can be seen as a disadvantage for tapping mode HS-AFM with respect to the other modulation techniques as it influences the amplitude, which is the control parameter [41, 42]. The nonlinear behavior is shown in figure 3.5, where the attractive region is caused by Van der Waals' forces and the repulsive region by the Pauli principle [22, 25]. This phenomenon has an influence on the phase shift as well, which was experimentally proven by Nishi [43] and mathematically shown in Appendix A.

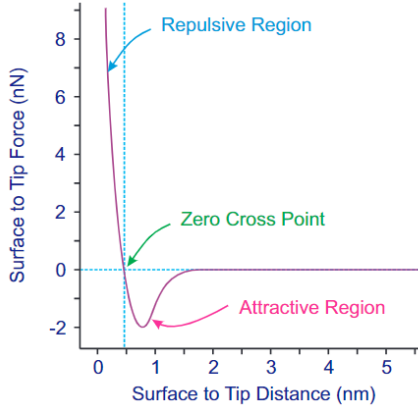


Figure 3.5: The nonlinearity of the vertical tip-sample interaction force [22]

Next, an estimation can be made for the tapping force which is dependent on the mechanical properties of the cantilever, k_c and Q_c , the stiffness and quality factor. Next, it is dependent on the ratio between its free and set point amplitude and the height of the sample. This expression is given below:

$$F_p = (k_c/Q_c) * (A_0 * (1 - r) + h_0 * \sin(\theta/2)) \quad (3.3)$$

3.6 Resolution restrictions

Considering the atomic resolution, it has theoretical restrictions on the AFM topography. The atomic resolution includes a combination of vertical and lateral resolution. This atomic resolution has an influence on spatial resolution as it determines to what extent the molecules can be measured and thus which resolution could be theoretically reached.

3.6.1 Vertical resolution

The vertical resolution of an AFM, or sensitivity, is mainly limited by the thermal noise of the deflection detection system. Other factors will thus be neglected. As you measure the amplitude for a tapping mode HS-AFM, this thermal noise should be minimized to maximize the vertical resolution. For a mainstream optical lever system, the thermal noise for a rectangular cantilever can be expressed as

$$\delta z = \sqrt{\frac{4k_B T}{3k}} \quad (3.4)$$

Where k_B is the Boltzmann constant, T the absolute temperature and k the spring constant of the cantilever [25, 44].

The spring constant can be an important factor in choosing the cantilever. Lowering it would mean less thermal noise but higher forces and vice versa, also shown in equations 3.4 and 3.3. The level of presence of thermal noise can be calculated. This can be used to decide whether it will cause much noise or not, as visually shown in a paper by Fantner et. al [45].

3.6.2 Lateral resolution

The lateral resolution is defined by Gan as the minimum detectable distance between two (infinitely) sharp spikes of different heights [25]. The lateral resolution is mainly limited by the geometry of the tip, so other factors are not taken into account. The expression for the minimum detectable distance, and thus the lateral resolution, can be given as

$$d = \sqrt{2R}(\sqrt{\delta z} + \sqrt{\delta z + \delta h}) \quad (3.5)$$

R corresponds to the radius of the tip of the probe, δh with the relative height between the two spikes and δz with the vertical resolution as mentioned above. Finally, it is important to mention that the dimple depth δz should be larger than the instrumental noise to be allowed to apply this expression [46].

3.7 Bandwidth limitations

The bandwidth of the HS-AFM system can be defined as the maximum frequency at which the output displacement will track a sinusoidal input signal on the cantilever in a satisfactory manner [20].

The main source of bandwidth limitation is caused by the Lock-In Amplifier (LIA). The LIA converts the ac signal into dc by averaging the amplitude of the oscillations. Usually, there are around ten oscillations required for the LIA, otherwise, it would react too sensitively to noise. This means that there is at least a time delay of ten oscillations till the controller knows it has to tune its z-piezo driver. In practice, the LIA is a low-pass filter that has a maximum bandwidth as it requires these ten oscillations. This low-pass filter limits the feedback bandwidth heavily. Furthermore, it results in a loss of information in transient responses as it is based on steady-state regimes. For HS-AFM, transient responses will become a bigger problem when the scan speed is increased. This is because the effective frequency of the sample decreases, thus transient responses will be present more frequently. The controller has less time to adjust to the sample height [20, 47].

The bandwidth of an AFM can be described in a general form which is a function of the time delay as the frequency (in Hz) is simply the inverse of time. The different time delays can be described as τ_0 which contains a phase delay θ that is used as the phase margin in the feedback loop. This phase margin can vary between $\pi/2$ and $\pi/8$, depending on the ratio between the cantilever's and free amplitude and the height of the sample [26]. From this, we get the expression $f_B = \theta/(2\tau_0\pi)$ [19, 20].

τ_0 can be split into multiple time delays that are present within the system. These are the cantilever's τ_c and z-scanner τ_z response time, integral time of error signals in the controller τ_i , parachuting τ_p and an excess part δ that sums the other time delays. The cantilever's response time can be calculated via $\tau_c = Q_c/(\pi f_c)$ where f_c is the resonance frequency and Q_c the quality factor [3]. The z-scanner response time can be calculated according to the same methodology, which will result in $\tau_z = Q_z/(\pi f_z)$. In here, Q_z is the quality factor of the z-scanner and f_z its resonance frequency. The excess part δ can cover different time delays such as the LIA, vibrations, and time delay as a result of the thermal noise as mentioned in section 3.6.

These different time delays can be filled in for τ_0 into the formula given above. Furthermore, it should be incorporated for an additional time delay of $1/(2f_c)$, thus one period, to measure the amplitude of the cantilever. Combining these into the formula of f_B , the following expression can be derived [23, 26]:

$$f_B = \alpha \frac{\theta f_c}{2\pi} / \left(1 + \frac{2Q_c}{\pi} + \frac{2Q_z f_c}{\pi f_z} + 2f_c(\tau_p + \tau_i + \delta) \right) \quad (3.6)$$

with $\tau_i = \kappa h_0 \sin(\theta/2)/(A_0 f_c)$ and $\tau_p = (\tan\beta/\beta - 1)/f_c$

Where α is a factor that is related to the phase compensation effect by the D component of a PID controller, or phase compensator. κ is a proportional coefficient and θ the phase delay of the feedback operation.

3.8 Scan speed limitation

In general, the scan speed is dependent on the cantilever's frequency and wavelength λ , giving $V_s = f_c \lambda$. In order to find the maximum possible scan speed, there are restrictions on the frequency as it is limited by the bandwidth [23]. Also, it should be corrected for the different time delays mentioned in section 3.7 which results in a maximum phase delay. Eventually, the following expression can be derived for the maximum possible scan speed:

$$V_s^{max} = \frac{\theta_{max}}{(\pi/4)} \times \lambda f_B \quad (3.7)$$

Where θ_{max} is the maximum possible phase delay as a result of all time delays, λ is the wavelength and f_B the feedback frequency or bandwidth [19].

A different, more specified, approach was formed by Sulcheck [20]. He defined a formula for the maximum scan speed mainly based on *preventing parachuting*. At first, it will follow the condition where the cantilever's amplitude will saturate at its free amplitude. After that, it is corrected for the geometry of the tip which results in the following equation:

$$V_s^{max} = \Delta a \tan(30)/T \quad (3.8)$$

with $\Delta a = (A_0 - A_s)(1 - e^{-Tf_c\pi/Q_c})$

where T corresponds with the period of the oscillation, A_0 and A_s with free amplitude and set point amplitude respectively. f_c is the cantilever's frequency and Q_c its quality factor. Δa can be interpreted as the amplitude increase as a function of the period of the oscillation while incorporating the slow transient response for parachuting.

Concerning the forces acting on the sample as mentioned in section 3.5, there can be said that there is a certain limit for the scan speed. This is because the ratio between the tapping frequency and scan speed should be high enough such that no lateral forces will be exerted [20]. The consequence can be that the tip will break which results in a poor measurement.

In some research, the scan speed is referred to as the imaging rate. The imaging rate or inverse for time resolution [2], has a theoretical limit that can be used to compare the maximum possibilities of different methods and thus to what extent they have already been explored. The imaging rate is dependent on the size of the sample and the scan speed. The equation for the maximum possible imaging rate, expressed in frames per second (fps), is given by

$$R_{max} = 2\theta_{max}\lambda f_B / (\pi W N) \quad (3.9)$$

Where θ_{max} is the maximum possible phase delay in the feedback controller, λ the wavelength, f_B the feedback frequency (given in section 3.7), W the scan size in the x-direction and N the number of scan lines. This means that for increasing the imaging rate, either the scan speed should be increased, or scanning the sample field should be done in a more efficient way [19].

3.9 Discussion

As mentioned in the introduction, the main goal is to find a method to improve the scan speed and spatial resolution. Observing equation 3.7, there is seen that the scan speed is directly dependent on the bandwidth. Increasing the bandwidth will immediately increase the maximum possible scan speed. For the equation of the bandwidth in 3.6, the cantilever's and z-scanner characteristics and different time delay components are involved. Increasing the bandwidth implies that the resonance frequency f_c and the quality factors Q_c and Q_z should be increased. The time delay components τ_p , τ_i and δ should be decreased. Improving the spatial resolution would imply lowering the thermal noise and minimum detectable distance. Following equations 3.4 and 3.5, this would imply procedures such as increasing the cantilever's stiffness and decreasing the radius of the tip of the probe

As mentioned in the introduction, the main goal of this research is to improve the *control* of the AFM. Improvements in the characteristics of the cantilever and z-scanner will thus not be taken into account. Improvements on the real quality factors Q_c Q_z , cantilever's stiffness, and radius of the tip are therefore not an ideal solution. Concerning the improvements for the spatial resolution, this must be done in a different manner which can not be calculated via the theory mentioned above. This will become more clear in the next section.

The resonance frequency f_c can be increased using a higher resonance mode, or via a multi-frequency approach that combines the first and higher order resonance modes [48]. The time delay components τ_p , τ_i , and δ can be decreased as well. The components that match these are parachuting, integral operation in the PID controller, and an excess part that includes hysteresis, drift, and the Lock-In Amplifier.

Concerning drift, in section 3.3 is shown that instrumental drift is dependent on the scan rate. For higher scan rates, the effect of drift will decrease. Thermal drift is time-dependent, which is more applicable in investigating temporal resolution instead of spatial resolution [49]. Therefore, drift will not be taken into account as a potential parameter to work with.

It is useful to know which parameters can help with the scan speed theoretically. For the spatial resolution, it might even be more interesting to see what can be observed from current papers. Logically, only hysteresis and parachuting can be analyzed. The time delay caused by the integral operation in the PID controller and Lock-In Amplifier can't be visualized clearly within the image. This is because bad control is the cause of patterns of parachuting, drift, and hysteresis in an image.

In order to find practical 'proof' to choose a certain problem as the main topic, a collection is made of experimental results with their year of publication. There is only focused on what can be observed from the image itself which should not require any background information from the paper. Some useful examples are shortly depicted below as well. These give an insight into the specific problem that returns in most experiments. For consistency, the scan speed has been left out of consideration as the variation in scan speeds couldn't be deduced for every paper. Finally, there is assumed that the researchers tried to publish their best results. In order to have recent results, papers are chosen with a publication date after January 2019. One example is elaborated below and the remaining examples can be found in Appendix B. The reason to choose this example is that it shows the topography at different scan speeds, which can give a good insight into how the scan speed and spatial resolution are influencing each other for this measurement.

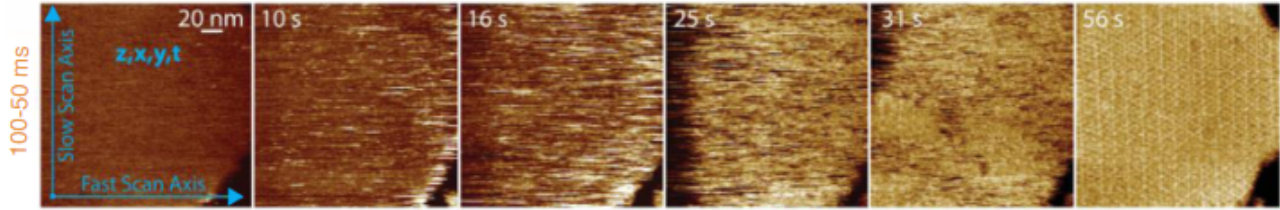


Figure 3.6: (2019) Use of different scan speeds by Heath et. al [49]. This image shows scan speeds from fast to slow starting from the left side towards the right side. Starting from the first pictures, parachuting and hysteresis are mostly present as these are dependent on the scan rate. The scan rate is too fast for the AFM, resulting in images with a topology that is mostly equal to the largest amplitude that is present in the image, which indicates parachuting. Another reason that parachuting seems to dominate is that the image does not seem to skew to the right which would indicate hysteresis. For slower scan rates, the quality of the spatial resolution gets better whereas for the last picture parachuting almost disappeared. There can be assumed that this slow scan rate is definitely lower than explained in equation 3.8, as the parachuting condition is met. It is difficult to see the effect of hysteresis and thermal drift inside this picture, as it is rather small and thus not detailed. However, there can be assumed that thermal drift will become more dominant as the scan rate decreases which increases the total time of a scan.

From the different examples in Appendix can be concluded that parachuting is the main problem in HS-AFM. This effect was dominantly present in the different examples and is strongly dependent on the scan rate. Thus, there may be chances for improvement regarding parachuting which will be further discussed in the next section.

Chapter 4

Control methods

Within this section, the current conventional method is presented and experimental control methods are discussed based on what is the biggest problem as discussed in section 3, parachuting. First, the level of improvement is indicated and quantified. After that, these different control methods are weighed up against each other and compared thoroughly. A new method will be presented based on potential improvement, level of simplicity, and practical feasibility.

4.1 Conventional methods

The most conventional method that is used by the industry is the PI and PID feedback controller. The PID controller tends to be more convenient as its derivative action gives a relatively faster response as it can compensate for the feedback delay. However, it can produce mechanical vibrations for higher frequencies. Thus, the resonant peaks at high frequencies should be lowered. In tapping mode HS-AFM, it is usual to control the Z-stage with a fixed gain that can be freely chosen beforehand [50, 51, 23, 5]. An example of a commercial but advanced controller is the SIM960, an analog PID controller designed by Stanford Research Systems. This controller can reach a bandwidth of 100kHz [52, 53].

4.2 Experimental methods

There has been solely focused on control solutions that cover parachuting. These are narrowed down into four aspects on which improvements can be made: the cantilever and X, Y, and Z sample stages. Furthermore, these researches are set up against each other to discuss their differences and to what extent they cope with parachuting. The main outcome is mainly mentioned for the bandwidth and certain errors. Considering the spatial resolution, most papers do not use quantification methods to show their improvements in practice.

4.2.1 Active Q-control

Active Q-control is a technique where an additional feedback loop is used for the cantilever oscillation signal. The effective quality factor is increased by using a phase lag signal from the feedback controller. Adding a phase lag signal of 90 degrees proves to maximize the Q enhancement and is thus called the self-excitation term. The result is that the effective frequency remains the same, but the effective quality factor is increased. This affects the amplitude of the signal by damping it more severely. Since the first research in 2000, this method became very effective in actively damping the transient response after the probe hit a steep uphill region which reduced time delay and improved spatial resolution [54, 55].

Later research in 2019 showed the possibilities of attenuating parachuting for higher scan speeds [56]. Equation 3.8 shows the influence of the quality factor on the scan speed where the slow transient response for parachuting is incorporated. It includes that a decrease in the quality factor leads to an increase in the amplitude. A higher amplitude causes the probe to touch the surface sooner, thus the time delay caused by parachuting decreases. This can be used to either increase the scan speed or improve the spatial resolution. They managed to decrease the effective Q factor of the cantilever from 177 to 15, which decreased the time delay caused by parachuting

by 40% [56]. After that, Kaveh et. al managed to use active Q-control on an FPGA-based setup where the quality factor was reduced from 268 to 81.7. They showed a reduction of parachuting time by around 40% as well [57].

4.2.2 Dynamic PID Control

The dynamic PID controller is a design for tapping mode AFMs by Kodera et. al which is published in 2006 [26]. The main goal of this method is to lower the interaction forces with the sample by actively tuning the amplitude via the Z-stage. The controller contains a feedback loop with a dynamic operator inserted which controls the Z-stage. For the dynamic operator, a parameter is chosen between the cantilever's set point and free amplitude. This causes an increase controller's gain when parachuting occurs, resulting in less presence of parachuting for the images. Following equation 3.6, a decrease in time delay caused by the parachuting effect gives an increase in feedback frequency which can be measured. This approach is combined with a drift compensation technique to cope with the relatively high drift in the cantilever-excitation efficiency. This results in a maximum achieved frequency of 70kHz in water with an increase of 30%-40% for the different measurements with $r = 0.9$. A disadvantage is an interaction with steep uphill regions which promotes overshooting and thus creates parachuting.

This technique has been further developed towards digitally controlled analog PID controllers, for instance by Dukic et. al [52] and the SIM960 as mentioned above.

4.2.3 Feed-forward Compensation

Feed-forward compensation is a control technique invented by Schitter et. al in 2004 [51, 50]. It contains a 2-DOF controller that consists of two controllers: a conventional PID feedback controller and a feed-forward open-loop controller. The feed-forward controller tracks the sample to the previously recorded scan line by reading out the X and Y stage. It compensates both scanning directions for its dynamic behavior which causes mechanical resonances. Next, this feed-forward compensation is combined with the feedback controller to send one control signal to the Z-stage. Results are that lower error signals are achieved leading to a higher possible bandwidth [23]. In 2006, Uchihashi et. al used this method for HS-AFM where they achieved to reach better image quality for scanning rates up to 60ms/frame. For $r = 0.98$, the bandwidth increased from 9 kHz to 51kHz. For $r = 0.8$, the bandwidth increased from 31 kHz to 70 kHz. In light of these results, there can be said that for $r = 0.9$, the bandwidth would have been increased by at least 150%. Although, a disadvantage as a result of the feed-forward compensation is the steep rising edge that occurs in the topography [58]. Considering parachuting, this is actually an advantage as the effect of parachuting is attenuated by such a steeper rising edge, while still having an overall error reduction of 25% [23]. Watanabe et. al showed in 2013 [59] that the use of feed-forward control is most useful in wide-area scanning. This has to do with the possibility to eliminate errors of the strong non-linearities of the X and Y piezo actuators which are caused by hysteresis.

4.2.4 Multifrequency control

Another interesting controlling method is done by using higher resonance frequencies of the cantilever, mostly via multifrequency methods [48]. A direct influence of the cantilever's frequency on the presence of parachuting is shown in equation 3.2. There can be seen that the time delay caused by parachuting is proportional to the cantilever's frequency which sounds promising. Considering equation 3.6, it even has a much stronger effect on the bandwidth frequency itself

which can contribute to higher scan speeds. The control loop itself remains unchanged, which means that a modified PID controller for multiple harmonics is used to control the Z-stage. In 2007, research has been done by Preiner et. al on higher harmonic AFM [60]. Preiner used the second harmonic which resulted in a much better lateral resolution, which can be theoretically proved from equation 3.5.

Using higher harmonics, the system is attenuated in a nonlinear manner which strongly influences the deflection and characteristics as well. For instance, when the quality factor increases proportionally with the cantilever's frequency, the force constant will have a quadratic growth [48]. Following equation 3.3, the force will thus increase in proportion with the frequency. A big advantage of multifrequency control is the ability to not only gather information about the topography, but also mechanical, magnetic, and electrical properties. The nonlinearity and lower sensitivity of the higher harmonics make it more difficult to obtain the topography. For this reason, the first harmonic is mostly used for the topography, and higher harmonics for the remaining properties. This still limits the potential maximum scan speed as the slowest resonance frequency is used for the topography.

In practice, multifrequency control is used for soft (biological) samples and not specifically for fast(er) scanning [48, 61]. Mainly because it can gather other properties from the sample as well. However, in 2021, Gisbert et. al performed a bi-modal approach on which they reached a scan speed of 200 ms/frame [16]. Within this research, he investigated the early stages of collagen growth which also required a scan speed optimization.

4.2.5 Discussion

In order to come up with a new methodology to control the system, the current experimental techniques should be reflected on. This is done by making an overview in table 4.1 where their main characteristics and effect on parachuting are given.

Grading scheme of current solutions vs. problems and limiting factors				
<i>Control techniques</i>	Control output	Control input	Effect on parachuting	Particularities
<i>Active Q-control</i>	Cantilever	Photodiode	+++	Input of X and Y stage used for clocking Use of multiple harmonics
<i>Dynamic PID Control</i>	Z-stage	Photodiode	+++	
<i>Feed-forward Compensation</i>	Z-stage	Photodiode X and Y stage	++	
<i>Multifrequency Control</i>	Z-stage	Photodiode	+	

Table 4.1: Table in which the different control solutions for parachuting are set against each other.

There is seen that the control output is either the cantilever's excitation signal or the Z-stage piezo. For the input, we see the photodiode as general input, and for the feed-forward approach an additional X and Y stage for clocking. Considering the effect on parachuting, there is seen that Q-control and Dynamic PID perform the best. This is mainly because these methods were more specific on tackling parachuting. The feed-forward and multifrequency control technique had other design parameters in which parachuting was covered as well. Considering the control input, there is seen that every system uses the photodiode which is quite common for amplitude modulation. As you need input concerning the height of the sample, this should not be replaced with any other input parameter. It can however be fulfilled with a second control input. This would make the most sense if there is another control loop, like for the feed-forward compensation approach.

Observing the results in table 4.1, it is quite remarkable that all the control techniques are based on either the cantilever or Z-stage, while there is also a possibility to control the X and Y stage. A possibility could be the level of simplicity for improving the Z-stage or cantilever, as it only adjusts the control loop that already exists. Controlling the X and/or Y stages would imply a second control loop which makes the system more complex. There has been done quite some research on different scanning methods, for example, spiral scanning [62, 63] and a Local Circular Scanning algorithm [64]. However, these do not focus on tackling parachuting at all. Their main focuses are increasing the scan speed and introducing a novel idea. There could be an opportunity to explore the possibilities for an improved raster scan for the original scan path. Moreover, there could be investigated control techniques that incorporate the geometry of the probe of the cantilever into improving the lateral resolution which affects the spatial resolution as shown in equation 3.5. An example where the geometry of the probe is taken into account is shown by Heath et. al who uses the principle of Localization Atomic Force Microscopy [65].

In general, raster scanning methods contain forward and backward traces as shown in figure 4.1. One raster line is scanned twice but only the forward or backward scan mode is used, deleting 50% of the information. This phenomenon holds not only for the conventional methods but also for the different experimental methods which are discussed above. It is a waste that the area

has been scanned twice while nothing is done with it. It can be an idea to alternate the scan path, run every scan path once and merge it into one image. Theoretically, this could decrease the time required for an image by 50%. However, this will most probably not work due to the hysteresis effect that occurs in the piezo actuators. There is a strong nonlinearity within the piezo actuators which is the main reason you want to perform either a forward or backward scan, but not both at a time. It could be an idea to investigate the possibility of ultra-fast scanning the forward path, roughly measure if there is any topography present, and use the backward scan for its topography based on whether there is a sample present.

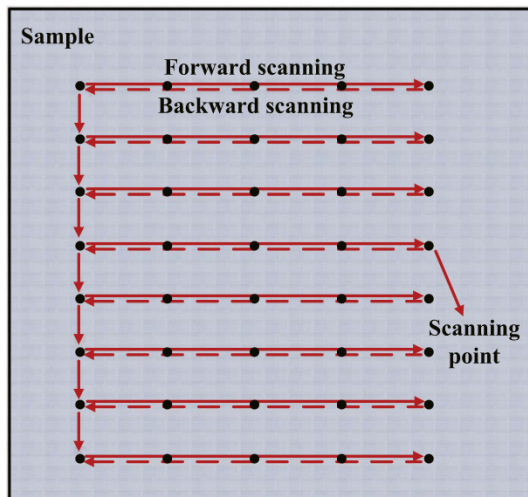


Figure 4.1: The path that is followed by a typical raster scan [34]

Let's assume a standard calibration sample with holes having a diameter of 500nm and 500nm space between every hole for the horizontal and vertical axis, X and Y axis respectively. In here, the X-axis measures the topography and will be controlled; the Y-axis is used to go to the next scan line. Taking a sample of $5\mu m \times 5\mu m$, a maximum amount of 25 holes can be present. If we scan the sample via a conventional method with a scan speed of $V_s = 100\mu m/s$ and a cantilever with a resonance frequency of $f_c = 150kHz$, it will take 26.7 seconds to scan the full sample.

To determine the maximum scan speed of the forward scan path, assumptions need to be made concerning the lateral resolution. The wavelength λ of the scanning probe can be determined via $\lambda = V_s/f_c = 0.67nm$. This states that any hole with a diameter smaller than 0.67nm could be skipped which thus gives a boundary for the lateral resolution. Depending on the level of lateral resolution that is required, a new wavelength can be specified which can be calculated into the maximum possible scan speed. If we assume that a lateral resolution of 5nm is acceptable, a scan speed of $750\mu m/s$ is reached for the forward scan path. From the sample, it is known that 50% of the scan lines do not contain any object and thus can keep this scanning speed for its backward scan topography. For the remaining 50%, it means that some topography is measured on which a slow scan is required as a backward scan. Now assume that this slow scan rate is done at $5\mu m/s$ which is slow enough to cope with parachuting. A rough calculation can be done for an average scan speed, which can be compared with the conventional scan speed.

50% of the scan lines are done by the forward scan, having a fast speed of $750\mu m/s$. The remaining 50% is done by the backward scan, which consists of a part fast and slow, de-

pending on the amount of topography measured. In this case, 50% of the scan lines do not even contain topography, which thus can keep the fast rate. The remaining 50% of the scan lines consist of about 50% topography, which means that for these scan lines the piezo must accelerate and decelerate at every hole or hill. Out of simplicity, we assume that the time delay as a result of acceleration/deceleration will add 10% extra 'slow scan speed' per scan line. In the end, it would mean that the backward scan consists of a 70% fast scan and 30% slow scan rate. The following calculation can be done: $V_{av} = \frac{1}{2}(V_{forward}) + \frac{1}{2}(V_{backward}) = \frac{1}{2}(100\% * 750\mu m/s) + \frac{1}{2}(70\% * 750\mu m/s + 30\% * 5\mu m/s) = 638\mu m/s$. This is already 6.4 times faster than the conventional method. The new scan would be done in 4.2 seconds with an improved spatial resolution as no parachuting will occur.

Of course, this scanning speed will most likely not hold as there are many oversimplifications present, like an additional drift factor for the X-axis, Y-axis movement, and time delay in the control loop. The additional drift factor for the X-axis can give some serious concerns as it will act when the scan speed accelerates and decelerates. It could be wise to perform this control technique with some intermediate steps, like starting with a slow constant backward rate instead of adaptive. However, after incorporating the new technique with its possible disadvantages, it still can have a huge potential in reaching much higher scan speeds with a better spatial resolution for HS-AFM. Finally, there can be thought of combinations between this approach and existing methods such as Dynamic PID and/or Q-control to further optimize the control of HS-AFM. This is because of their differences so that they will not interfere with each other.

Chapter 5

Project proposal

As a result of the discussion from the previous section, a research proposal can be formed. The research proposal will consist of a research question that is in line with the main goal of this literature paper. A proof-of-concept will be made in Matlab to show the feasibility of this novel idea. After that, a methodology is written on how to practically implement it on an AFM.

5.1 Research Question

The following research question is formulated with its intermediate steps:

How can a variable scan speed decrease the effect of parachuting and thereby improve the spatial resolution for high-speed atomic force microscopy?

At first, a model will be built in Matlab from the theory that models an AFM. This model will contain a constant speed and represents the conventional scanning method. After that, this model will be modified towards the adaptive approach. For the forward scan line, this modified model should solely look at whether there is a height difference measured in the scan line or not. Based on this information, the control loop decides to perform either a slow or fast scan rate for the backward scan.

Then, differences within a forward scan line can be observed and distinguished. This can be implemented such that there can be made a difference between certain height differences which can be implemented into a variable scan speed for the backward scan.

Next, the adaptive scanning method can be compared to the conventional scanning method to validate the feasibility of this proof-of-concept. Additionally, it could be possible to define certain variations within the model to find any consideration between robustness and efficiency which might improve the performance of this adaptive scanning method.

After that, there will be investigated how to practically implement this proof-of-concept in a real-life implementation. The Nanosurf JPK ([66]) at the PME lab at the TU Delft will be considered as potential experimental setup. For this AFM, there will be investigated for a combination of software and hardware that could work as an experimental setup to test this novel idea.

Chapter 6

Modelling the AFM

This chapter explains the dynamics of the AFM. At first, the dynamics of the cantilever are explained. It shows a state-space model, followed by the input signal and tip-sample force which are the input parameters of this model. Next, the z-scanner, Lock-In Amplifier, and controller are explained which are the other elements of the complete control loop. After that, the imaging technique and scanning direction are explained. Lastly, there is explained how there is accounted for the step response at the start of a signal, followed by the two different ground truths that are used to analyze its performance. A validation technique is introduced which is used to compare the Adaptive Scanning Method with the conventional method.

6.1 Cantilever's dynamics

The cantilever of the AFM is modeled as a mass-spring-damper system, obeying the following equation of motion [67]:

$$m_c \ddot{z}(t) + c_c \dot{z}(t) + k_c z(t) = F_c \quad (6.1)$$

where z corresponds with the position of the cantilever's tip and its derivatives. F_c is the force that is applied to the cantilever. m_c is the mass of the cantilever and is described by $m_c = \frac{k_c}{\omega_c^2}$. k_c is the stiffness of the cantilever and $\omega_c = 2\pi f_c$ where f_c is the cantilever resonance frequency. c_c is the damping coefficient and is described as $c_c = \frac{k_c}{Q_c \omega_c}$ with Q_c as the quality factor of the cantilever. The cantilever's properties are achieved from measurement data, valued as $k_c = 0.47$ N/m, $Q_c = 1.59$, and $f_c = 400$ kHz.

The force F_c applied on the cantilever is split into two forces: an excitation force F_{ext} , and a tip-sample force F_{ts} . The excitation force is further described as a cosine, namely $F_{ext} = F_0 \cos \omega_0 t$ where F_0 and ω_0 are the amplitude and angular frequency of the excitation force, respectively. Filling this into equation (6.1), it leads to the following differential equation [68]:

$$m_c \ddot{z}(t) + \frac{m_c \omega_c}{Q_c} \dot{z}(t) + k_c z(t) = F_{ts} + F_0 \cos \omega_0 t \quad (6.2)$$

The equation of motion of the cantilever will later be used in section 10.5.2 to model the cantilever for its real-life implementation.

For the proof-of-concept, cantilever dynamics is approximated by the linear-time-invariant (LTI) system as a state-space model

$$\begin{aligned} x(k+1) &= Ax(k) + B\bar{u}(k) \\ y(k) &= Cx(k) + D\bar{u}(k) \end{aligned} \quad (6.3)$$

where A is the system matrix, B is the input matrix, C is the output matrix, and D is the feed-forward matrix. D is 0 since there is only feedback present. $x(k)$ is the state and $y(k)$ the measured cantilever deflection at time step k . $\bar{u}(k) = u_c(k) + F_{ts}(k) + \eta(k)$ consists of the input signal, or driving force $u_c(k)$, the tip-sample force $F_{ts}(k)$ and process noise $\eta(k)$ with variance R_η .

The system matrices A , B , and C , and the process noise $\eta(k)$ are achieved from measurement data that considers system identification on the Nanosurf JPK at the TU Delft. The signals that are mentioned above are sampled with rate $1/t_s = 10$ MHz.

6.2 Input signal u_c

The input signal u_c is determined using the variable z . z is the position of the cantilever, of which its steady-state oscillation is approximated by a sinusoidal oscillation [69],

$$z(z_c, t) = z_0(z_c) + A(z_c) \cos(\omega_c t - \phi(z_c)) \quad (6.4)$$

$\omega_c = 2\pi f_c$ is the driving frequency of the cantilever. z_0 is the mean deflection which is zero, A the driving amplitude and ϕ the phase shift of the oscillation. A and ϕ are achieved from measurement data and are valued as 12 nm and $\pi/6$, respectively. z_c is the equilibrium tip-sample separation in absence of interactions and t is the time which is described towards the discrete domain via t_s . Figure 6.1 shows the difference between z and z_c .

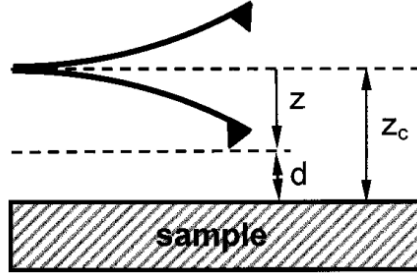


Figure 6.1: Supporting illustration considering the steady-state oscillation, taken from [68]. The origin of the z coordinate is the average cantilever position. z_c is the rest separation as a result of a tip-sample separation called d within this image.

6.3 tip-sample force F_{ts}

The tip-sample force F_{ts} is a non-linear force as a result of Van der Waals forces and the Pauli Principle as described in section 3.5. Out of simplicity, the tip-sample force is modeled in a linear manner as shown in Eq. 6.5.

$$F_{ts}(k) = \begin{cases} C(h(k) - y(k)) & \text{for } y(k) < h(k) \\ 0 & \text{otherwise} \end{cases} \quad (6.5)$$

where $h(k)$ is the sample height, $y(k)$ is the deflection of the cantilever at time step k . C is a constant that corresponds to the hardness of the sample.

6.4 Z-scanner

The z-scanner is a second-order low-pass filter, which is described by Kodera et. al [70]. This leads to transfer function G_z ,

$$G_z(s) = \frac{\omega_z^2}{s^2 + (\omega_z/Q_z)s + \omega_z^2} \quad (6.6)$$

where $\omega_z = 2\pi f_z$ with f_z the resonance frequency of the z-scanner; Q_z is the quality factor of the z-scanner. These are valued from measurement data at $f_z=100\text{kHz}$ and $Q_z=2$.

An in-built function of Matlab 'ss' converts continuous transfer function G_z towards the discrete state-space representation with the sample time t_s .

6.5 Lock-In Amplifier

A Lock-In Amplifier (LIA) filters the signal such that its minima can be determined accurately in a later stage. For this, it uses the methodology described by DeVore [71].

At first, the input signal is preamplified by a factor g as given in Eq. 6.7.

$$\begin{aligned} V_I &= gy_c \\ \text{with } y_c &= y + \nu \end{aligned} \quad (6.7)$$

where y is the output from the cantilever's dynamics as seen in equation 8.1 $\nu(k)$ is the measurement noise with variance R_ν which is achieved from measurement data.

A reference signal is generated based on the cantilever drive frequency f_c . This signal is split in a cosine v_{RX} and sine v_{RY} part as seen in Eq. 6.8. There is a 90 degrees phase shift between these two signals.

$$\begin{aligned} v_{RX} &= \cos(2\pi f_c t) \\ v_{RY} &= -\sin(2\pi f_c t) \end{aligned} \quad (6.8)$$

After that, the amplified output of the cantilever V_I is mixed with reference signals v_{RX} and v_{RY} .

$$\begin{aligned} V_{MX}(t) &= V_I(t)v_{RX}(t) \\ V_{MY}(t) &= V_I(t)v_{RY}(t) \end{aligned} \quad (6.9)$$

Next, mixed signals V_{MX} and V_{MY} are put into a low-pass filter. A review of demodulation techniques for AM-AFM by Ruppert [72] shows that a fourth-order Butterworth filter is most convenient as a low-pass filter for the lock-in amplifier. The filter uses a cut-off frequency f_{LIA} of 40% of the cantilever drive frequency, thus $f_{LIA} = 0.4 \times 400\text{kHz} = 160\text{kHz}$ [73].

The LIA filters the signal such that there is one LIA measurement per oscillation period. Since there is a drive frequency of 400kHz, the filter reduces the data set with a factor,

$$\begin{aligned} \text{factor} &= \frac{1}{t_s} / f_c \\ &= 10 \text{ MHz} / 400\text{kHz} \\ &= 25 \end{aligned} \quad (6.10)$$

Filtering V_{MX} and V_{MY} result in V_{OutX} and V_{OutY} , respectively. The total magnitude A_{LIA} and phase difference ϕ_{LIA} are the results of the following calculations,

$$\begin{aligned} A_{LIA} &= (2/g) \sqrt{V_{OutX}^2 + V_{OutY}^2} \\ \phi_{LIA} &= \tan^{-1}(V_{OutY}/V_{OutX}) \end{aligned} \quad (6.11)$$

Recall that g is the factor that is used in equation (6.7). The magnitude A_{LIA} is the input to the controller which is discussed in the next section.

6.6 Controller

The Nanowizard uses a Proportional-Integral controller K_{PI} as feedback control [74]. The PI controller has the following form,

$$K_{PI}(s) = \frac{K_p s + K_i}{s} \quad (6.12)$$

where K_p is the proportional gain, and K_i the integral gain. The data is achieved from measurements where the gains are empirically designed to $K_p = 0.1$ and $K_i = 7.5 \times 10^4$.

In Matlab, it is modeled as a PID controller of which its derivative gain K_d is set to zero. After that, it is converted into a discrete state-space representation. For the input of the controller, the output from the LIA is used and subtracted with a reference amplitude that is necessary for the feedback control as seen in Eq. 6.13.

$$\begin{aligned} x_c(k+1) &= A_c x_c(k) + B_c (A_{LIA}(k) - A_{ref}) \\ u_z(l) &= C_c x_c(k) + D_c (A_{LIA}(k) - A_{ref}) \end{aligned} \quad (6.13)$$

The matrices A_c , B_c , C_c , and D_c are the system matrices of the controller. x_c is the state or u_z is the output of the controller which is the input to the z-piezo. A_{ref} is a reference amplitude for the feedback control.

6.7 Imaging

The minima of the estimated cantilever deflection are used for imaging. At first, a height reconstruction is made with a condition that estimates it for each oscillation period, which has been retrieved from a yet-to-be-published paper by J. Noom,

$$\left(i - \frac{1}{2}\right) T \leq kt_s < \left(i + \frac{1}{2}\right) T \quad (6.14)$$

with T corresponding to the length of one cantilever oscillation period, thus $T = 1/400\text{kHz}$. t_s is the sampling time and i and k are time steps. Note that i is defined as the number of oscillation periods, whereafter it is multiplied by the period to match with the number of time steps of k .

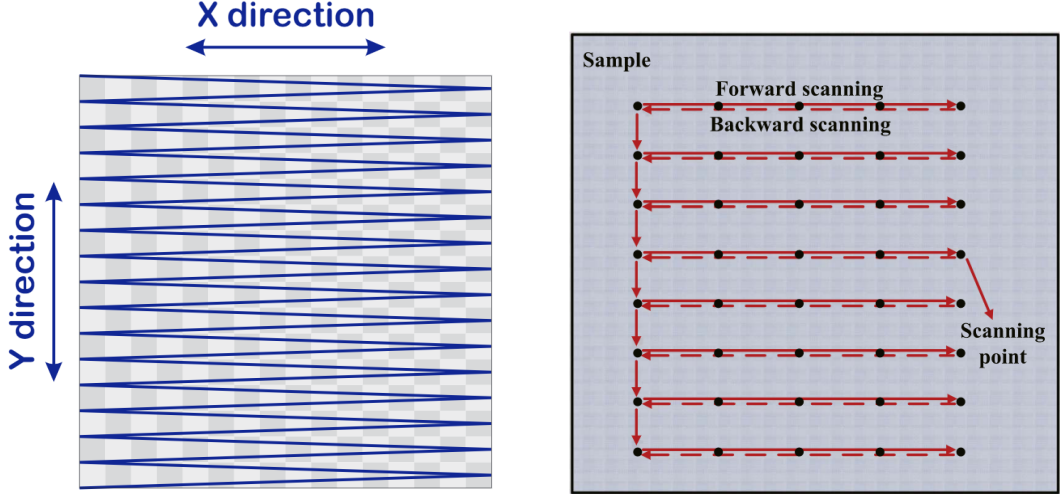
From this condition, i is taken and put into the equation for the minimum of the estimated cantilever deflection \hat{h} ,

$$\hat{h}(i) = \min_k (\hat{y}_c(k)) - \hat{u}_z(i) \quad (6.15)$$

where y_c is taken from equation (6.7) and u_z from equation (6.13).

6.8 Scanning direction

Usually, in practical setups for HS-AFM, there is a slow and fast scan axis present. The X-axis uses a triangular pattern, and Y-axis has a constant velocity. This leads to a zig-zag pattern which is seen in figure 6.2a. This is difficult to model because the system is discretized and built up in individual lines. This means that interpolation methods become necessary between the different scanning points to achieve a zig-zag pattern. Therefore, it is more common to model it as a raster scan as seen in figure 6.2b [34, 75].



(a) The zig-zag scan in experimental setups. The probe has a high velocity along the X-axis and follows a triangular signal. The Y-axis has a constant slow velocity [22]

(b) How the raster scan is performed in the model. The triangular pattern still exists for the fast scan axis, while the slow scan axis has been discretized into steps for modeling purposes. [34]

Figure 6.2: Different scanning directions: The zig-zag scan in experimental setups (6.2a) and the raster scan for theoretical modeling (6.2b)

In Matlab, a sawtooth function is set up for the x-position that follows a function $y = x$ for every individual trace. For the y-position, a for-loop is built for the number of scan lines after which the different data sets are stored in matrices with the dimension 'amount of lines by the length of a scan trace'.

The number of data points for a scan trace is the number of time steps n and is described as,

$$n[-] = \frac{L_s[nm]}{V_H[nm/s]t_s[s]} \quad (6.16)$$

where L_s is the length of the scan trace, V_H the scan speed and t_s the sample time. Different from experimental setups, the simulation first calculates all forward and/or backward traces for both conventional and adaptive scans as that makes the code for the simulation much more efficient and clear while it does not make a difference for its final results. An example of the sawtooth function for 5 lines is shown in figure 6.3. These are combined for the image via the function `repmat()` in Matlab.

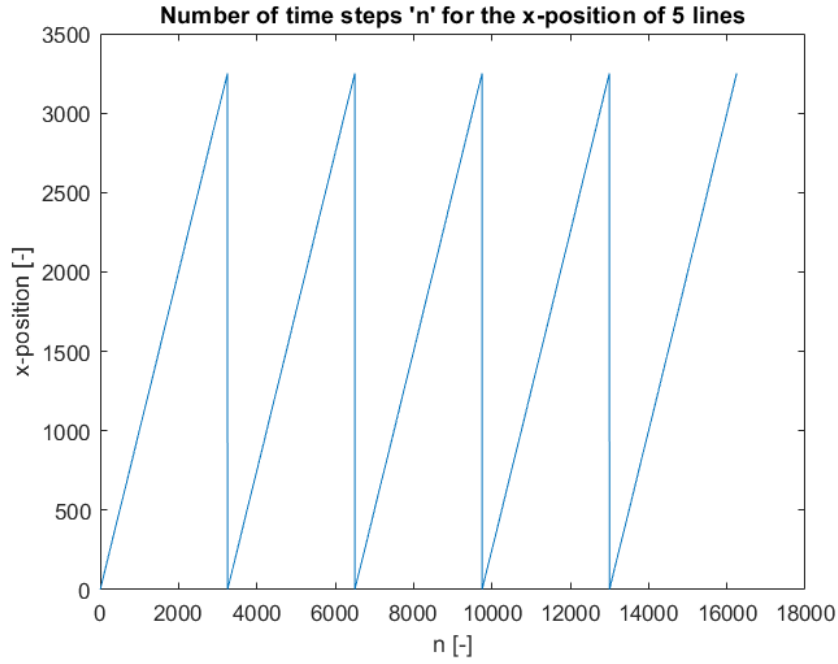


Figure 6.3: For this graph, the following parameters is chosen: $L_s = 25 \text{ nm}$, $V_H = 100 \mu \text{ m/s}$, $t_s = 10 \times 10^{-8} \text{ s}$. This sawtooth function shows the x-position for 5 lines. Each line has a length of 3250 datapoints, which corresponds with Eq. 6.16 as $n = 1.3 \frac{25[\text{nm}]}{10 \times 10^4 [\text{nm/s}] \times 10 \times 10^{-8} [\text{s}]} = 1.3 \times 2500 = 3250$. The multiplication factor of 1.3 is discussed in section 6.9, making the sample 30% longer to remove its step response at the start of the simulation.

6.9 Accounting for the Step Response

The simulation starts oscillating from a stationary position, caused by the settings within the Matlab code. This leads to a step response which is unwanted since it might show some height difference that is not present and thus misleading [76]. Calculating the step response of the signal, there is accounted for misleading information within the code that causes a wrong height approximation. This step response is calculated such that there is accounted for its settling time when the different simulations run.

The total settling time from the step response is approached by calculating the different settling time components individually. The total settling time is divided into different components as discussed in the literature section 2 and mentioned above. The components that are incorporated are the cantilever's dynamics T_c , LIA filter T_{LIA} , PI-controller T_{PI} , and z-scanner dynamics T_z . These are shown in Eq. 6.17. τ_c and τ_z are taken from section 2. For the settling time of second-order underdamped systems, like the cantilever and z-scanner, a general condition is applied of $T_s = 4\tau$ [77].

$$\begin{aligned}
 T_{total} &= T_c + T_{LIA} + T_{PI} + T_z \\
 \text{with } T_c &= 4\tau_c = 4 \frac{Q_c}{\pi f_c}, \\
 T_z &= 4\tau_z = 4 \frac{Q_z}{\pi f_z}, \\
 T_{LIA} &= \tau_{LIA}, \\
 T_{PI} &= \tau_{PI}
 \end{aligned} \tag{6.17}$$

For the LIA filter and PI controller, only the time constants are given since only these influence the total settling time via a certain time delay that is determined through its time constant.

The values for Q_c and f_c are taken from section 6.1, and Q_z and f_z from section 6.4. Filling in Eq. 6.17 gives the following settling time components:

$$\begin{aligned}
 T_c &= \frac{Q_c}{\pi f_c} = 4 \frac{1.59}{\pi \times 400\text{kHz}} = 5.06 \times 10^{-6} \text{ s} \\
 T_z &= 4 \frac{Q_z}{\pi f_z} = 4 \frac{2}{\pi \times 100\text{kHz}} = 2.55 \times 10^{-5} \text{ s}
 \end{aligned}$$

As mentioned in section 6.5, the LIA follows a fourth-order Butterworth filter. The time delay of this filter is calculated via the formula which is shown in Eq. 6.18 [73].

$$\begin{aligned}
 T_{LIA} &= \tau_{LIA} = \frac{0.416}{f_{cutoff}} \text{ [s]} \\
 \text{with } f_{cutoff} &= 0.4f_c \\
 T_{LIA} &= 2.6 \times 10^{-6} \text{ [s]}
 \end{aligned} \tag{6.18}$$

For the time delay of the PI controller, an impulse response is done using Matlab. Using the figure for the impulse response, the time delay is read on. There is found that $T_{PI} = \tau_{PI} = 1 \times 10^{-7}$ seconds. The figure is found in Appendix D.

$$\begin{aligned}
 T_{total} &= T_c + T_{LIA} + T_{PI} + T_z \\
 T_{total} &= 5.06 \times 10^{-6} + 2.55 \times 10^{-5} + 2.6 \times 10^{-6} + 1 \times 10^{-7} = 3.32 \times 10^{-5} \text{ s}
 \end{aligned} \tag{6.19}$$

Thus, the total estimated settle time results in 3.32×10^{-5} seconds. For the simulation, there must be incorporated for the total settle time such that there is no unwanted misleading height profile presence at the start of a scan line. In order to calculate the number of time steps that are necessary to incorporate for the settling time, the sample time is divided which leads to the following expression in Eq.6.20.

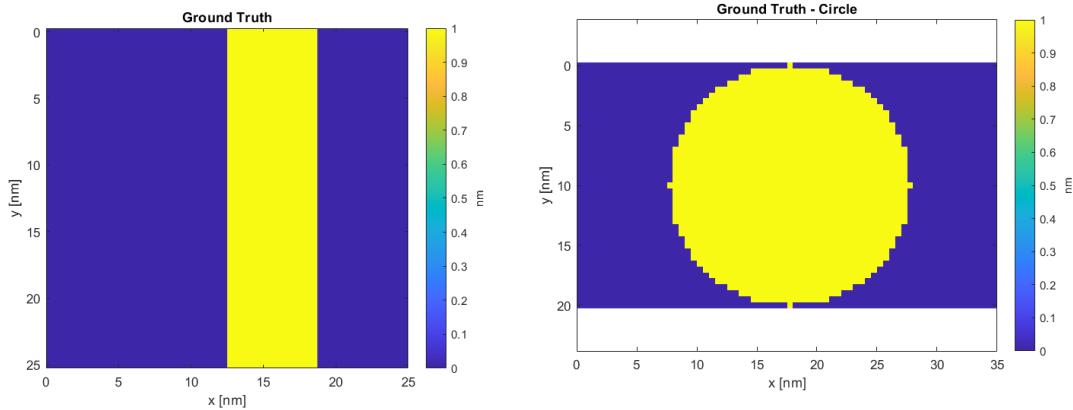
$$n = \frac{T_s}{t_s} = \frac{3.32 \times 10^{-5}}{1 \times 10^{-7}} \quad (6.20)$$

$$n = 332 \text{ Time steps}$$

This means that at least 332 time steps should be added to the sample to let the signal settle before a measurement is done. The signal is extended with 30% of its original path length to make sure that the signal has been settled. For example, taking a scan speed of $100 \mu\text{m}/\text{s}$ would lead to an addition of $n = 30\% \times \frac{25\text{nm}}{100\mu\text{m}/\text{s} \times 1 \times 10^{-7}\text{s}} = 750$ Time steps which are large enough for the signal to settle since 750 is larger than the required 332 time steps. The additional time steps are removed afterward such that the unwanted step response pattern disappears.

6.10 Sample - Ground Truth

A ground truth is made for the simulation to be able to analyze its performance with the truth. It is set up as a sample with a height of 1 nm and width of 6.25nm as shown in figure 6.4a. The scanned area is 25x25nm. The GT is made non-symmetrical to distinguish forward and backward lines for the code and report. As the primary goal is to show the proof-of-concept for this method, the sample has been kept rather simple. There are 50 equal lines used per simulation, to make it easy to show and compare its performance for the current parameters. After that, a more challenging shape is used as ground truth which is shown in figure 6.4b. This is a circle which consists of 41 lines and has a scanned area of 20x35nm. This gives a measure of its performance for different widths of lines.



(a) The ground truth of the sample to show the proof-of-concept (b) A more varying shape to show its performance for other sample widths.

Figure 6.4: The two different Ground Truths (GT) that are used.

6.11 Validating the model

The validation of the model is done by using the least-squares fit approach done by Verhaegen et. al [78],

$$\min_c \left\| h(k) - \hat{h}(k) - \begin{bmatrix} 1 \\ \vdots \\ 1 \end{bmatrix} c \right\|_2^2 \quad (6.21)$$

where c is a constant that implies a systematic shift of the general baseline for the overall error. $h(k)$ is the ground truth, $\hat{h}(k)$ the estimated cantilever deflection and k the time steps. The array filled with ones has a length of k as well.

At first, c is determined,

$$c \approx \begin{bmatrix} 1 \\ \vdots \\ 1 \end{bmatrix} / (h(k) - \hat{h}(k)) \quad (6.22)$$

Then, the error ϵ is calculated which unit is in nm^2 ,

$$\epsilon = \sum_{k=1}^n (h(k) - \hat{h}(k) - c)^2 \quad (6.23)$$

The sum takes n number of time steps since there is a maximum of n time steps on a line scan as explained in equation (6.16).

Chapter 7

Implementing the Adaptive Scan

This chapter explains the implementation of the Adaptive Scanning Method. For the adaptive scan, the process is divided into the following steps:

1. Conventional forward scan at very high speed
2. Designing the Detection Algorithm
3. Implementing the variable speed
4. Performing the adaptive backward scan

7.1 Conventional forward scan at very high speed

At first, a conventional forward scan at a very high speed is done. The scan speed that is used should be higher than the conventional approach for the backward scan. Otherwise, it would be impossible to save time for the method of adaptive scanning with respect to its conventional method. For this section, a forward scan speed of $170 \mu\text{m}/\text{s}$ is used to show this method.

7.2 Designing the Detection Algorithm

Next, the forward scan is analyzed to determine at which time steps an uphill or parachuting pattern occurs. In order to reach that, there must be found consistency within the signals from which certain patterns are taken. The answer lies in the derivatives of the output signal. As is seen in figure 7.1, the magnitude of the first derivative increases for an uphill pattern, and it decreases for a parachuting pattern. Furthermore, there is observed that the rate of increase/decrease differs. At the time steps where the AFM scans the corners of the sample, an instantaneous increase/decrease is present for the output of its first derivative. This is translated into the second derivative.

In figure 7.2, the first and second derivatives of the output signal are visualized. From the second derivative, clear peaks become already visible that show uphill and parachuting patterns, around time steps 30 and 45. There could be said that there is already enough evidence present to say that these time steps are correct to choose, which could be taken from this signal by taking the maximum and minimum. However, there might be some cases where this behavior is not that obvious to observe, caused by the combination of added noise and the LIA filter.

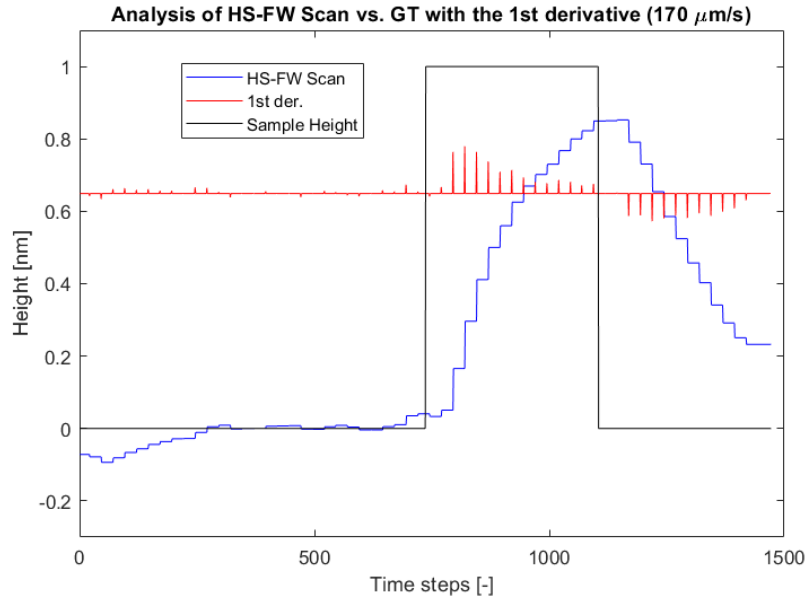


Figure 7.1: An high-speed forward scan is done at $170\mu\text{m/s}$ and plotted against the Ground Truth and its first derivative. The horizontal lines within the HS-FW Scan are caused by the imaging technique that is used, which is explained in section 6.7. Here, the minimum of every oscillation is taken, which has a length of 25 time steps as shown in equation (6.10). This causes the height of a signal to be constant for 25 time steps until a new minimum of an oscillation has become clear.

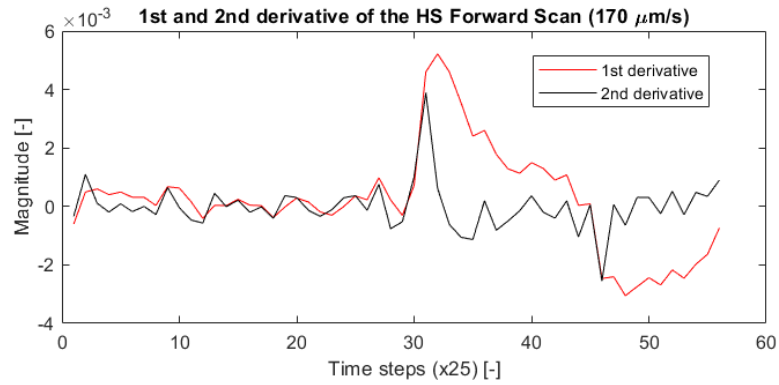


Figure 7.2: The first and second derivative of a single line scan at $170\mu\text{m/s}$ is shown. From the first derivative, the positive regime of the uphill region is clearly seen (time steps $\approx 30 - 45$), followed by the negative regime of the parachuting region (time steps $\approx 45 - 55$). The second derivative indicates at which exact time step an uphill or parachuting action happens, at 31 and 46.

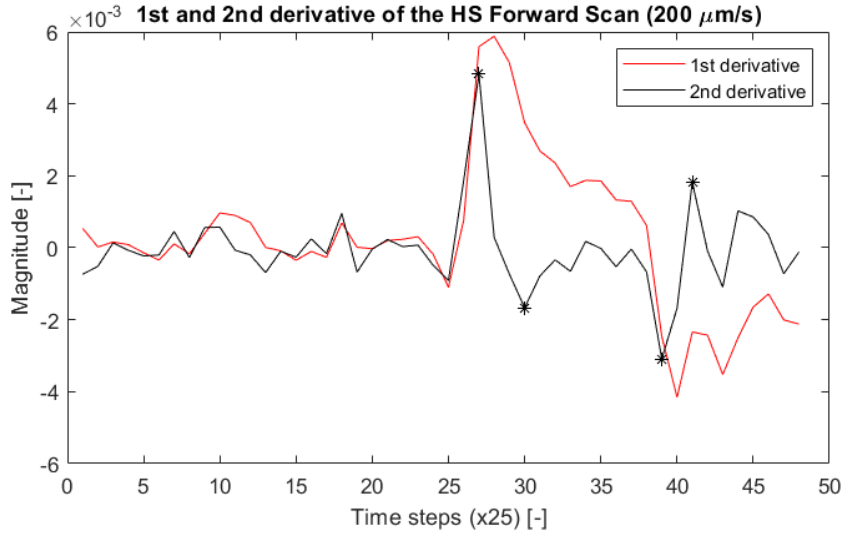


Figure 7.3: The first and second derivative of a single line scan at $200\mu\text{m/s}$ is shown. The first derivative still shows clear regimes for uphill or parachuting regions. The second derivative creates more maxima and minima which makes it more difficult to analyze.

For example, figure 7.3 shows the indistinctness of the peaks and valleys within the second derivative. For the second derivative, there are two regions that show positiveness: at the start of an uphill region, and after a parachuting region. This makes sense as both increasing acceleration and decreasing deceleration show a positive outcome for the second derivative. The same principle holds for the two regions that show negativeness: after an uphill region and at the start of a parachuting region. These four cases are set up in the table below,

	Region 1 (Uphill)	Region 2 (Uphill)	Region 3 (Parachuting)	Region 4 (Parachuting)
1st der.	+	+	-	-
2nd der.	+	-	-	+

Within these four regions, the first and third should be picked out as these show the starting point and end point of the sample. These two regions are separated from the other two regions by setting up a mixed signal that multiplies the first and second derivatives. Combining a high acceleration and its current change over time leads to clear maxima that are linked towards an uphill or parachuting region as shown in figure 7.4.

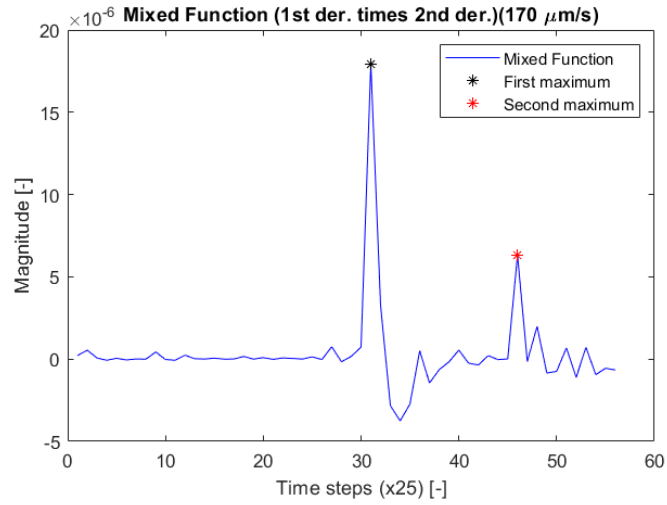


Figure 7.4: The mixed function is a multiplication of the first and second derivative of the signal. The positive extremes are regions where the direction of the second derivative is in line with the first derivative. For negative extremes, these directions are their opposites.

These maxima are chosen as time points for the adaptive backward line. Still, there must be checked which maxima show an uphill region and which parachuting. A condition is taken for these maxima where there is observed at the first derivative graph and see in what region it is present. This is done in figure 7.5. There is seen that the first maximum remains in the uphill region and the second maximum in the parachuting region.

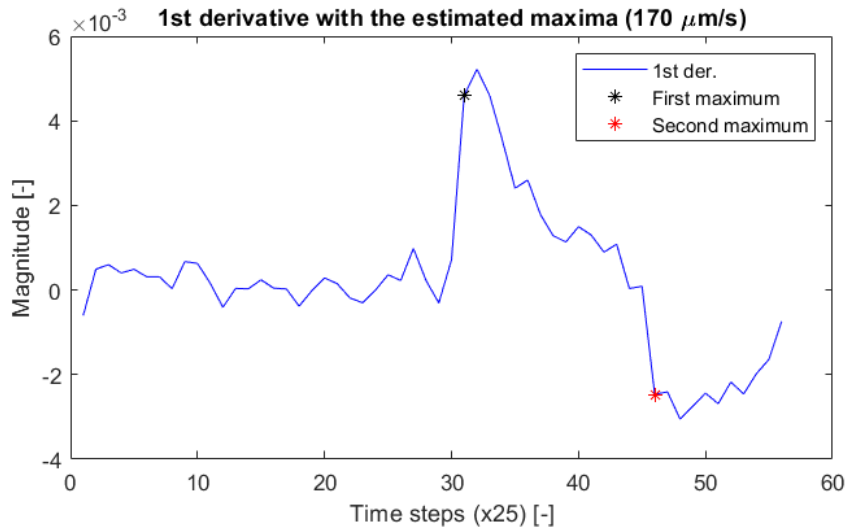


Figure 7.5: Boundary condition for the maxima that are found in figure 7.4. An increase for the first derivative implies an uphill region, and a decrease in a parachuting region.

Finally, these estimated time steps are used as sample predictions. In figure 7.6, the sample prediction is plotted against the Ground Truth and High-Speed Forward Scan. There is seen that there is a certain horizontal shift of the sample present, which is explained by the time delay of the LIA and Z-scanner.

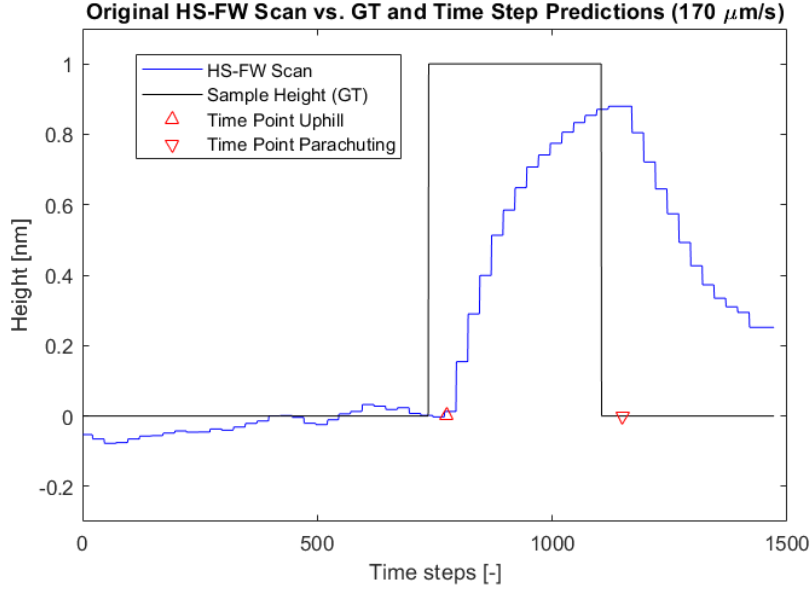


Figure 7.6: The High-Speed Forward Scan against the Ground Truth and Time Step Predictions. This shows the accuracy of the identification of any uphill or parachuting behavior on the sample. Furthermore, a time delay is observed between the Ground Truth and the different time points.

As mentioned in the literature review in section 3.7 and visible in figure 7.6, there is a certain time delay present between the ground truth and the measured signals. For this Adaptive Raster Scanning method, the signal is measured after the controller. This means that it shows a time delay depending on the cantilever's response time, LIA filter, and PI controller because the signal is analyzed after the controller. For the current model, only the time delay of the LIA, because from the literature is found that this has a large influence on the total time delay. The remaining components are discussed later in section 9.2.2.

The time delay of the LIA consists of 2.6×10^{-6} seconds as shown in Eq.6.18 from section 6.9. Dividing it by the sample time, this results in $\frac{2.6 \times 10^{-6}}{10 \times 10^{-8}} = 26$ Time steps. Thus, 26 Time steps are used as a time delay component to be incorporated into the simulation model.

7.2.1 Implementing the variable speed

After the identification of the High-Speed Forward signal, the time steps are set up for the forward line and need to be switched toward the backward line. This is done by taking the full length of a line and subtracting the time points at which the uphill and parachuting event occurs. Important to note is that the *Time Point Uphill* from figure 7.6 becomes the new parachuting time point, and the *Time Point Parachuting* becomes the new uphill time point as the scanning direction is switched. This leads to the following time points as shown in Eq. 7.1.

$$\begin{aligned} \text{New Time Point Uphill} &= \text{Total length sample} - (\text{Time Point Parachuting} - \text{Time Delay LIA}) \\ \text{New Time Point Parachuting} &= \text{Total length sample} - (\text{Time Point Uphill} - \text{Time Delay LIA}) \end{aligned} \quad (7.1)$$

Figure 7.7 shows the new time points within the backward scan as discussed above. As a result of switching from forward to backward scanning, the time points flip to the other side of the black line as well. Where in figure 7.6, there is seen that the detections of time points for the forward scan were always *after* the events occurred. For backward scanning, it is highly recommended to set up time points *before* the events occur. The speed must be already adjusted to a lower value before it scans any uphill or parachuting event, or it scans these at high speed again resulting in bad imaging.

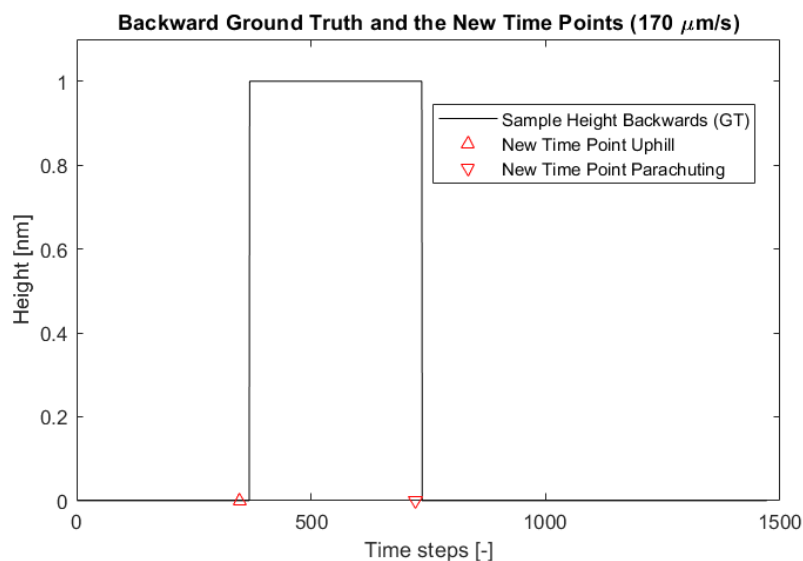


Figure 7.7: The Backward Ground Truth and the estimated time points for this line. The GT is flipped since the AFM scans from the right to the left. Furthermore, flipping the signal causes the new time points to lie before the uphill and parachuting events.

For the time points where the uphill and parachuting events occur, the speed is adjusted to a lower value for better scanning quality. However, a lower scan speed is only necessary for the distance where the signal settles towards the sample height (uphill) or zero baseline (parachuting). For this, a variable d_{adap} is introduced which fixes a distance on the sample where there is scanned at a slower speed. The variables $d_{adap} = 1, 2,$ and 4 nm are chosen as parameters to test the performance of the Adaptive Raster Scanning method. To show the working principle of this method, d_{adap} is set to 2 nm.

This means that these follow the reasoning of Eq. 6.16, where L_s is replaced with d_{adap} . The dimensionless time blocks t_{up} and t_{par} are set up in Eq. 7.2 to show the number of time steps that are taken to scan at a lower rate. For this report, there is chosen to take the same parameter as d_{adap} for t_{up} and t_{par} .

$$\begin{aligned}
 t_{up} = t_{par} &= \frac{d_{adap}}{V_H t_s} \\
 \text{with } d_{adap} &= 2 \text{ nm} \\
 &= 117.65 = 118 \text{ Time steps}
 \end{aligned} \tag{7.2}$$

Furthermore, it scans at an adaptive speed of $V_L = 10 \mu\text{m}/\text{s}$ during this domain, which is slow enough to scan with almost no parachuting at a sample height of 1 nm. The visualization of the domains for a line scan is shown in figure 7.8.

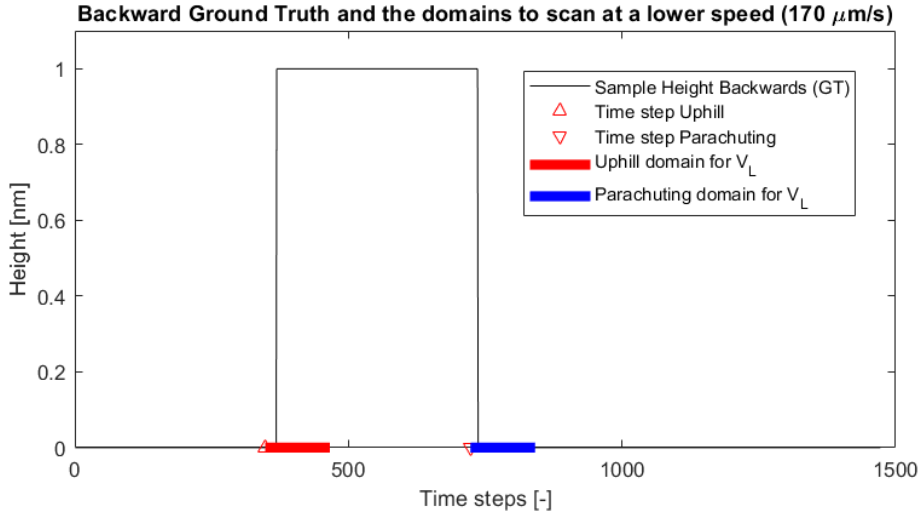


Figure 7.8: The Backward Ground Truth and the red and blue arced time points to scan at a lower speed of $V_L = 10 \mu\text{m}/\text{s}$.

In order to simulate this varying scan speed for the backward scan, the sample is adjusted toward its correct scan speed. This means that the sample is extended as input for the general feedback controller and shortened afterward. Since t_s is constant, the distances with a lower scan speed contain more 'time steps'. Furthermore, it is extended and shortened in a linear manner without any averaging. This method is equivalent to applying a variable scan speed and thus gives the same result. In order to reach the right amount of time steps, it must be extended with a factor $\frac{V_H}{V_L}$ which is based on the forward scan speed. These proportions follow the formula as shown in Eq.7.3:

$$\begin{aligned} \text{Extended Uphill domain} &= \frac{V_H}{V_L} t_{up} = \frac{V_H}{V_L} \times \frac{d_{adap}}{V_H t_s} \\ &= \frac{d_{adap}}{V_L t_s} = \frac{2 \text{ nm}}{10 \mu\text{m/s} \times 10 \times 10^{-8} \text{ s}} = 2000 \text{ Time steps} \end{aligned} \quad (7.3)$$

Since $t_{par} = t_{up}$,

Extended Parachuting domain = Extended Uphill domain = 2000 Time steps

There is observed that the formulation for the extended time steps is independent of the forward scan speed, because the tuning parameter for the length of the slow scanning distance is chosen as d_{adap} .

The calculations for the new time steps are visualized in figure 7.9. This extended sample is used as input for the backward scan, whereafter it is shortened to its normal sample size.

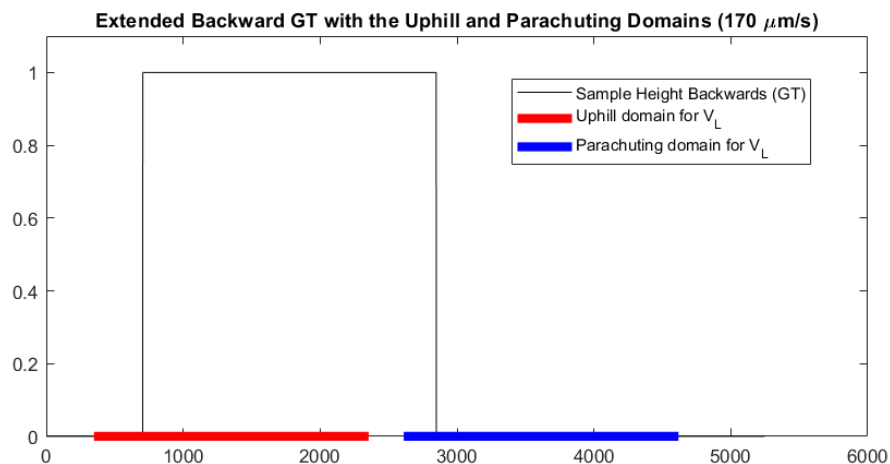


Figure 7.9: The sample has been extended with a factor of $V_H/V_L = 170/10 = 17$ times. Thus, the 118 (117.65) time steps are linearly extended to 2000 time steps.

7.3 Performing the adaptive backward scan

The backward scan is performed on the extended sample, which must be shortened back to its normal sample size such that the output is equivalent to using the variable speed approach. This means that the 2000 time steps must be shortened to 118-time steps. This is done by picking every $\frac{V_H}{V_L}$ th number from the extended array such that it is plotted in a normal format. So, for the scan above with a $V_H = 170\mu\text{m/s}$ and $V_L = 10\mu\text{m/s}$, every 17th number from the extended array is taken, such that it is shortened towards its original length of $2000/17 \approx 118$ time steps.

Chapter 8

Simulation results

In this section, the results are shown for the simulations which are done in Matlab. First, the results from the measurement data are shown. Then, the results for the step response at the beginning of the signal are shown. Next, the results from the Adaptive Raster Scanning Method are shown, whereafter its performance for $d_{adap}=1, 2,$ and 4 nm are set against the conventional method. After that, the results of the performance of the detection algorithm are shown. Lastly, the result of scanning a circular shape is shown.

8.1 System Identification on the AFM

The system matrices A, B, and C are inspected from measurement data on the Nanosurf JPK at the TU Delft. These are filled in for (8.1),

$$\begin{aligned}x(k+1) &= Ax(k) + B\bar{u}(k) = \begin{bmatrix} 0.7908 & 0.3830 \\ -0.2277 & 0.9059 \end{bmatrix} x + \begin{bmatrix} 1.2249 \\ 0.2142 \end{bmatrix} (u_c(k) + F_{ts}(k) + \eta(k)) \\ y(k) &= Cx(k) = \begin{bmatrix} 0.0338 \\ -0.0105 \end{bmatrix} x\end{aligned}\tag{8.1}$$

From the same measurement data, the variances of process noise $\eta(k)$ and measurement noise $\nu(k)$ are valued as $R_\eta=0.0033$ and $R_\nu = 2.41 \times 10^{-5}$.

An unrounded version of the system matrices is shown in Appendix C.

8.2 Accounting for the Step Response

As mentioned in section 6.9, there is a step response pattern expected at the beginning of the simulation as a result of settings within the Matlab code. Figure 8.1 shows the result of a line scan where this step response pattern is present.

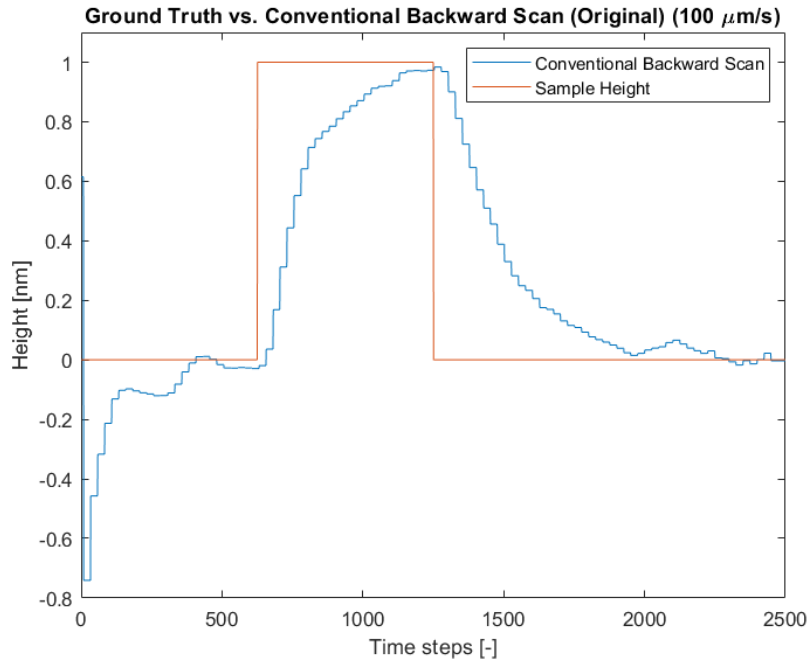
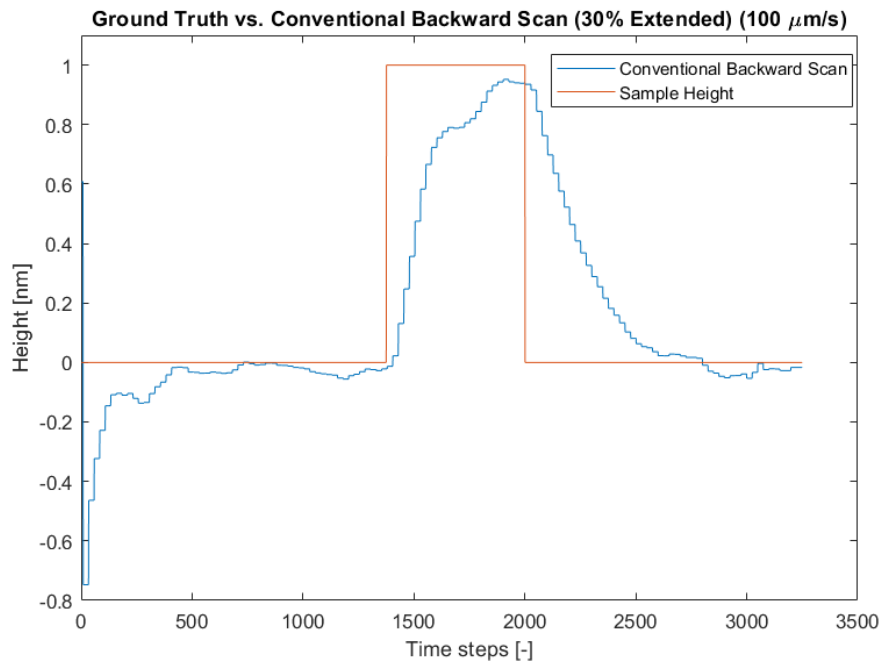


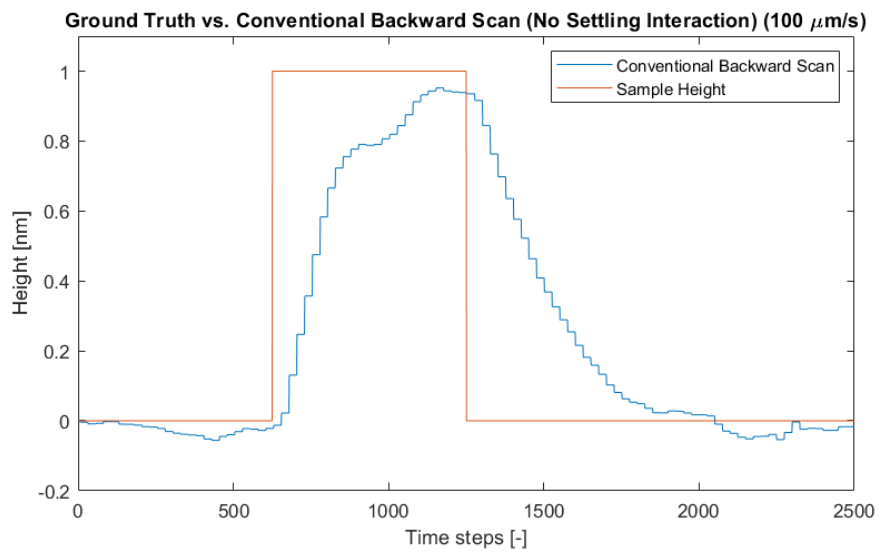
Figure 8.1: The original signal is shown where the step response pattern as a result of oscillating from a stationary position is present.

There is seen that it has a step response pattern at the start of the simulation. This step response has an overshoot toward a negative height with a magnitude of around -0.7 nm. The settling time can be read in the figure as well. The amount of time steps is read where the Conventional Backward Scan crosses the $h = 0$ nm line. This happens at 407 time steps.

Next, the signal is extended with 30% of its original path length to make sure that the signal is settled as mentioned in section 6.9. For a scan speed of $100\mu\text{m/s}$, it corresponded to 750 extra time steps to let the signal settle. The extended line scan is shown in figure 8.2a, and figure 8.2b shows the line scan where the step response pattern is removed.



(a)



(b)

Figure 8.2: 8.2a shows the extended signal where 30% of its total sample length is added. This results in $2500 \times 1.3 = 3250$ time steps, where 750 time steps are added at a scan speed of $100\mu\text{m/s}$. 8.2b shows the sample height estimation after it is turned back to its normal sample length by removing the extra added time steps. This removes the unwanted step response. Note that different noise values are used for the simulation runs between figure 8.1 and figures (8.2a, 8.2b), resulting in slightly different figures.

8.3 Results from the Adaptive Raster Scanning Method

The intermediate results for the Adaptive Raster Scanning Method are shown, whereafter the final results are visualized. Performing the simulations, a forward scan at $160 \mu\text{m/s}$ with $d_{\text{adapt}} = 2\text{nm}$ is shown in the upper figure 8.3. This output is used as input for the adaptive backward scan via the detection algorithm as described in section 7.2. An intermediate result is the adaptive backward scan before it is resampled, as shown in the bottom figure 8.3. It shows the extended regions as explained in section 7.2.1.

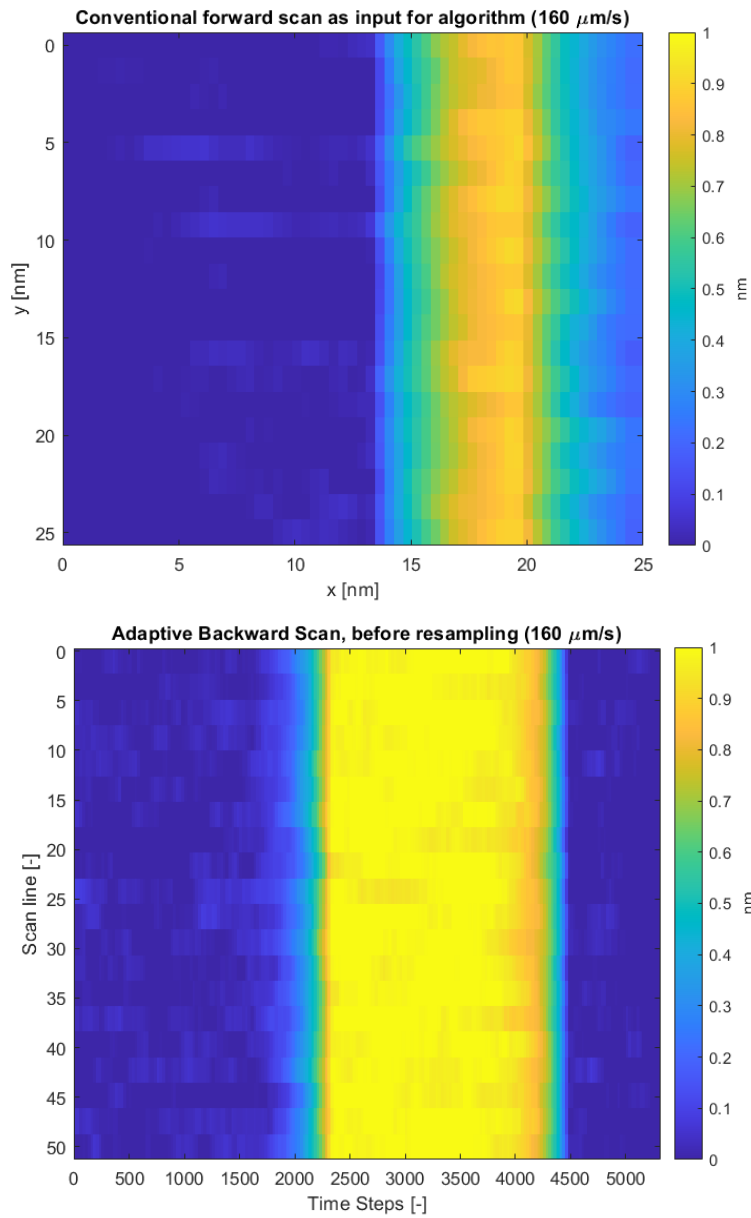


Figure 8.3

Figures 8.4 show the Ground Truth versus the Conventional Raster Scan at 10 and 70 $\mu\text{m/s}$, and the Adaptive Raster Scan at 160 $\mu\text{m/s}$ is shown. The conventional Raster Scan at 10 $\mu\text{m/s}$ shows a similar error value to the Adaptive Raster Scan, and the Conventional Raster Scan at 70 $\mu\text{m/s}$ shows an equal scanning time.

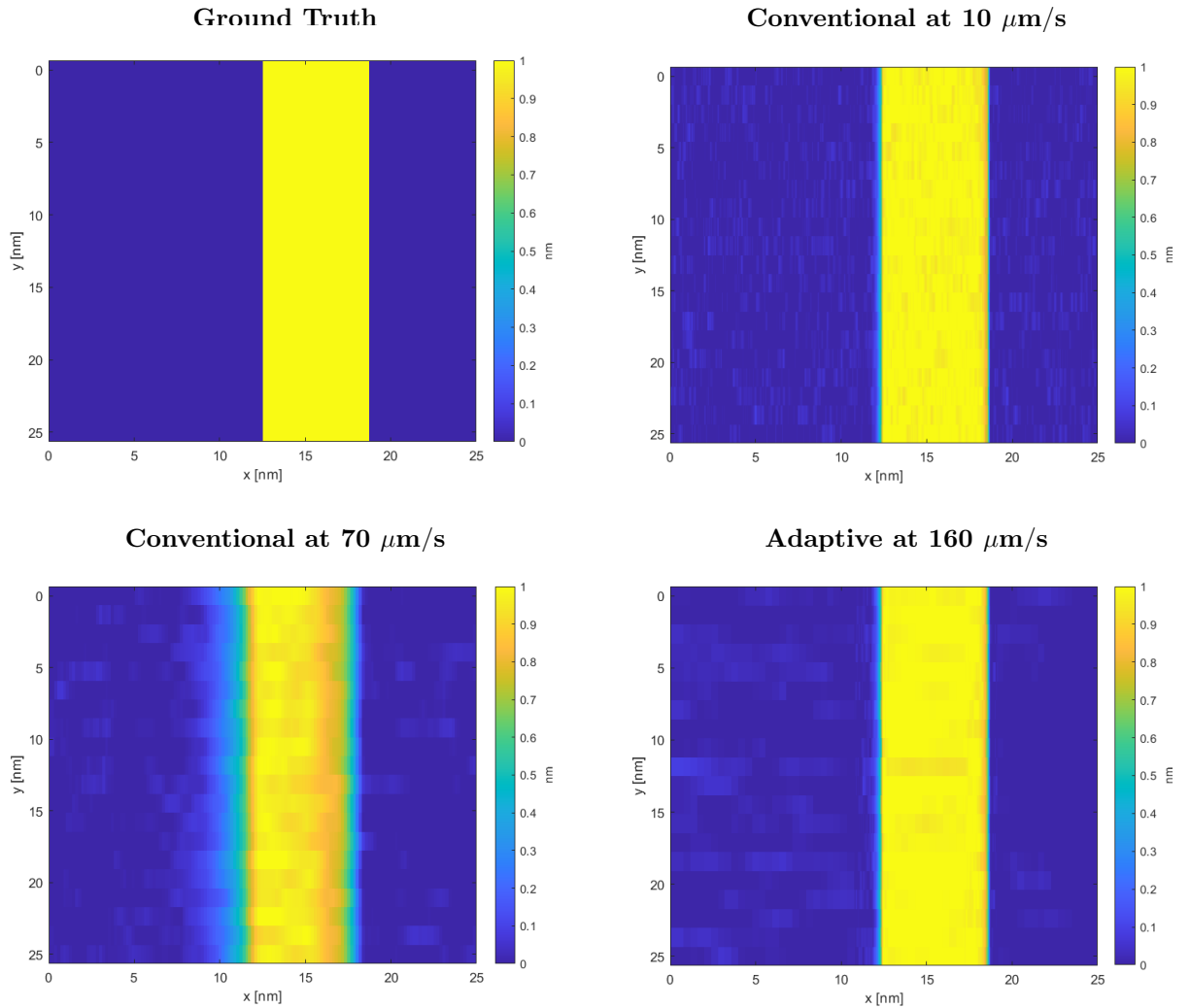


Figure 8.4: Upper left shows the Ground Truth. The right figures show a similar error, namely 0.0110 nm^2 for the conventional scan at 10 $\mu\text{m/s}$, and 0.0121 nm^2 for the adaptive scan at 160 $\mu\text{m/s}$. The bottom figures have a similar scanning time, namely 0.0143 seconds for the conventional scan at 70 $\mu\text{m/s}$, and 0.0138 seconds for the conventional scan at 160 $\mu\text{m/s}$. The scanning time of the conventional scan at 10 $\mu\text{m/s}$ is 0.1 seconds, and the error of the conventional scan at 70 $\mu\text{m/s}$ is 0.0754 nm^2 . This results in 7 times faster scanning and 6.2 times higher spatial resolution.

8.4 Performance Against the Conventional Method

To show the performance of the Adaptive Raster Scanning Method against the Conventional Raster Scanning Method, a visualization has been made in figure 8.5. 20 lines are simulated at a range of 10-500 $\mu\text{m/s}$.

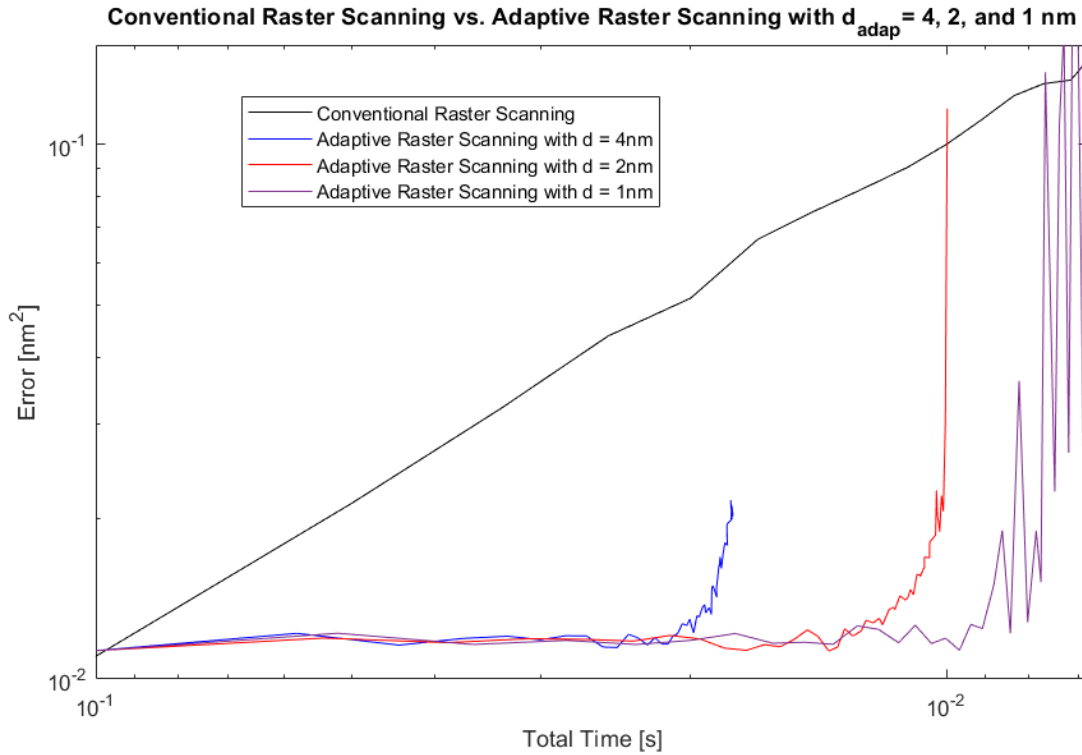


Figure 8.5: The Conventional Raster Scanning method against the Adaptive Raster Scanning method with $d_{adap} = 1, 2,$ and 4 nm. Measurements have been done for 20 lines at scan speeds of 10-500 $\mu\text{m/s}$. Eventually, the maximum scanning speeds that have been reached are within a range of 450-480 $\mu\text{m/s}$. A log-log scale plot is used to visualize the different results.

The Conventional Raster Scanning performance curve shows an increasing error at higher scanning speeds because the total scanning time decreases. For the Adaptive Raster Scanning Method, there can be observed that the error remains constant while the scanning speed increases, followed by a steep increase in error which shows a vertical asymptote.

This vertical asymptote moves to the left direction for larger values of d_{adap} . Furthermore, there is observed that the error will decrease till a lower maximum for larger values of d_{adap} . Next, The Adaptive Scan using $d_{adap} = 1$ nm starts oscillating at scan speeds higher than 210 $\mu\text{m/s}$. Lastly, the simulations for the Adaptive Scans did not reach the maximum scanning speed of 500 $\mu\text{m/s}$ but gave an error between 450-480 $\mu\text{m/s}$.

Observing the conventional performance curve and the different adaptive performance curves, there are ratios determined which are later used to compare the different methods. The most optimal points on the different adaptive scanning curves are chosen, to see what the theoretical limits of this methodology are compared to the conventional method. There are performance

ratios defined concerning the resolution and scanning time. Considering the resolution ratio, there will be observed to what extent the adaptive method is an improvement while having the same scanning time. Regarding the scanning time ratio, there will be observed to what extent the adaptive method is an improvement while having the same resolution. Table 8.1 shows these performance ratios,

Optimal resolution and scanning time ratio			
d_{adap} (nm)	Scan speed ($\mu\text{m/s}$)	Resolution Ratio	Scanning time Ratio
1	170	9.5x	9.4x
2	160	6.7x	6.6x
4	160	4.4x	4.3x

Table 8.1: The data points and calculations that are used for this table are shown in table E.1 and E.2 from Appendix E.

First, there is seen that all optimal scanning speeds of the different values of d_{adap} are in a range of 160-170 $\mu\text{m/s}$. Next, the resolution and scanning time ratios increase for lowering d_{adap} . The resolution and scanning time ratio are both rather similar. Taking d_{adap} at 4 nm as starting point, halving d_{adap} to 2 nm results in a $\approx 53\%$ increase for the resolution and scanning time ratio. Halving d_{adap} again to 1 nm results in another $\approx 42\%$ increase for the resolution and scanning time ratio.

8.5 Performance of the detection algorithm

The performance of the detection algorithm can generally be split into two parts: repeatability and accuracy. The repeatability is determined by how often the algorithm chooses the same time step for its uphill or parachuting event. The accuracy is a measure of how close the measurement is to its true value. This does not imply that it is a measure of the accuracy of the Adaptive Controller itself, but just the detection algorithm. The accuracy of the detection algorithm means how accurately it detects the time points it should detect. Since it is known from the literature that there is a time delay present (section 3.7), this must be incorporated for the 'true value' that the algorithm should detect. This is then the sum of the ground truth and the total time delay. The total time delay is the amount of time that is necessary to detect a parachuting or uphill event.

8.5.1 Repeatability

There is a repeatability analysis made for the detection algorithm. There are scans made with 100 lines per scanning speed and observed how often the algorithm detects the same time point from the output signal. These are put in table 8.2 with its matching percentage. This table shows the repeatability for the speeds at a range of 10-300 $\mu\text{m/s}$. More data for this is shown in table F.1, which shows the repeatability for the speeds at a range of 10-500 $\mu\text{m/s}$.

Repeatability Analysis 10-150 $\mu\text{m/s}$			Repeatability Analysis 160-300 $\mu\text{m/s}$		
Scan Speed ($\mu\text{m/s}$)	Uphill	Parachuting	Scan Speed ($\mu\text{m/s}$)	Uphill	Parachuting
10	100%	100%	160	100%	100%
20	100%	100%	170	100%	100%
30	100%	100%	180	100%	100%
40	100%	53%	190	100%	100%
50	100%	100%	200	100%	63%
60	100%	100%	210	100%	100%
70	100%	100%	220	100%	100%
80	100%	100%	230	100%	100%
90	100%	100%	240	100%	100%
100	100%	100%	250	100%	100%
110	100%	53%	260	100%	100%
120	100%	50%	270	53%	99%
130	100%	100%	280	93%	90%
140	100%	100%	290	67%	100%
150	100%	100%	300	100%	100%

Table 8.2

In general, from table 8.2 can be seen that the detection algorithm has for 85% of all cases a repeatability of 100%, implying that every scan line is detected at the same time point. Analyzing the scan speeds individually, the detection algorithm shows for the uphill event of 280 $\mu\text{m/s}$ and parachuting event of both 270 $\mu\text{m/s}$ and 280 $\mu\text{m/s}$ repeatability of $\geq 90\%$. Furthermore, the parachuting events at 40, 110, 120 and 200 $\mu\text{m/s}$, and the uphill events at 270 and 290 $\mu\text{m/s}$ show repeatability within a range of 50% and 67%.

Averaging the different repeatability percentages result in an overall repeatability of 97.1% for the Uphill events and 93.6% for the Parachuting events. Taking these averages of the scan speeds for a range of 10-500 $\mu\text{m/s}$ (table F.1), the results turn out to be slightly higher for both cases, namely 98.1% and 95.9%.

8.5.2 Accuracy

As said above, the accuracy of the detection algorithm is dependent on the total time delay, since its target is the ground truth value combined with the total time delay by the system. Since the ground truth value is known and constant, the results of the total time delay will only be looked at. At first, the total time delay will be calculated and determined from the simulation results. These result in an estimation of the total time delay, which will then be used to analyze the results for their accuracy.

Time delay from the calculations

The total time delay depends on the cantilever's response time, LIA filter, and PI controller. Similar to the calculation of the settling time, the complete transfer function can not be designed. The LIA filters the output of the cantilever such that it becomes nonlinear which makes it improper to design a transfer function. The time delays for the LIA filter and PI controller are the same as used in equation (6.17) from section 6.9 because these influence the output signal via a constant time delay. The total time delay becomes as follows,

$$\begin{aligned}\Delta t_{total} &= \Delta t_c + \Delta t_{LIA} + \Delta t_{PI} \\ \text{with } \Delta t_c &= C\tau_c = C\frac{Q_c}{\pi f_c}, \\ &= C\frac{1.59}{\pi \times 400 \text{ kHz}} = C \times 1.265 \times 10^{-6} \text{ s}, \\ \Delta t_{LIA} &= \tau_{LIA} = 2.6 \times 10^{-6} \text{ s}, \\ \Delta t_{PI} &= \tau_{PI} = 1 \times 10^{-7} \text{ s}\end{aligned}\tag{8.2}$$

where τ_c has already been used in section 6.9 for the settling time and C is a constant. For C , the condition for the settling time as described in Eq.6.17 does not apply here. The settling time implies that the signal has already been settled below a 2% tolerance band [79]. The detection algorithm already detects the signal at the first slope when it is increasing in magnitude since it is the multiplication of the first and second derivatives. Choosing the settling time would mean that both first and second derivatives are (almost) zero, and is thus not the right time point to choose. Therefore, there must be estimated what percentage on the slope of the step response these uphill and parachuting events are detected. A step response of the cantilever's dynamics is made in figure 8.6 and further analyzed.

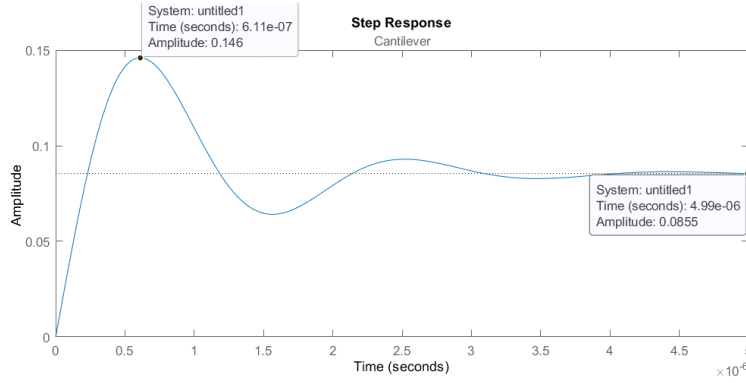


Figure 8.6: The step response on the dynamics of the cantilever. The maximum overshoot is seen after 6.11×10^{-7} seconds.

Analyzing the step response, there can be seen that the steady state value is 0.0855. The maximum overshoot is at an amplitude of 0.146. Considering the first peak of the step response, it shows a steep increase of the amplitude within the first half of the time, followed by a deceleration to go towards its maximum. There can thus be assumed that the detection algorithm probably detects the signal at $\approx 50\%$ of this first slope. Next, the following calculation can be done:

$$\text{Detected point: } 50\% \times 0.146 = 0.073$$

Percentage of the detection point at the steady-state value:

$$0.073/0.0855 \times 100\% \approx 85\%$$

Results into the following equation for t

$$0.85 = (1 - 10^{-t/\tau})$$

$$t \approx 1.9\tau$$

Constant $C = 1.9$ can be filled in for Eq.8.2, leading to the following result:

$$\begin{aligned} \Delta t_{total} &= \Delta t_c + \Delta t_{LIA} + \Delta t_{PI} \\ \Delta t_{total} &= C \times 1.265 \times 10^{-6} + 2.6 \times 10^{-6} + 1 \times 10^{-7} \\ \Delta t_{total} &= 5.104 \times 10^{-6} \text{ s} \end{aligned}$$

Thus, the total time delay Δt_{total} can be estimated at 5.104×10^{-6} s. Converting the time delay towards the number of time steps, we get $\frac{5.104 \times 10^{-6}}{1 \times 10^{-7}} = 51$ Time steps. This calculated value will be used to compare with the time delays that are retrieved from the simulation measurements.

Time delay from the simulation data

From the simulation data, the time delay is determined as a function that takes the difference between the time point of detection and its ground truth value as shown below:

$$\text{Total Time Delay} = \text{Detection Point} \times 25 - \text{Ground Truth Value} \quad (8.3)$$

The detection point must be multiplied by the period since it's a filtered signal from the LIA that only takes the minima from every period which contains 25 time steps.

Table 8.3 shows the time delay for the uphill and parachuting events at a range of 10-300 $\mu\text{m/s}$. More data for this is shown in Appendix G, which shows the time step offsets for the different events at a range of 10-500 $\mu\text{m/s}$.

Time Delay within 10-150 $\mu\text{m/s}$				Time Delay within 160-300 $\mu\text{m/s}$			
Scan ($\mu\text{m/s}$)	Speed	Uphill	Parachuting	Scan ($\mu\text{m/s}$)	Speed	Uphill	Parachuting
10		49	49	160		42	51
20		49	49	170		38	45
30		57	48	180		29	31
40 (53%-47%)		49	36-61	190		41	37
50		49	49	200 (63%-37%)		49	36-61
60		40	48	210		53	55
70		38	45	220		30	45
80		36	29	230		55	58
90		60	65	240		28	42
100		49	49	250		48	47
110 (53%-47%)		62	43-68	260		43	27
120 (50%-50%)		57	36-61	270 (47%-53%)		36-61	54
130		37	56	280		27	53
140		56	59	290 (33%-67%)		42-67	51
150		40	48	300		57	48

Table 8.3: Table for the time delays at the different scan speeds. Note that for the scan speeds where the repeatability is <90%, both offsets are set into the table, together with their time delay values.

In general, there can be observed that the different time delay values are not showing the same value. Further analyses can be done which might result in a value for the time delay from the simulation results.

First, let us define the sample in time steps with the formula in Eq. 6.16: $n = \frac{L_s}{V_H t_s}$. This results in rounding errors for most of the scan speeds since the arrays defined by Matlab only accept integers. For example, a sample with $V_H = 190\mu\text{m/s}$ results in $n = \frac{25 \text{ nm}}{190 \mu\text{m/s} \times 1 \times 10^{-7} \text{ s}} = 1315.79$ time steps which will be rounded towards 1316 time steps such that it can be processed before a new line scan is done.

However, there are some scan speeds in which no rounding is required, namely 10, 20, 40, 50, 100, 200, and 250 $\mu\text{m/s}$. These are shown once again in table 9.1 to give an overview and be able to discuss the results clearly.

Time Delay with the scan speeds that require no rounding			
Scan Speed ($\mu\text{m/s}$)	Uphill	Parachuting	Number of Time Steps per line
10	49	49	25000
20	49	49	12500
40 (53%-47%)	49	36-61	6250
50	49	49	5000
100	49	49	2500
200 (63%-37%)	49	36-61	1250
250	48	47	1000

Table 8.4: Table for the time delays that require no rounding for determining its array size

For these results, there can be seen that there is some repeatability present for the time delay. For these scan speeds, the total time delay can be estimated at 49 time steps. At 40 and 200 $\mu\text{m/s}$, the average offset between 36 and 61 is 48.5, which can be rounded to 49 time steps as well.

Comparing the calculations with the simulation results

From the calculations was shown that the total time delay is 51 time steps. From the simulation results could be seen that the total time delay could be estimated to be 49 time steps for the scan speeds where the sample size has not been sampled. The scan speeds that show rounding errors for their sample arrays in Matlab are not in line with the upper results.

8.6 The Circle Scan

Another type of Ground Truth is used to show its applicability on a different shape instead of just a line scan, which is here a circular shape. Figures 8.7 show the Circle Ground Truth versus the Conventional Raster Scan at 10 and 90 $\mu\text{m/s}$ and the Adaptive Raster Scan at 170 $\mu\text{m/s}$. Conventional Raster Scan at 10 $\mu\text{m/s}$ shows a similar error value to the Adaptive Raster Scan, and the Conventional Raster Scan at 70 $\mu\text{m/s}$ shows an equal scanning time.

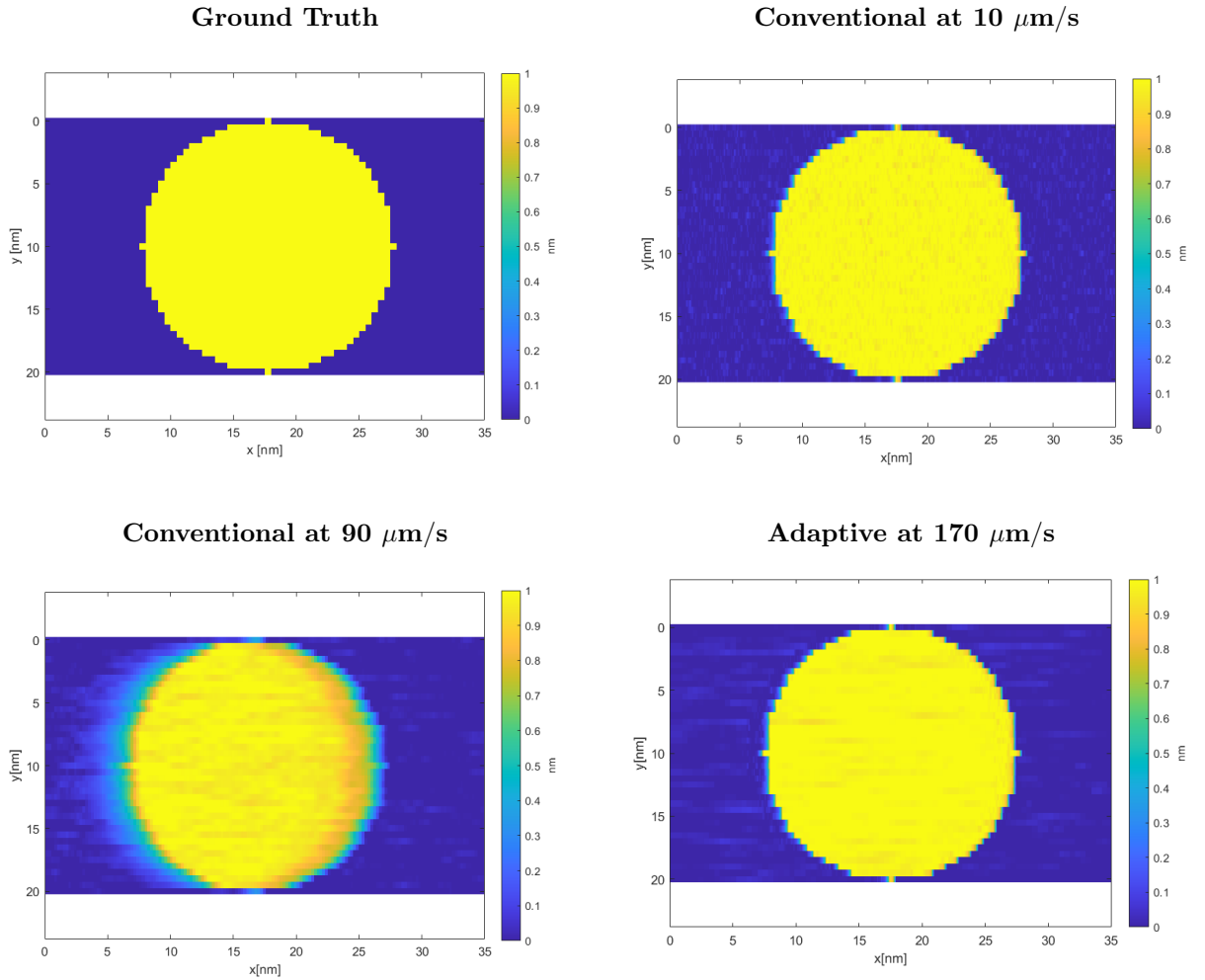


Figure 8.7: Upper left shows the Circle Ground Truth. The right figures show a similar error, namely 0.0080 nm^2 for the conventional scan at 10 m/s , and 0.0089 nm^2 for the adaptive scan at 170 m/s . The bottom figures have a similar scanning time, namely 0.0319 seconds for the conventional scan at 90 m/s , and 0.0323 seconds for the conventional scan at 170 m/s . The scanning time of the conventional scan at 10 m/s is 0.2870 seconds, and the error of the conventional scan at 90 m/s is 0.0692 nm^2 . This results in 8.9 times faster scanning and 7.8 times lower error for the Adaptive Raster Scanning Method on a circle scan.

Chapter 9

Discussion

In this chapter, the results and limitations will be discussed. First, the process of how to account for the step response is discussed. After that, the detection algorithm will be discussed whereafter the performance analysis of the Adaptive Raster Scanning Method is discussed, combined with potential improvements. Finally, the circular scan is discussed.

9.1 Accounting for the Step Response

During the first simulations, a large error occurred at the beginning of the measurement as a result of the settling time from the interaction between the cantilever and the sample that caused a step response. This step response caused large disturbances by the detection algorithm for the uphill and parachuting time points. They also led to a larger resolution error as they do not follow the ground truth of the sample height, resulting in bad imaging.

This problem was effectively tackled by extending the sample based on the settling time of the system because it did not bring up the problems anymore which were present in the first case. However, there are some points to address considering the method that is used to cope with the settling time of the system.

At first, it would be most accurate to determine the step response of the complete system, instead of every component individually. The system could be set into a closed-loop system on which a step response could have been done. From the transfer function of the closed loop system, the total Q factor and settling time could be achieved and compared to the simulation results later in this report.

However, it is not possible to define a transfer function for the closed-loop system. The LIA filters the output of the oscillating cantilever, which makes it nonlinear and thus improper to calculate its transfer function.

The calculated settling time of 332 time steps from Eq.6.20 in section 6.9 turned out to be 407 time steps for the simulation as shown in figure 8.1 from section 8.2. Reading the settling time from the graph was meant to show the similarities within the order of magnitude, which can be seen as a good estimation with a 19% offset compared to the calculations. For both the calculations and reading from the graph, there are some uncertainties. At first, there is a presence of noise. The average RMS value has not been taken into account, but might influence the choice of the number of time steps from reading the graph for the total settling time. Furthermore, step responses contain a dead time which is not considered an element within the settling time, but does affect the total time as described via the method that is used in this report. Finally, the signal was read at the condition for crossing the $h=0$ line. Normally, and also for this method with $T_s = 4\tau$, settling times are determined within 5% and 2% regions. There can be said that the signal should not have passed the $h=0$ line to be seen as well saturated for these tolerance bands.

Lastly, considering the condition that there are at least ≈ 400 extra time steps required to settle the signal, the assumption of taking 30% of a total line scan is valid till a certain scan speed. The higher the scan speed, the fewer time steps are required to finish one line scan. Taking 30% of a decreasing amount of time steps results in a smaller amount of time steps that are added for

the extended signal to let the signal settle. Calculating this scanning speed is shown in Eq.9.1.

$$\begin{aligned}
 n &= 0.3 \frac{L_s}{V_H t_s} \\
 V_H &= \frac{0.3 L_s}{n t_s} \\
 V_H &= \frac{0.3 \times 25 \text{ [nm]}}{400 \times 1 \times 10^{-7} \text{ [s]}} \\
 V_H &= 187.50 \mu\text{m/s} \approx 190 \mu\text{m/s}
 \end{aligned} \tag{9.1}$$

This implies that the settling condition for at least 400 time steps holds till a scan speed of $\approx 190 \mu\text{m/s}$. However, only the first 140 time steps are the main problem since this interferes with the detection method for the parachuting and uphill points, which is visualized in figure 9.1. Following the same methodology, as shown in Eq.9.1, this implies that the detection method at scan speeds higher than $\approx 540 \mu\text{m/s}$ becomes invalid because this might interfere with the detection algorithm.

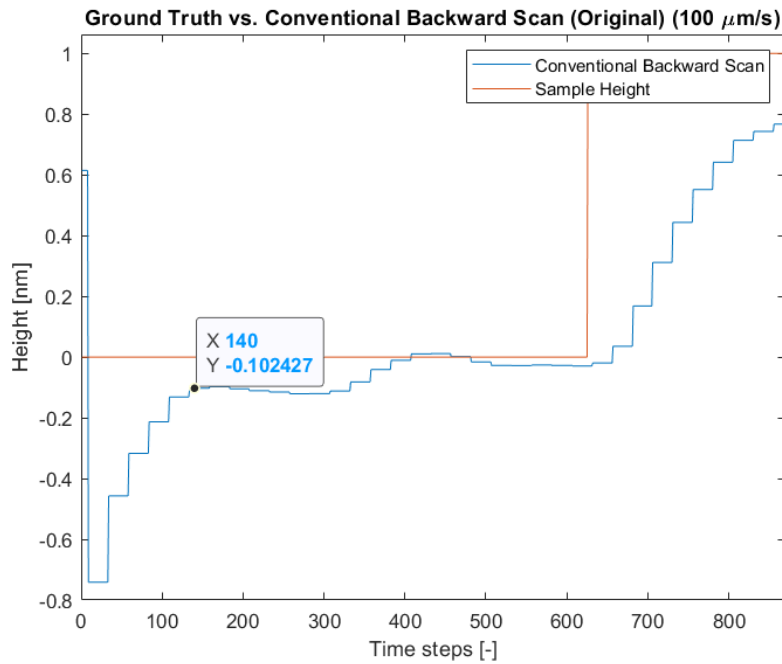


Figure 9.1: A close-up on the step response at the start of an original line scan. This shows the largest deflection till 140 time steps which is the main problem of having a step response at the start of a simulation. This could interfere with the detection algorithm where the uphill and parachuting time points are determined. Furthermore, it also adds additional errors when the validation process of the least-squares fit is done.

9.2 Performance of the detection algorithm

The results of the repeatability and accuracy of the detection algorithm are discussed below. From this discussion, the performance of the detection algorithm is described whereafter potential improvements are mentioned. Furthermore, the limitations of the detection algorithm are discussed, together with possible solutions.

9.2.1 Repeatability

Analyzing the results from section 8.5.1, there was seen that the detection algorithm had an overall repeatability of 97.1% for the Uphill events and 93.6% for the Parachuting events. From these numbers, there can be said the detection algorithm has high overall repeatability.

Comparing the repeatability values for the scan speeds from table 8.2, some differences can be discussed. For 85% of all scan speeds, the detection algorithm has a perfect score of 100%. This means that every scan line is detected at the exact same time point. Another 5% shows repeatability between 90% and 100% which can still be considered very high. For the remaining 10% of all uphill and parachuting events, the repeatability turned out to be in a range of 50% and 67% which is moderately high. These cases are further analyzed with their time delay as shown below:

Scan speeds with low repeatability and their time delay values		
Scan Speed ($\mu m/s$)	Uphill	Parachuting
40 (53%-47%)	49	36-61
110 (53%-47%)	62	43-68
120 (50%-50%)	57	36-61
200 (63%-37%)	49	36-61
270 (47%-53%)	36-61	54
290 (33%-67%)	42-67	51

Table 9.1: Table for the time delays that require no rounding for determining its array size

At 40, 120, 200, and 270 $\mu m/s$ there could be an alternating behavior present between the values 36 and 61. From section 8.5.2, there was shown that the total time delay resulted in 49 time steps for the simulations, which is the average of 36 and 61. From Eq.8.3 there is seen that the total time delay is defined as a multiple of 25 time steps, meaning that the value 49 cannot be physically reached at these scan speeds. Depending on the noise levels, the detection algorithm chooses either the time point before or after the correct time point.

At 110 and 290 $\mu m/s$, this theory does not hold as their averages are ≈ 55 time steps. To understand what might cause this difference, figure 9.2 is made to compare both cases.

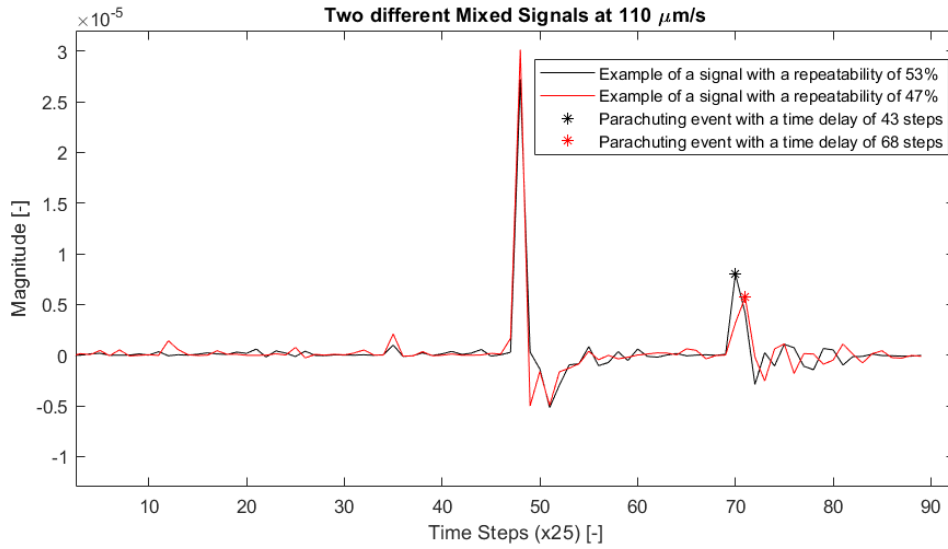


Figure 9.2: For the simulation at $110\mu\text{m}/\text{s}$, two types of outcome were present considering the repeatability of the parachuting event: 70 and 71 time steps, resulting in a 43 and 68 time delay (from Eq.8.3) Furthermore, from section 9.1 is seen that the noise levels at the start of a signal become unreliable at scan speeds higher than $190\mu\text{m}/\text{s}$. Therefore, a speed of $110\mu\text{m}/\text{s}$ is used instead of $290\mu\text{m}/\text{s}$.

Comparing the parachuting events, there can be seen that the black line has a higher magnitude than the red line. This is probably caused by the presence of noise. During the first time steps, the output is dominated by the noise since there is no difference in sample height present yet. The maxima that are present for this part of the signal, show a similar maximum in magnitude for its height compared with the difference in magnitude between both parachuting events. Furthermore, it could also be caused by how the cantilever has tapped on the sample. This could give an interaction that is very sensitive to noise. More details on these interactions are explained in section 9.2.2. Since every scan line is the same, every interaction point is sensitive to the presence of noise.

This could be prevented by using samples higher than the current 1 nm. This will cause higher magnitude peaks for the mixed signal. The relative effect of the presence of noise will then become less, resulting in a better detection algorithm.

9.2.2 Accuracy

From the results in section 8.5.2, the differences between the calculation and simulation can be discussed. The total time delay calculated from the theory and step response of the system resulted in 51 time steps. From the simulation results, an estimation of 49 time steps had been found at the scan speeds that did not face any rounding procedure for its calculations. From this, there can be suggested that the total time delay can be estimated at ≈ 50 time steps, or 2 periods because one period consists of 25 time steps.

Comparing this result with table 8.3, some strong differences can be discussed for the remaining scan speeds that require a rounding procedure.

There is a handful of events that are in line with the estimation of 50 time steps. Considering the uphill events, only $270 \mu\text{m}/\text{s}$ is in line with this approximation. For the parachuting events, 30, 60, 120, 150, 160, 290, and $300 \mu\text{m}/\text{s}$ are in line with this approximation. Combining these with table 9.1, there are 22 events that are in line with this approximation, or 37%. The remaining 63% of the events are within a range of 27 and 68 time steps. From this, there can be said that the detection algorithm is not quite accurate.

The observation that most of the scan speeds are not in line with the estimated total time delay, can be explained by the LIA filter and interaction point between the cantilever and the sample. At first, the interaction point will be discussed, and after that the LIA filter.

Interaction point between Cantilever and Sample

Varying the scan speed will change the interaction point where the cantilever taps the sample. Figures 9.3a-9.3f show the interaction points where the cantilever taps the sample at an uphill event for different scan speeds. From this, the differences in time delay can be explained.

Analyzing figures 9.3a, 9.3b, and 9.3c, there can be seen that the interaction points at 10, 50 and $100 \mu\text{m}/\text{s}$ are quite similar. The cantilever taps just past the edge and taps the surface during its next period. This shows how these scan speeds result in the same time delay of 49 time steps. Since there is no rounding procedure necessary for these scan speeds with the current parameters, the tapping interaction is the same, and thus a similar time delay.

More interesting are the differences between the remaining scan speeds that are inaccurate since they show time delays within a range of 27 and 68 time steps. Figures 9.3d, 9.3e, and 9.3f show the interaction of 150, 180, and $290 \mu\text{m}/\text{s}$. Recalling from table 8.3, these showed a time delay of 40, 29, and 68 time steps, respectively. The figures show that when varying the scan speed, the interaction point changes, causing the time delay to shift. The differences are discussed below:

At $150 \mu\text{m}/\text{s}$ in figure 9.3e, the cantilever hits the sample at the corner of the sample. This leads to a time delay which is not too much of the estimated time delay, namely 40 time steps.

At $180 \mu\text{m}/\text{s}$ in figure 9.3e, the cantilever seems to penetrate the sample which causes a steep increase in its magnitude. This steep increase might have triggered the detection algorithm too early, resulting in a total time delay of 29 time steps.

At $290 \mu\text{m}/\text{s}$ in figure 9.3f, the cantilever seems to softly tap the sample such that it gets not triggered by the detection algorithm. This causes a less steep increase which triggers the detection algorithm too late at a time delay of 68 time steps.

The uphill events at 180 and $290 \mu\text{m}/\text{s}$ seem to be outer bounds. The first is too close to the sample and penetrates it, leading to a low time delay. The second taps too softly, leading to a large time delay.

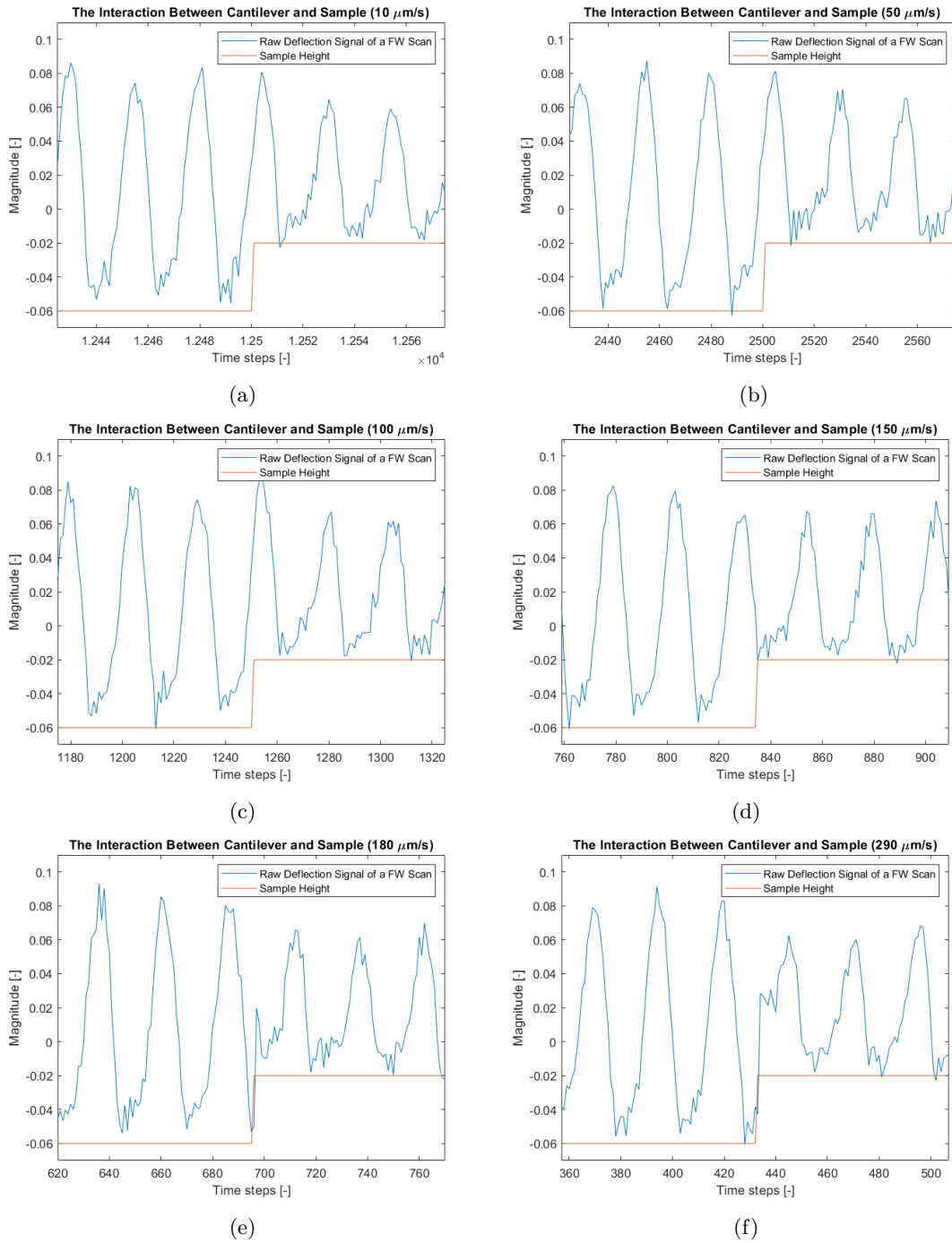


Figure 9.3: The interaction between the cantilever and sample is shown for the scan speeds 10, 50, 100, 150, 180, and 220 $\mu\text{m/s}$. 10, 50, and 100 $\mu\text{m/s}$ showed the same time delay, namely 49 time steps. 150, 180, and 290 $\mu\text{m/s}$ showed differences for the time delay, namely 40, 29, and 68 time steps, respectively.

Moreover, the rounding procedure as explained in section 8.5.2 causes a lower scan speed for the simulation. As explained in section 8.5.2, a sample with $V_H = 190\mu m/s$ resulted in 1315.79 time steps, which was rounded upwards to 1316 time steps. The same amount of time steps had been used as input signal, such that these arrays have the same length to be processed in Matlab. However, the sample width L_s and sample time t_s had not been modified for this rounding procedure. Following Eq.6.16: $n[-] = \frac{L_s[nm]}{V_H[nm/s]t_s[s]}$, it implies that the scan speed will change when the rounding procedure is performed. For $n = 1316$ time steps, this results in $V_H = \frac{25\text{ nm}}{1316 \times 10^{-7}\text{ s}} = 189.97\mu m/s$. Since the scan speed is therefore not exactly the value that has been set, it could influence the accuracy of the detection point slightly. From these two discussion topics, there can be said that the interaction point between the cantilever and sample is dependent on varying the scan speed.

LIA filter

The LIA filters the raw deflection signal towards a signal such that the magnitude is constant for 25 time steps since. It is not known where on this line the minimum of the period lies because this has been averaged by the LIA.

Recalling a signal used in this report, for example, figure 7.6 from section 7.2 which has been shown once again in figure 9.4a. A close-up from this in figure 9.4b shows that when the magnitude changes, it remains constant for 25 time steps. This implies that the measured minimum of an oscillation lies between the black and red star, but it is unknown where exactly. The detection algorithm is built such that it always chooses the first time step that changes in magnitude, thus the black star. If the minimum of the oscillation lies at the red star, the value of the black star will still be the output. This result in an uncertainty of maximum 24 time steps.

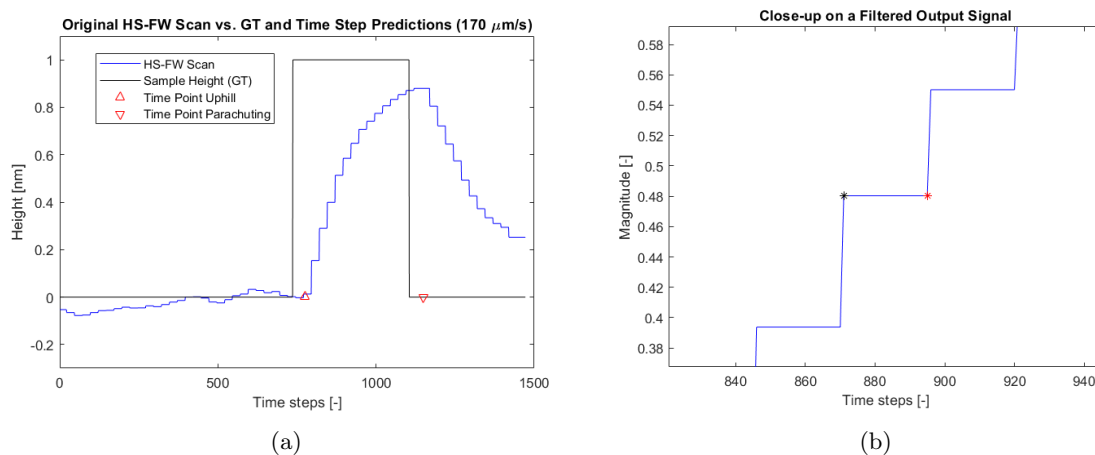


Figure 9.4

From the analysis of the interaction point between the cantilever and sample and LIA filter can be said that there is uncertainty for the detection algorithm. This uncertainty has a maximum of 25 time steps, since that is the length of one period. Altogether, the accuracy of the detection algorithm can then be settled towards a domain of 50 ± 25 time steps within this configuration.

In order to improve the accuracy of the detection algorithm, the uncertainty of ± 25 time steps on the time delay should be decreased. This can be done by taking a cantilever with a higher

frequency. A higher frequency implies a smaller period, which results in a lower uncertainty for the detection algorithm. The total time delay itself will decrease as well, but this is not the main issue since there can be accounted for that within the controller.

Next, the raw deflection signal can be used to improve the accuracy of the detection algorithm. For the current configuration, the filtered signal is used which shows a new magnitude point at every 25th time step. There is information thrown away because it is currently unknown at which exact time point an event occurs between the cantilever and the sample as a result of this filtering approach. However, the raw deflection signal is very sensitive to noise, so replacing the LIA output signal with the raw deflection signal would become a mess in detecting the different events.

A possibility could be to use the current method to 'guess' the area where an event occurs, and use the raw deflection signal to specify the exact data point. For instance, looking at the raw deflection signals in figures 9.3a-9.3f, there can be guessed where the sample is present just by observing the raw deflection signal itself. Having the outer boundaries where it does not hit the sample yet (at $100\mu\text{m/s}$ in fig.9.3c), and where it hits the sample exactly at the corner (at $150\mu\text{m/s}$ in fig.9.3d), the uncertainty can be decreased severely towards approximately half a period. The signals that show a penetrating behavior of the sample by the cantilever (at 180 and $290\mu\text{m/s}$ in fig.9.3e and 9.3e), can be estimated rather easily because the moment of impact is observed.

9.2.3 Limitations

Currently, the simulation only works for only 2 events (a combination of parachuting and/or uphill). This is a result of picking two maxima from the mixed function of the two derivatives as shown in figure 7.4. A better approach would be to choose the time points with a certain threshold, or as a function of the averaged RMS value. With such a condition, every parachuting and uphill event could be detected. Important to note is that this threshold or ratio should be dependent on the height of the sample as well. For samples with a lower height, the magnitude of the peaks within the mixed function will become lower. This makes it more difficult to distinguish it from the RMS level.

9.3 Performance of the Controller

The performance of the controller is discussed by explaining the differences for using $d_{adap} = 1$, 2, and 4 nm. Next, there will be discussed how it could scan samples with different heights and smaller widths.

9.3.1 Varying factor d_{adap}

Studying the results from figure 8.5 and table 8.1, there can be seen that the performances of the Adaptive Raster Scanning Methods show both a strong decrease in error and are more time efficient. At $d_{adap} = 1$ nm, there is an improvement of up to 9.5 times for the spatial resolution, and it is 9.4 times more time efficient. At $d_{adap} = 2$ nm, these values are slightly lower toward 6.7 and 6.6, respectively. At $d_{adap} = 4$ nm, the lowest improvements are seen, which are 4.4 and 4.3, respectively.

Moreover, from figure 8.4 can be observed that the effect of parachuting has decreased drastically while enhancing the same scanning time. Figure 8.5 shows that the Adaptive Raster Scanning Method shows better performances till the vertical asymptotes of $d_{adap} = 1$ nm and $d_{adap} = 2$ nm. This is because within this domain their performance curves are below the Conventional

Raster Scanning Method curve which then shows better combinations for having the lowest error and least scanning time.

Considering the Adaptive's performance curves, all three are constant for a significant amount of scanning speeds. The reason is that the settling time of the parachuting and uphill events fit within the slow scanning areas set up by d_{adap} . This means that it does not matter whether the excess space of a line scan will be scanned at a high speed, because its height is constant.

Still, a vertical asymptote is present for the different adaptive performance curves. The first reason is that for scanning speeds higher than $190\mu m/s$ the signal is not settled anymore at the start of the simulation as described in section 9.1. This leads to an increasing error at higher speeds. Secondly, following equation (7.2), t_{up} and t_{par} decrease at higher speeds. This makes the controller more sensitive for a large offset of the time delay. There is an increasing risk that the signal has not been settled yet before it will be scanned at a high speed again, leading to larger errors. If the time delay is larger than t_{up} and/or t_{par} , the Adaptive's approach will not scan the uphill and parachuting regions at a lower speed which causes a gigantic error. This can be partly solved by using a larger value for d_{adap} , as shown in figure 8.5, such that there is enough space to let the signal settle.

Choosing a lower value for the slow scanning speed of $10\mu m/s$ would mean that a shorter distance of d_{adap} is required because the signal is quicker saturated. In order to keep the same resolution within this slow scanning range, the distance of d_{adap} must decrease the same order as V_L because these have a linear relationship. This is also mathematically shown by equation (7.3) in section 7.2.1.

Furthermore, varying d_{adap} causes performance differences for the minimum scanning time and maximum error.

For the first observation, the controller is the fastest at $d_{adap} = 1$ nm, because the smallest distance is scanned at a slower speed. It will scan the areas that are most necessary to scan at a lower speed and thus can be seen as most efficient considering these three parameters. Furthermore, it contains the points with the lowest error for its total time, which can thus be considered the best performance points before it starts oscillating.

For the second observation, the controller is most robust at $d_{adap} = 4$ nm, because the performance line shows the lowest errors overall. This is because a larger area is scanned at a slower speed. The signal has then more time to settle, which works more robust for badly determined detection points as a result of the inconsistent time delay as discussed in 9.2.2.

A higher value for d_{adap} is also capable of reaching higher scanning speeds. Where the performance line of $d_{adap} = 1$ nm starts showing an oscillating pattern at speeds higher than $210\mu m/s$. This behavior is determined by the decreasing value of t_{up} and t_{par} at higher scanning speeds, combined with an inaccurate time delay of ± 25 time steps. Choosing a value of $d_{adap} = 1$ nm will then not be enough to compensate for these effects. Thus, factor d_{adap} settles a trade-off between robustness and scanning efficiency.

Of course, there are other alternatives to determine a changing variable for this Adaptive Raster Scanning method. There could be chosen to set up ratios between the high and low scanning speeds, where the total performance curves can be distinguished by different ratios.

Next, the performance lines of $d_{adap} = 2$ nm and $d_{adap} = 4$ nm showed valid answers till a speed of $450 - 480\mu m/s$. This is a result of an overload within the array. The array size decreases at higher scanning speeds but the time delay remains constant. Eventually, using the expressions for t_{up} and t_{par} , the code wants to call array integers that fell out of the array size. This can be fixed by rewriting the code such that it first gets extended to a new array size before it is assigned to new numbers.

As mentioned in section 8.4, the factor d_{adap} causes a horizontal shift of the vertical asymptote as shown in figure 8.5. This horizontal shift can be analytically determined by determining the relationship between d_{adap} and the total time t_{total} ,

$$t_{total} = (L/V_H) \times (2W + (\frac{V_H}{V_L} - 1) \times N \times d_{adap}) \quad (9.2)$$

Where L is the number of lines and N is the number of parachuting and uphill events. V_H is the high scanning speed and V_L is the low scanning speed, both in nm/s. W is the width of the sample and d_{adap} is the variable we are interested in, both in nanometers.

There can be seen that d_{adap} has an affine relationship with the total time t_{total} .

Furthermore, $t_{up} = t_{par}$ since d_{adap} has been chosen the same for both, but this can be varied to put a better imaging quality on either the uphill or parachuting part. An analysis can be done to measure the error for these specific domains individually, and if necessary, apply a different strategy.

Considering the optimal resolution and scanning time ratios in table 8.1, there is seen that the optimal scanning speed is rather similar for all three different values of d_{adap} , namely 160-170 $\mu\text{m/s}$. There could be suggested that this scanning speed is most optimal for this methodology, but more measurements are necessary to draw this conclusion.

9.3.2 Different sample dimensions

The current sample has a height of 1 nm and a length of 6.25 nm. If the sample has a sample different than 1 nm, the variable chosen for d_{adap} should change as well to get similar results. Samples lower than 1 nm will saturate much faster and thus will require a lower d_{adap} to achieve the same resolution. This would result in faster scanning.

The reverse holds for samples higher than 1 nm, they will need more time to saturate, and thus d_{adap} should be chosen higher to achieve similar results for the resolution. This would result in slower scanning.

A smaller length for the sample would eventually lead to bad detection of the uphill and/or parachuting events, an example with a length of 0.5 nm is shown in figure 9.6.

This can be solved by using the RMS value to detect the uphill and parachuting events instead of the maxima as mentioned in section 9.2.3. By using the RMS value, it will not detect the next event since the width of the sample is too narrow. However, this is not even necessary because detecting the first event gives enough room to scan both combinations of uphill and/or parachuting as the sample is assumed to be narrow.

9.4 Circle scan

In section 8.6, a Circular Ground Truth has been tested to show its applicability on different shapes. There can be seen that the error decreased by a factor of 7.8 for settings with similar scanning times. The scanning time turned out to be 8.9 times quicker. There can thus be said that also for different shapes, the Adaptive Raster Scanning Method shows an improved result. Furthermore, from figure 8.7 there is clearly seen that the effect of parachuting has decreased severely while enhancing the same scanning time.

However, there is an important limitation considering its detection accuracy. Samples with a small width can be (partly) skipped for higher scan speeds. Also, it can occur that the controller does not have sufficient time to settle towards its new position. An example is shown in figure 9.5.

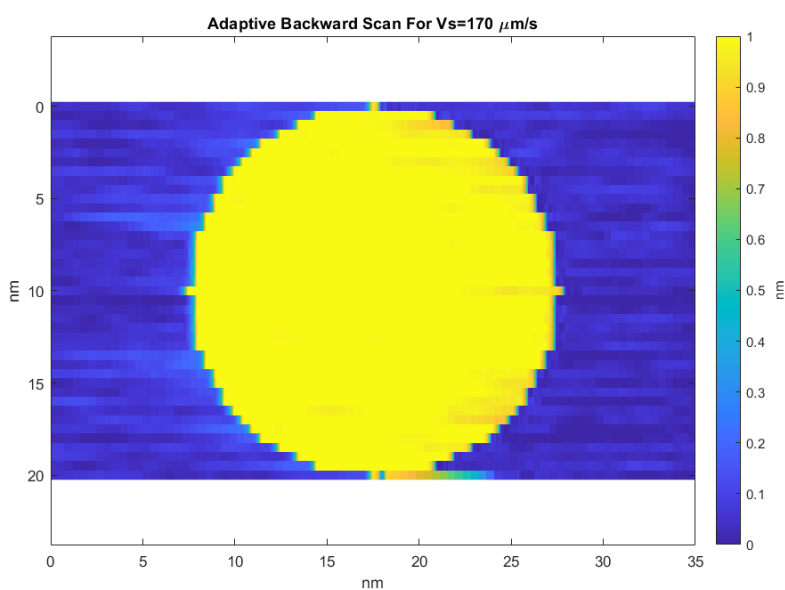
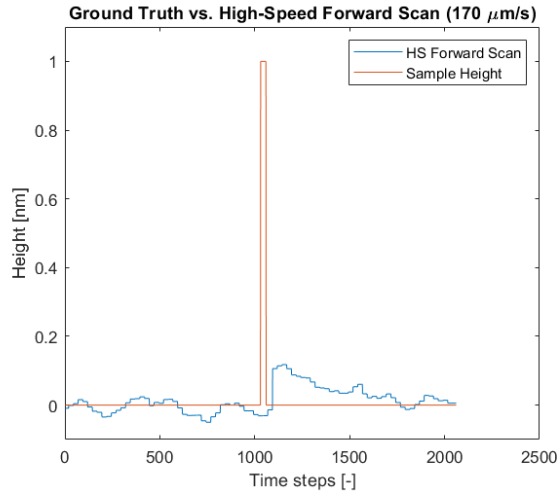


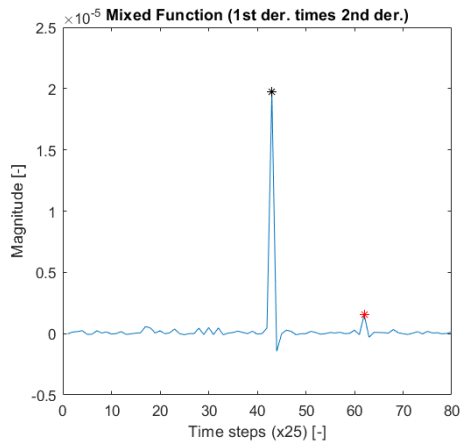
Figure 9.5: An example that shows a circle scan with a wrong line (the bottom one - line 41). The width of this line is 0.5 nm

There can be seen in this image that the bottom line is wrongly scanned as a result of a higher scan speed for a sample with a small width (0.5 nm). Such small widths and high speeds make it difficult for the algorithm to determine the exact time point where parachuting occurs. An analysis of a wrong estimation from a signal is shown in figure 9.6. The mixed function should detect the parachuting right after it detected an uphill effect. However, it missed it which resulted in a wrong estimation for the detection of parachuting, leading to a wrong scan line in figure 9.5. As mentioned above, using an RMS approach for the detection algorithm could already solve this problem.

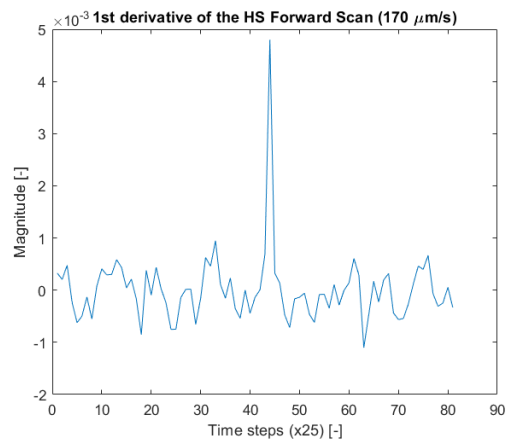
Still, there cannot be said that the algorithm will fail every time under these circumstances, as the upper line in figure 9.5 is correct and has a width of 0.5 nm as well.



(a)



(b)



(c)

Figure 9.6: In 9.6a, The original signal shows that there is a detection of the sample present. 9.6b shows the mixed function, where the first derivative is multiplied by the second derivative. The two maxima (42 and 61) are highlighted and used by the algorithm as detection points. From 9.6c, it must become clear whether these detection points are showing an uphill or parachuting behavior. 43 shows an uphill behavior (1st diff is positive) and 62 parachuting (1st diff is negative). Reflecting these detection points on the original signal in 9.6a, there can be said that the detection of parachuting is wrong.

9.5 Horizontal drift

There is assumed that the speed can change instantaneously during a line scan. In practice, there are effects of accelerating and decelerating which should be taken into account. These effects will cause horizontal drift as you are applying forces on the X piezo actuator [80]. Also, the rates for acceleration/deceleration are bounded by the characteristics of the experimental setup. Before any experiments are performed, it is useful to research and model these effects and account for them. Different drift compensation techniques exist that could be used here [26, 29, 80, 81].

9.6 Resolution

There can be said that the distance between two lines is a measure of their resolution, as the more lines you use on the same sample, the better its resolution. However, this is totally irrelevant to the purpose of this report which shows its proof-of-concept. It does not have any influence on the parachuting effect for the simulation which is the main problem that was issued. However, it could have some influence on experimental setups. Here, the amount of lines is determined by the speed of the slow scan axis. If the speed of the slow scan axis is too high, some parts might be skipped which will result in bad imaging and a low resolution in the vertical direction.

9.7 Simulation time

It requires simulation time for the controller to calculate the adaptive backward line, which happens between the forward and backward lines. This is strongly dependent on the computer that has been used for the simulation. Thus, this has not been considered and should be taken into account when experimental measurements are done.

Chapter 10

Toward Real-life Implementation

In this section, the methodology for the practical implementation of an AFM will be described. Currently, there is a proof-of-concept for the Adaptive Raster Scanning method, but performing experiments are necessary to prove its working principle.

The JPK Nanowizard will be taken as a practical example to work from as its characteristics have been used for the simulation, and it is present at the TU Delft.

As described in the literature in section 2, the AFM consists of 4 piezo actuators which are attenuated individually. Normally, the software on the AFM determines the signals that are sent through these piezo actuators, but it is possible to take over its control and send both pre-programmed and real-time signals externally. Real-time signals are signals to the AFM that are generated online during the experiment. The input for the controller is then the filtered deflection signal of the forward scan, and the output will be a set of variable scanning speeds converted to the correct voltages of the backward scan. Thus, for solely controlling the X and Y direction, the X and Y piezo actuators should be real-time controlled externally.

The piezo actuators for the cantilever and Z-axis should still be controlled by the conventional software on the AFM. This implies that the feedback loop for the AM-AFM mode must be set up in its general settings.

10.1 JPK Nanowizard

As mentioned previously, the JPK Nanowizard 4 is an option to perform the measurements. Since the JPK is present at the PME lab of the TU Delft, the procedure will be explained for this type of AFM [66].

10.2 Break-out box

For some AFM setups, the signals can be controlled externally relatively easily when the ports are already available. However, for some setups (like the JPK Nanowizard 4), a break-out box is required which gives access to send external signals to the AFM. The break-out box of the JPK Nanowizard is called the Vortis Combi Controller [82]. This break-out box only contains BNC connections that are suitable for reading and writing signals.

10.3 FPGA

A Field-Programmable Gate Array is convenient and common to use for sending external signals toward the break-out box of the AFM. An FPGA is an integrated circuit that can be configured by the customer by the customer after it has been manufactured [83]. The code for the control loop with the detection algorithm can be generated on the FPGA controller to read and write real-time signals.

10.4 Sample

The sample that was currently present by the supervisors, was the *CS-20NG AFM XYZ calibration standard, 20nm Z* by Micro to Nano [84]. This sample has a height of 20nm, and pitch sizes that vary between 10 μ m, 5 μ m, and 500nm.

10.5 National Instruments and LabVIEW

Here in Delft, different hardware modules from NI are present which can be used to control the AFM JPK Nanowizard via its break-out box.

Graphical software programs such as Labview can be used to design a control loop in a visual way that can be configured on an FPGA chip manufactured by the same company. National Instruments manufactures both hardware and software modules which thus gives good cooperation between these.

10.5.1 Hardware

cRIO-9039-Sync [85] is an embedded CompactRIO controller with a real-time processor and reconfigurable FPGA. This makes it possible to write the code within Labview, and write it specifically for the FPGA chip. The control loop will be saved on this chip and can be used for adaptive scanning on the JPK Nanowizard.

Input and Output Modules

The CompactRIO controller contains different slots which can be used to plug in input and output modules to be able to read and write signals real time.

Right now, there is known that the PME faculty can provide analog modules, namely the NI 9215 analog input module, and NI 9263/9264 analog output modules. These will be discussed below.

Input Module NI 9215, datasheet available on: [86]

A snapshot is given below, where the following characteristics are given in the correct order: product name, signal levels, number of channels, sample rate, ability to work simultaneously, resolution and connectivity.

NI 9215	± 10 V	4 Differential	100 kS/s/ch	Yes	16-Bit	Screw-Terminal, Spring-Terminal, BNC
---------	------------	----------------	-------------	-----	--------	--

The sample rate of 100kS/s/ch limits the rate to write signals towards the break-out box. This limits the maximum frequency of the cantilever because aliasing must be prevented. However, since the output is measured from the PI controller, the maximum bandwidth is determined by the combination of the cantilever's frequency, LIA filter, and PI controller. This combination must thus be lower than 50kHz to prevent aliasing. This means that a higher frequency can be chosen for the cantilever because it is already filtered. Moreover, it is beneficial that the input module contains BNC connectors so that there is only a simple BNC cable required to connect it to the break-out box.

Output Module NI 9263/9264, datasheets available on: [87, 88]

Again, there is a snapshot given below with the following characteristics in the correct order: product name, signal levels, number of channels, sample rate, ability to work simultaneously, resolution and connectivity.

NI 9263	Voltage Output	± 10 V	4	100 kS/s/ch	Yes	16-Bit	Screw-Terminal, Spring-Terminal
NI 9264	Voltage Output	± 10 V	16	25 kS/s/ch	Yes	16-Bit	Spring-Terminal, 37-Pin DSUB

The sample rates of 25 and 100kS/s/ch limit the rate to write signals to the break-out box. This limits the bandwidth frequency to a value lower than 12.5kHz or 50kHz to prevent aliasing, which represents the X and Y signals.

The most convenient would be to choose the NI 9263 because it has a much higher sample rate. Furthermore, just two signals should be written toward the break-out box, so one NI 9263 module would be sufficient.

Connecting the hardware

Following the methodology within this report, the minimum requirement to have a working control loop consists of three signals: reading the *vertical deflection*, and writing both *Piezo stage X axis* and *Piezo stage Y axis*. However, being able to collect more data is much more preferred. For instance, reading the Piezo stage X axis and Piezo stage Y axis is useful to analyze lagging/leading signals and possibly define an estimation for the horizontal drift that will be most likely present. Next, reading the cantilever's excitation could be desirable to check whether the input trace does not show any irregularities.

Be aware to use output channels from the break-out box with a lower or same amount of bits with respect to the NI input module, to prevent truncation of the bottom bits of the output signal. For instance, if you feed a 24-bit output signal (from the break-out box) to a 16-bit NI 9215 input module, there will be truncation of the bottom eight bits. These bottom eight bits will then just be ignored. This will increase the amount of distortion, especially for low-level signals. This could give problems because you want to measure the displacement accurately [89]. The other way around will not give any problems. If you feed a 16-bit NI9263/9264 output signal on an 18-bit analog input channel of the break-out box, the bottom two bits will be automatically padded out with zeros. However, it is important to have the same sample rates. The NI9263/9264 have sample rates of 100 and 25kS/s/ch respectively, and the 18-bit analog input channels have a sample rate of 800kHz. These must match the lower sample rate of the NI output module to have a match [90].

When attaching the signals to the breakout box, a 50Ω resistor must be put between the break-out box and the CompactRIO controller. It is recommended to first read the signals on an oscilloscope, to see whether the voltages are not too high for the break-out box or the controller.

10.5.2 Software

The following software packages are at least required to design the code with FPGA, and be able to send real-time signals:

- LabVIEW (32-bit)
- NI CompactRIO driver
- LabVIEW FPGA Module (32-bit)
- LabVIEW Real-Time Module

Furthermore, there might be a compatibility issue between LabVIEW and some NI CompactRIO driver versions, so the following NI support page can help to choose the right combination such that it is compatible: [91].

Next, the Matlab model must be translated into a LabVIEW model. LabVIEW is a graphical programming environment that can be used to both perform simulations and program the CompactRIO such that it controls the AFM. LabVIEW works with Virtual Instruments (VI), which can be seen as a program that is created within its programming environment. It is possible to generate VIs yourself and add different (standardized) VIs to build your code. LabVIEW contains three different levels, of which its communications are visualized in figure 10.1

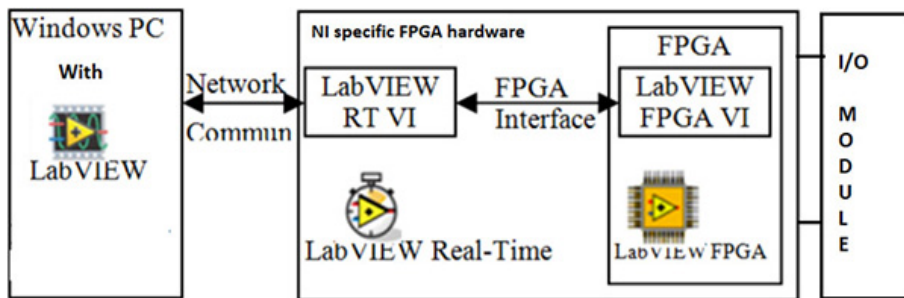


Figure 10.1: An overview of the different levels within LabVIEW [92]

In practice, below 'My Computer' the main Virtual Instrument (VI) can be generated which is stationed on the Windows PC. From here, the programming can be done that processes the general loop such as imaging and theoretical simulations. Within the RT CompactRIO Target, the program must be built that is stationed on the processor itself. This consists of two levels: Real-Time VI (RT VI) and FPGA VI. The RT VI is a connection between the FPGA VI and the main VI, which mostly reads and saves the signals from the FPGA VI and sends these toward the main VI. On the FPGA VI, the control loop must be built which processes the incoming signals towards output signals.

For the practical implementation of the Adaptive Raster Scanning method, it could be useful to code the simulation in LabVIEW as well. A reason could be that comparing the experiments with the simulations will become more objective since the software is the same. Below, coding examples or methodologies are given for the different aspects of programming the cantilever.

Cantilever's Dynamics

The cantilever's dynamics can be modeled in two ways which can be taken from section 6.1. At first, the identification data from the cantilever can be used in the state-space form as shown in equation (8.1). Secondly, it can be modeled as a mass-spring-damper system which is shown in equation (6.2). For this configuration, the cantilever had a resonance frequency of 400kHz. This will become too high to use for the current set of in- and output modules which have a maximum frame rate of 100kS/s/ch. Therefore, a model is built that follows a theoretical approach for the mass-spring-damper system, which is shown in figure 10.2. Of course, there can still be decided to perform identification experiments for new sets of cantilevers to apply a state-space approach.

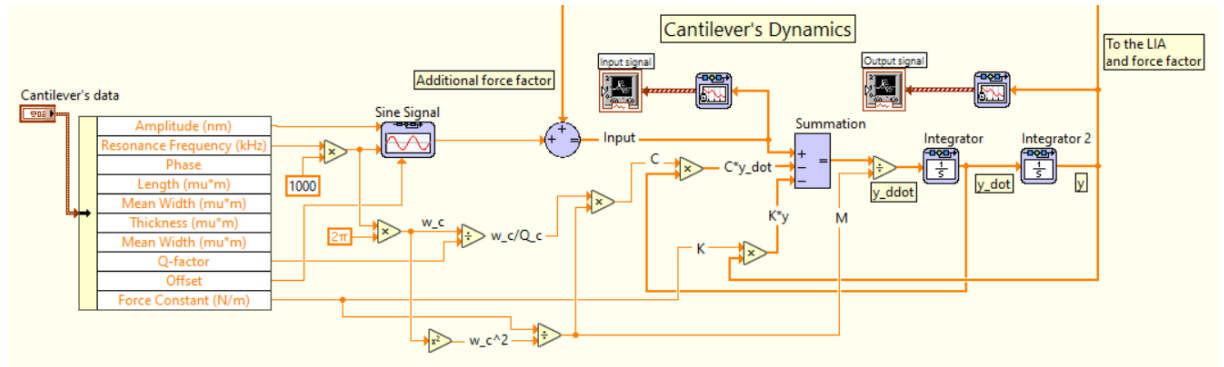


Figure 10.2: The dynamics of the cantilever are coded here via its equation of motion.

Additional force and tip-sample force

The additional force factor can be modeled by using a linear approach which has been explained by Eq. 6.5 in section 6.3 which is visualized in figure 10.3.

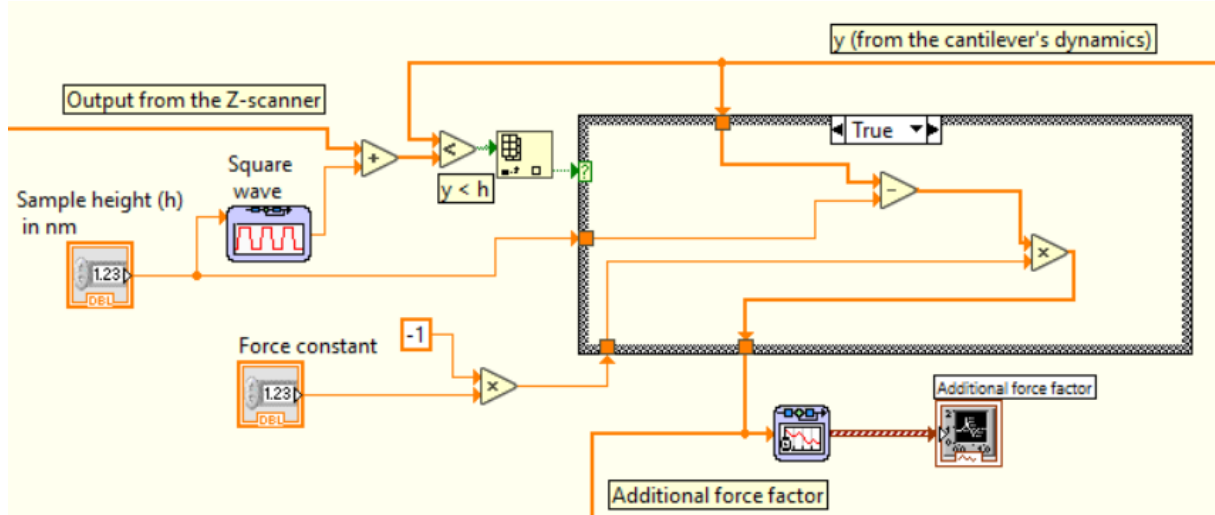


Figure 10.3: The condition for the tip-sample force is coded here. There are two cases, a 'true' case where $y < h$ and thus the linear force will be applied. The 'false' case corresponds with $y \geq h$, where the force output will be set to zero.

Lock-In Amplifier

Coding the LIA follows the same methodology as shown in section 6.5. This means that a reference signal must be defined and split into cosine and sine parts. These signals are then mixed with a preamplified input signal after which they are put into a fourth-order Butterworth low-pass filter. The filter must also take a moving average with a length of one wavelength (25 time steps). This moving average can be generated by adding memory blocks after each other and taking the average. After filtering the signal, the magnitude and phase difference can be determined. The magnitude of the LIA will then be used as input to the controller.

Z-scanner

Again as for the cantilever's dynamics, the z-scanner can be modeled as a mass-spring-damper system as shown in Eq. 6.6 from section 6.4. Figure 10.4 shows the code that corresponds to the z-scanner.

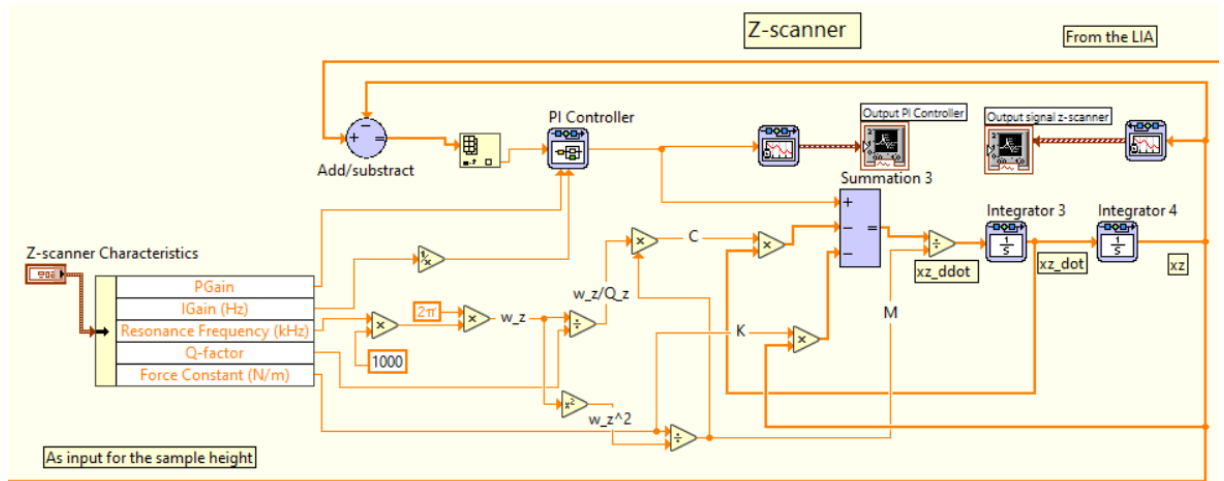


Figure 10.4: The dynamics of the z-scanner are coded here via its equation of motion.

Chapter 11

Conclusions

The simulation results for the proof-of-concept of the Adaptive Raster Scanning show that there is a large potential to be improved considering the current Conventional Raster Scanning method. Analyzing the general performance curves in section 8.4, there can be concluded that its general performance is better for all three different values of d_{adap} that have been taken into account for this report. For the best performing parameter at $d_{adap}=1\text{nm}$, the Adaptive Raster Scanning Method is an improvement of up to 9.5 times considering the spatial resolution, and 9.4 times in time efficiency.

Moreover, figures 8.4 and 8.7 show that the effect of parachuting has decreased severely while enhancing the same scanning time. There can thus be said that the proof-of-concept on implementing a variable scan speed decreases the effect of parachuting and thereby improves the spatial resolution up to a factor of 9.5.

Increasing the scanning speed, there is a limit that is set towards a vertical asymptote. This is caused by an increasing error for the settling time at the start of a line scan, combined with the decrease of t_{up} and t_{par} that makes the controller more sensitive for a large offset of the time delay.

For the different values of d_{adap} that have been analyzed, namely 1, 2, and 4nm, there can be concluded that there is a trade-off between robustness and efficiency. Lowering d_{adap} will make the controller more efficient, but more sensitive to an inaccurate estimation of the time delay. Getting too low will cause oscillating results for the performance curve at higher speeds. The most robust parameter at $d_{adap}=4\text{nm}$ still shows an improvement with a factor of 4.4 considering the spatial resolution and 4.3 in time efficiency.

Considering the detection algorithm, there can be concluded that it has high repeatability. It has a repeatability of 97.1% for the uphill events, and 93.6% for the parachuting events. Furthermore, it has mediocre accuracy with an uncertainty of approximately one period. However, this can be improved by implementing the raw deflection signal for the detection algorithm.

Next, there can be concluded that the proof-of-concept is versatile since it is applicable to different shapes, here to a circle. The spatial resolution showed an increase by a factor of 7.8, and the scanning time decreased by a factor of 8.9

The Adaptive Raster Scanning Method works currently for two events of either an uphill and/or parachuting event. This can be improved by implementing a different method to detect the maxima from the mixed signal that multiplies the first and second derivatives. A detection algorithm based on the RMS value could improve the method a lot because more events can be measured and the lateral resolution might decrease. There could be investigated in defining the magnitude based on the average RMS value, sample height, scanning speed, and sample time. This proof-of-concept can be further improved by identifying whether there is indeed an optimum for the scanning speed with the current parameters, which seems to be in a range of 160-170 $\mu\text{m/s}$ for these parameters. This can be done by taking more measurements for different values of d_{adap} . The next step would be to test this proof-of-concept experimentally. Section 10 shows the first steps to design such a controller for a real-life setup. When performing experiments, it is important to incorporate the effects of horizontal drift and the computing time between the forward and backward lines.

Finally, since this Adaptive Raster Scanning method solely focuses on externally tuning the X and Y piezo actuators, there is room for combining this method with techniques that are focused on the Z or Cantilever's piezo actuator.

Bibliography

- [1] G. Binnig, C. F. Quate, and C. Gerber, “Atomic Force Microscope,” *Physical Review Letters*, vol. 56, no. 9, 3 1986.
- [2] T. Uchihashi, N. Kodera, and T. Ando, “Guide to video recording of structure dynamics and dynamic processes of proteins by high-speed atomic force microscopy,” *Nature Protocols*, vol. 7, no. 6, pp. 1193–1206, 6 2012.
- [3] Y. F. Dufrêne, T. Ando, R. Garcia, D. Alsteens, D. Martinez-Martin, A. Engel, C. Gerber, and D. J. Müller, “Imaging modes of atomic force microscopy for application in molecular and cell biology,” *Nature Nanotechnology*, vol. 12, no. 4, pp. 295–307, 4 2017.
- [4] R. C. Barrett, “High-speed, large-scale imaging with the atomic force microscope,” *Journal of Vacuum Science & Technology B: Microelectronics and Nanometer Structures*, vol. 9, no. 2, pp. 302–306, 3 1991.
- [5] T. Ando, “High-speed atomic force microscopy coming of age,” *Nanotechnology*, vol. 23, no. 6, pp. 1–27, 2 2012.
- [6] T. Sulchek, S. C. Minne, J. D. Adams, D. A. Fletcher, A. Atalar, C. F. Quate, and D. M. Adderton, “Dual integrated actuators for extended range high speed atomic force microscopy,” *Applied Physics Letters*, vol. 75, no. 11, pp. 1637–1639, 9 1999.
- [7] T. Sulchek, R. J. Grow, G. G. Yaralioglu, S. C. Minne, C. F. Quate, S. R. Manalis, A. Kiraz, A. Aydine, and A. Atalar, “Parallel atomic force microscopy with optical interferometric detection,” *Applied Physics Letters*, vol. 78, no. 12, pp. 1787–1789, 3 2001.
- [8] S. C. Minne, G. Yaralioglu, S. R. Manalis, J. D. Adams, J. Zesch, A. Atalar, and C. F. Quate, “Automated parallel high-speed atomic force microscopy,” *Applied Physics Letters*, vol. 72, no. 18, pp. 2340–2342, 5 1998.
- [9] S. C. Minne, J. D. Adams, G. Yaralioglu, S. R. Manalis, A. Atalar, and C. F. Quate, “Centimeter scale atomic force microscope imaging and lithography,” *Applied Physics Letters*, vol. 73, no. 12, pp. 1742–1744, 9 1998.
- [10] D. A. Walters, J. P. Cleveland, N. H. Thomson, P. K. Hansma, M. A. Wendman, G. Gurlley, and V. Elings, “Short cantilevers for atomic force microscopy,” *Review of Scientific Instruments*, vol. 67, no. 10, pp. 3583–3590, 10 1996.
- [11] T. E. Schäffer, J. P. Cleveland, F. Ohnesorge, D. A. Walters, and P. K. Hansma, “Studies of vibrating atomic force microscope cantilevers in liquid,” *Journal of Applied Physics*, vol. 80, no. 7, pp. 3622–3627, 10 1996.
- [12] M. B. Viani, T. E. Schäffer, A. Chand, M. Rief, H. E. Gaub, and P. K. Hansma, “Small cantilevers for force spectroscopy of single molecules,” *Journal of Applied Physics*, vol. 86, no. 4, pp. 2258–2262, 8 1999.
- [13] M. B. Viani, T. E. Schäffer, G. T. Palocz, L. I. Pietrasanta, B. L. Smith, J. B. Thompson, M. Richter, M. Rief, H. E. Gaub, K. W. Plaxco, A. N. Cleland, H. G. Hansma, and P. K. Hansma, “Fast imaging and fast force spectroscopy of single biopolymers with a new atomic force microscope designed for small cantilevers,” *Review of Scientific Instruments*, vol. 70, no. 11, pp. 4300–4303, 11 1999.
- [14] T. Ando, N. Kodera, E. Takai, D. Maruyama, K. Saito, and A. Toda, “A high-speed atomic force microscope for studying biological macromolecules,” *Proceedings of the National Academy of Sciences*, vol. 98, no. 22, pp. 12 468–12 472, 10 2001.

- [15] T. Ando, N. Kodera, D. Maruyama, E. Takai, K. Saito, and A. Toda, “A High-Speed Atomic Force Microscope for Studying Biological Macromolecules in Action,” *Japanese Journal of Applied Physics*, vol. 41, no. Part 1, No. 7B, pp. 4851–4856, 7 2002.
- [16] V. G. Gisbert, S. Benaglia, M. R. Uhlig, R. Proksch, and R. Garcia, “High-Speed Nanomechanical Mapping of the Early Stages of Collagen Growth by Bimodal Force Microscopy,” *ACS Nano*, vol. 15, no. 1, pp. 1850–1857, 1 2021.
- [17] T. Ando, “High-speed atomic force microscopy,” *Current Opinion in Chemical Biology*, vol. 51, pp. 105–112, 8 2019.
- [18] N. Kodera, D. Noshiro, S. K. Dora, T. Mori, J. Habchi, D. Blocquel, A. Gruet, M. Dosnon, E. Salladini, C. Bignon, Y. Fujioka, T. Oda, N. N. Noda, M. Sato, M. Lotti, M. Mizuguchi, S. Longhi, and T. Ando, “Structural and dynamics analysis of intrinsically disordered proteins by high-speed atomic force microscopy,” *Nature Nanotechnology*, vol. 16, no. 2, pp. 181–189, 2 2021.
- [19] T. Ando, T. Uchihashi, and N. Kodera, “High-Speed AFM and Applications to Biomolecular Systems,” *Annual Review of Biophysics*, vol. 42, no. 1, pp. 393–414, 5 2013.
- [20] T. Sulchek, G. G. Yaralioglu, C. F. Quate, and S. C. Minne, “Characterization and optimization of scan speed for tapping-mode atomic force microscopy,” *Review of Scientific Instruments*, vol. 73, no. 8, pp. 2928–2936, 8 2002.
- [21] S. Belikov, J. Alexander, M. Surtchev, and S. Magonov, “Implementation of atomic force microscopy resonance modes based on asymptotic dynamics using Costas Loop,” in *2016 American Control Conference (ACC)*. IEEE, 7 2016, pp. 6201–6208.
- [22] D. Y. Abramovitch, S. B. Andersson, L. Y. Pao, and G. Schitter, “A Tutorial on the Mechanisms, Dynamics, and Control of Atomic Force Microscopes,” in *2007 American Control Conference*. IEEE, 7 2007, pp. 3488–3502.
- [23] T. Ando, T. Uchihashi, and T. Fukuma, “High-speed atomic force microscopy for nano-visualization of dynamic biomolecular processes,” *Progress in Surface Science*, vol. 83, no. 7-9, pp. 337–437, 11 2008.
- [24] B. Lee, S. Somnath, and W. P. King, “Fast nanotopography imaging using a high speed cantilever with integrated heater–thermometer,” *Nanotechnology*, vol. 24, no. 13, pp. 135 501(1)–135 501(10), 4 2013.
- [25] Y. Gan, “Atomic and subnanometer resolution in ambient conditions by atomic force microscopy,” *Surface Science Reports*, vol. 64, no. 3, pp. 100–121, 3 2009.
- [26] N. Kodera, M. Sakashita, and T. Ando, “Dynamic proportional-integral-differential controller for high-speed atomic force microscopy,” *Review of Scientific Instruments*, vol. 77, no. 8, pp. 083 704(1)–083 704(7), 8 2006.
- [27] A. B. Churnside and T. T. Perkins, “Ultrastable atomic force microscopy: Improved force and positional stability,” *FEBS Letters*, vol. 588, no. 19, pp. 3621–3630, 10 2014.
- [28] J. Mou, D. M. Czajkowsky, Y. Zhang, and Z. Shao, “High-resolution atomic-force microscopy of DNA: the pitch of the double helix,” *FEBS Letters*, vol. 371, no. 3, pp. 279–282, 9 1995.
- [29] S. J. T. van Noort, K. O. van der Werf, B. G. de Groot, and J. Greve, “High Speed Atomic Force Microscopy of Biomolecules by Image Tracking,” *Biophysical Journal*, vol. 77, no. 4, pp. 2295–2303, 10 1999.

- [30] B. Hartman and S. B. Andersson, “Feature tracking for high speed AFM: Experimental demonstration,” in *2017 American Control Conference (ACC)*. IEEE, 5 2017, pp. 773–778.
- [31] M. D’Acunto and O. Salvetti, “Pattern recognition methods for thermal drift correction in Atomic Force Microscopy imaging,” *Pattern Recognition and Image Analysis*, vol. 21, no. 1, pp. 9–19, 3 2011.
- [32] Khafa F, Patnaik S, and Tavana M, “Advances in Intelligent Systems and Interactive Applications: Proceedings of the 4th International Conference on Intelligent, Interactive Systems and Applications (IISA2019).” Springer Nature, 2019, vol. 1084, pp. 270–275.
- [33] S. Bashash, “Modeling and control of piezoactive micro and nano systems,” Ph.D. dissertation, Clemson University, 12 2008.
- [34] Y. Wu, Y. Fang, and X. Ren, “A high-efficiency Kalman filtering imaging mode for an atomic force microscopy with hysteresis modeling and compensation,” *Mechatronics*, vol. 50, pp. 69–77, 4 2018.
- [35] D. Croft, G. Shed, and S. Devasia, “Creep, Hysteresis, and Vibration Compensation for Piezoactuators: Atomic Force Microscopy Application,” *Journal of Dynamic Systems, Measurement, and Control*, vol. 123, no. 1, pp. 35–43, 3 2001.
- [36] W. Rongxiu, J. Chaoyuan, C. Yao, H. Weijun, and W. Bo, “Research on Hysteresis Modeling for Piezoelectric Displacement Actuators,” 2017, pp. 22–28.
- [37] Y. Wang, S. Wu, L. Xu, and Y. Zeng, “A new precise positioning method for piezoelectric scanner of AFM,” *Ultramicroscopy*, vol. 196, pp. 67–73, 1 2019.
- [38] B. Derjaguin, V. Muller, and Y. Toporov, “Effect of contact deformations on the adhesion of particles,” *Journal of Colloid and Interface Science*, vol. 53, no. 2, pp. 314–326, 11 1975.
- [39] A. Yurtsever, “Nanotribological surface characterization by frequency modulated torsional resonance mode AFM,” Ph.D. dissertation, Ludwig Maximilians Universität München, 7 2008.
- [40] O. Pfeiffer, R. Bennewitz, A. Baratoff, E. Meyer, and P. Grütter, “Lateral-force measurements in dynamic force microscopy,” *Physical Review B*, vol. 65, no. 16, pp. 161 403(1)–161 403(4), 4 2002.
- [41] H. Hölscher, “Theory of phase-modulation atomic force microscopy with constant-oscillation amplitude,” *Journal of Applied Physics*, vol. 103, no. 6, pp. 064 317(1)–064 317(6), 3 2008.
- [42] D. Sarid, “Review of scanning force microscopy,” *Journal of Vacuum Science & Technology B: Microelectronics and Nanometer Structures*, vol. 9, no. 2, pp. 431–437, 3 1991.
- [43] R. Nishi, I. Houda, T. Aramata, Y. Sugawara, and S. Morita, “Phase change detection of attractive force gradient by using a quartz resonator in noncontact atomic force microscopy,” *Applied Surface Science*, vol. 157, no. 4, pp. 332–336, 4 2000.
- [44] R. García, “Dynamic atomic force microscopy methods,” *Surface Science Reports*, vol. 47, no. 6-8, 9 2002.
- [45] G. E. Fantner, G. Schitter, J. H. Kindt, T. Ivanov, K. Ivanova, R. Patel, N. Holten-Andersen, J. Adams, P. J. Thurner, I. W. Rangelow, and P. K. Hansma, “Components for high speed atomic force microscopy,” *Ultramicroscopy*, vol. 106, no. 8-9, 6 2006.

- [46] C. Bustamante, C. Rivetti, and D. J. Keller, “Scanning force microscopy under aqueous solutions,” *Current Opinion in Structural Biology*, vol. 7, no. 5, pp. 709–716, 10 1997.
- [47] A. Farokh Payam, P. Biglarbeigi, A. Morelli, P. Lemoine, J. McLaughlin, and D. Finlay, “Data acquisition and imaging using wavelet transform: a new path for high speed transient force microscopy,” *Nanoscale Advances*, vol. 3, no. 2, pp. 383–398, 2021.
- [48] R. Garcia and E. T. Herruzo, “The emergence of multifrequency force microscopy,” *Nature Nanotechnology*, vol. 7, no. 4, pp. 217–226, 4 2012.
- [49] G. R. Heath and S. Scheuring, “Advances in high-speed atomic force microscopy (HS-AFM) reveal dynamics of transmembrane channels and transporters,” *Current Opinion in Structural Biology*, vol. 57, pp. 93–102, 8 2019.
- [50] G. Schitter, R. Stark, and A. Stemmer, “Fast contact-mode atomic force microscopy on biological specimen by model-based control,” *Ultramicroscopy*, vol. 100, no. 3-4, pp. 253–257, 8 2004.
- [51] G. Schitter, F. Allgöwer, and A. Stemmer, “A new control strategy for high-speed atomic force microscopy,” *Nanotechnology*, vol. 15, no. 1, 1 2004.
- [52] M. Dukic, V. Todorov, S. Andany, A. P. Nievergelt, C. Yang, N. Hosseini, and G. E. Fantner, “Digitally controlled analog proportional-integral-derivative (PID) controller for high-speed scanning probe microscopy,” *Review of Scientific Instruments*, vol. 88, no. 12, pp. 123 712(1)–123 712(7), 12 2017.
- [53] Stanford Research Systems, “SIM960 Analog PID Controller.” [Online]. Available: <https://www.thinksrs.com/products/SIM960.htm>
- [54] T. Sulchek, R. Hsieh, J. D. Adams, G. G. Yaralioglu, S. C. Minne, C. F. Quate, J. P. Cleveland, A. Atalar, and D. M. Adderton, “High-speed tapping mode imaging with active Q control for atomic force microscopy,” *Applied Physics Letters*, vol. 76, no. 11, pp. 1473–1475, 3 2000.
- [55] T. R. Rodriguez and R. Garcia, “Theory of Q control in atomic force microscopy,” *Applied Physics Letters*, vol. 82, no. 26, pp. 4821–4823, 6 2003.
- [56] M. B. Coskun, H. Alemansour, A. G. Fowler, M. Maroufi, and S. O. R. Moheimani, “Q Control of an Active AFM Cantilever With Differential Sensing Configuration,” *IEEE Transactions on Control Systems Technology*, vol. 27, no. 5, 9 2019.
- [57] O. Kaveh, M. B. Coskun, M. Mahdavi, and S. O. Reza Moheimani, “FPGA-Based Characterization and Q-Control of an Active AFM Cantilever,” in *2020 IEEE/ASME International Conference on Advanced Intelligent Mechatronics (AIM)*. IEEE, 7 2020, pp. 2062–2067.
- [58] T. Uchihashi, N. Kodera, H. Itoh, H. Yamashita, and T. Ando, “Feed-Forward Compensation for High-Speed Atomic Force Microscopy Imaging of Biomolecules,” *Japanese Journal of Applied Physics*, vol. 45, no. 3B, pp. 1904–1908, 3 2006.
- [59] H. Watanabe, T. Uchihashi, T. Kobashi, M. Shibata, J. Nishiyama, R. Yasuda, and T. Ando, “Wide-area scanner for high-speed atomic force microscopy,” *Review of Scientific Instruments*, vol. 84, no. 5, pp. 053 702(1)–053 702(10), 5 2013.
- [60] J. Preiner, J. Tang, V. Pastushenko, and P. Hinterdorfer, “Higher Harmonic Atomic Force Microscopy: Imaging of Biological Membranes in Liquid,” *Physical Review Letters*, vol. 99, no. 4, pp. 046 102(1)–046 102(4), 7 2007.

- [61] A. Raman, S. Trigueros, A. Cartagena, A. P. Z. Stevenson, M. Susilo, E. Nauman, and S. A. Contera, “Mapping nanomechanical properties of live cells using multi-harmonic atomic force microscopy,” *Nature Nanotechnology*, vol. 6, no. 12, pp. 809–814, 12 2011.
- [62] I. A. Mahmood, S. O. R. Moheimani, and B. Bhikkaji, “A New Scanning Method for Fast Atomic Force Microscopy,” *IEEE Transactions on Nanotechnology*, vol. 10, no. 2, pp. 203–216, 3 2009.
- [63] M. S. Rana, H. R. Pota, and I. R. Petersen, “Performance of Sinusoidal Scanning With MPC in AFM Imaging,” *IEEE/ASME Transactions on Mechatronics*, vol. 20, no. 1, pp. 73–83, 2 2015.
- [64] J. L. Worthey and S. B. Andersson, “Local circular scanning for autonomous feature tracking in AFM,” in *2015 American Control Conference (ACC)*. IEEE, 7 2015, pp. 3490–3495.
- [65] G. R. Heath, E. Kots, J. L. Robertson, S. Lansky, G. Khelashvili, H. Weinstein, and S. Scheuring, “Localization atomic force microscopy,” *Nature*, vol. 594, no. 7863, pp. 385–390, 6 2021.
- [66] Bruker and JPK, “NanoWizard 4 XP NanoScience.” [Online]. Available: https://www.bruker.com/en/products-and-solutions/microscopes/materials-afm/jpk-nanowizard-4-xp-nanoscience.html#ID_specifications
- [67] M. V. Salapaka, H. S. Bergh, J. Lai, A. Majumdar, and E. McFarland, “Multi-mode noise analysis of cantilevers for scanning probe microscopy,” *Journal of Applied Physics*, vol. 81, no. 6, pp. 2480–2487, 3 1997.
- [68] R. García and A. San Paulo, “Attractive and repulsive tip-sample interaction regimes in tapping-mode atomic force microscopy,” *Physical Review B*, vol. 60, no. 7, pp. 4961–4967, 8 1999.
- [69] S. Paulo and R. García, “Tip-surface forces, amplitude, and energy dissipation in amplitude-modulation (tapping mode) force microscopy,” *Physical Review B*, vol. 64, no. 19, pp. 193 411(1)–193 411(4), 10 2001.
- [70] N. Kodera, H. Yamashita, and T. Ando, “Active damping of the scanner for high-speed atomic force microscopy,” *Review of Scientific Instruments*, vol. 76, no. 5, 5 2005.
- [71] S. DeVore, A. Gauthier, J. Levy, and C. Singh, “Development and evaluation of a tutorial to improve students’ understanding of a lock-in amplifier,” *Physical Review Physics Education Research*, vol. 12, no. 2, p. 020127, 9 2016.
- [72] M. G. Ruppert, D. M. Harcombe, M. R. P. Ragazzon, S. O. R. Moheimani, and A. J. Fleming, “A review of demodulation techniques for amplitude-modulation atomic force microscopy,” *Beilstein Journal of Nanotechnology*, vol. 8, pp. 1407–1426, 7 2017.
- [73] K. Manal and W. Rose, “A general solution for the time delay introduced by a low-pass Butterworth digital filter: An application to musculoskeletal modeling,” *Journal of Biomechanics*, vol. 40, no. 3, pp. 678–681, 1 2007.
- [74] JPK Instruments, “NanoWizard Series User Manual,” in *SPM Software Release*, 6th ed., 1 2018, pp. 1–187.
- [75] S. K. Das, H. R. Pota, and I. R. Petersen, “Damping Controller Design for Nanopositioners: A Mixed Passivity, Negative-Imaginary, and Small-Gain Approach,” *IEEE/ASME Transactions on Mechatronics*, vol. 20, no. 1, pp. 416–426, 2 2015.

- [76] R. M. Schmidt, G. Schitter, and A. Rankers, *The design of high performance mechatronics: high-Tech functionality by multidisciplinary system integration*. Ios Press, 2020.
- [77] Electrical4U, “Time Response of Second Order Control System (Worked Example),” 9 2021. [Online]. Available: <https://www.electrical4u.com/time-response-of-second-order-control-system/>
- [78] M. Verhaegen and V. Verdult, *Filtering and System Identification : A Least Squares Approach*. Cambridge: Cambridge University Press, 2007. [Online]. Available: <https://search.ebscohost.com/login.aspx?direct=true&db=nlebk&AN=194302&site=ehost-live>
- [79] tutorialspoint, “Time Domain Specifications.” [Online]. Available: https://www.tutorialspoint.com/control_systems/control_systems_time_domain_specifications.htm#:~:text=ratio%20%CE%B4%20increases.-,Settling%20time,is%20denoted%20by%20ts.
- [80] Y. Wang, H. Wang, and S. Bi, “Real time drift measurement for colloidal probe atomic force microscope: a visual sensing approach,” *AIP Advances*, vol. 4, no. 5, pp. 057 130–1, 5 2014.
- [81] B. Mokaberi and A. Requicha, “Drift compensation for automatic nanomanipulation with scanning probe microscopes,” *IEEE Transactions on Automation Science and Engineering*, vol. 3, no. 3, pp. 199–207, 7 2006.
- [82] Bruker, “Vortis Combi Controller.” [Online]. Available: <https://www.bruker.com/en/products-and-solutions/microscopes/bioafm/bioafm-accessories/vortis-combi-controller.html>
- [83] arm, “What is FPGA.” [Online]. Available: <https://www.arm.com/glossary/fpga>
- [84] Micro to Nano, “AFM / SPM Calibration Standards and Test Gratings.” [Online]. Available: <https://www.microtonano.com/AFM-XYZ-calibration-standard-for-calibrated-measurements-and-dimensions.php>
- [85] NI, “cRIO-9039 CompactRIO Controller.” [Online]. Available: <https://www.ni.com/nl-nl/support/model.crio-9039.html>
- [86] —, “NI9215 Datasheet.” [Online]. Available: <https://www.amc-systeme.de/files/pdf/ni-9215-amc.pdf>
- [87] —, “NI9263 Datasheet.” [Online]. Available: <https://www.amc-systeme.de/files/pdf/ni-9263-amc.pdf>
- [88] —, “NI9264 Datsheet.” [Online]. Available: <https://www.amc-systeme.de/files/pdf/ni-9264-amc.pdf>
- [89] H. Robjohns and T. Flint, “Q. Can I feed a 24-bit signal into a 16-bit device?” 2 2005. [Online]. Available: <https://www.soundonsound.com/sound-advice/q-can-feed-24-bit-signal-16-bit-device>
- [90] H. Robjohns, “Q. Can I feed 16-bit digital audio into a 24-bit digital device via S/PDIF?” 10 2015. [Online]. Available: <https://www.soundonsound.com/sound-advice/q-can-feed-16-bit-digital-audio-24-bit-digital-device-spdif>
- [91] NI, “CompactRIO Device Driver and LabVIEW Version Compatibility.” [Online]. Available: <https://www.ni.com/nl-nl/support/documentation/compatibility/20/compactrio-device-driver-and-labview-version-compatibility-.html>

- [92] Farnell, “How to use LabVIEW for FPGA Based Application.” [Online]. Available: <https://nl.farnell.com/how-to-use-labview-for-fpga-based-application>

Appendix A

Extra formulas from literature

Some extra formulas from literature are put into this chapter to give extra insight into how the different theory is grounded.

A.1 Noise in the optical system

e_{nor} : This error is caused by laser intensity fluctuations. It can be detected by adding the left upper and lower corner of the photodiode, A and D, and subtracting the sum of the right upper and lower corner, B and C. Next, this error can be eliminated by normalizing this error, which means dividing through the total sum:

$$e_{nor} = \frac{(A + D) - (B + C)}{A + B + C + D} \quad (\text{A.1})$$

f_{nor} : The friction signal as a result of the first torsional mode, which is in the vertical direction on the photodiode. Detecting and normalizing the friction signal in the same manner as for the error value, the following equation can be settled [22].

$$f_{nor} = \frac{(A + B) - (C + D)}{A + B + C + D} \quad (\text{A.2})$$

A.2 Nonlinear force equation

For the vertical tip-sample interaction force of a spherical tip on a flat surface, the following equation can be given which corresponds to its nonlinear behavior [22]

$$F(r) = k \left[- \left(\frac{\sigma}{r} \right)^2 + \frac{1}{30} \left(\frac{\sigma}{r} \right)^8 \right] \quad (\text{A.3})$$

where σ is the interaction parameter, r is the tip-sample distance, and k is a constant depending on the geometry and material of the tip and sample.

Appendix B

Examples of experimental research in practice

The images that have been used are from experiments done after January 2019. There is only focused on what can be observed from the image itself which would require no background information from the text.

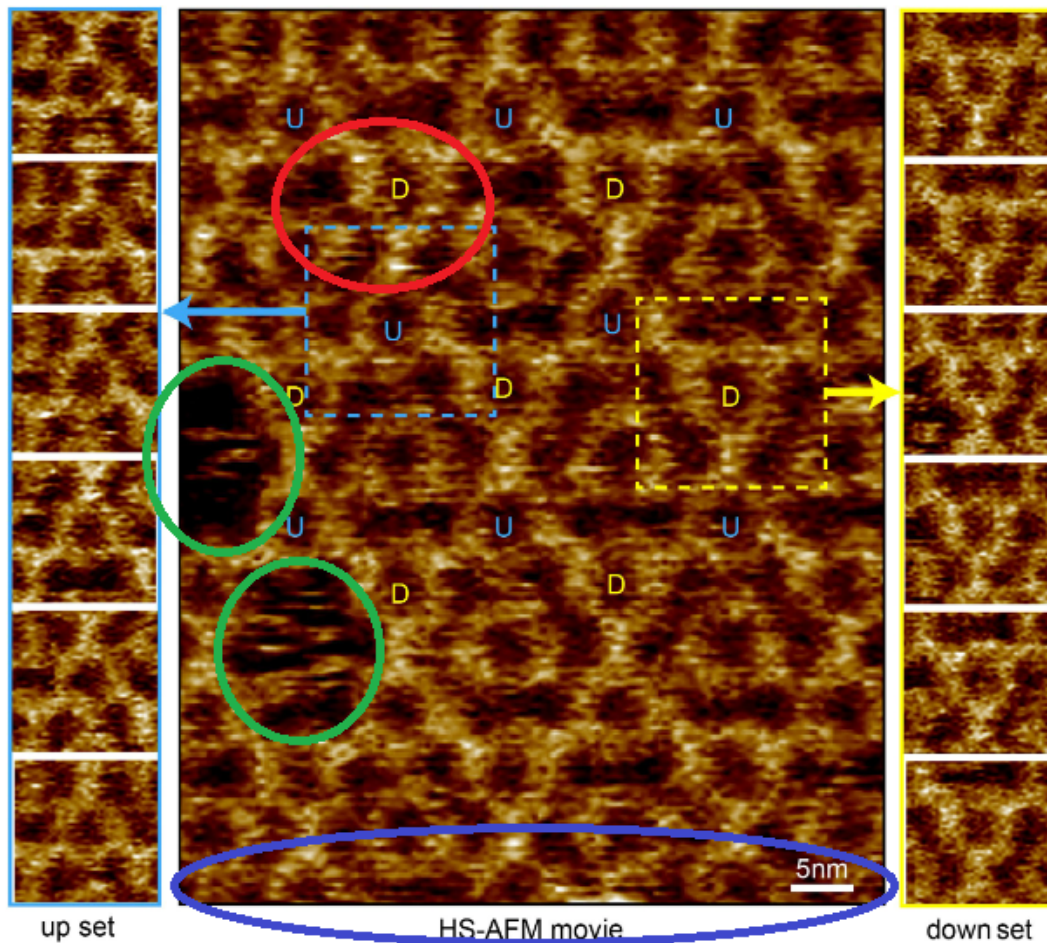


Figure B.1: (2021) Picture from a HS-AFM movie by Heath et. al [65]. Here, there can be observed that the scan has been done from the left to the right side as there are many light stripes pointing toward the right side of the picture. An example is red circled and it shows the presence of parachuting which is quite dominating the quality of the image. At the bottom of the image within the blue image, the spatial resolution seems to be skewed could be a result of hysteresis and thermal drift. Furthermore, the green circles show some unusual missing topography. This could be that topography is really missing, or some trouble in the demodulation technique and/or post-processing localization algorithm as in both circles some topography lines are present.

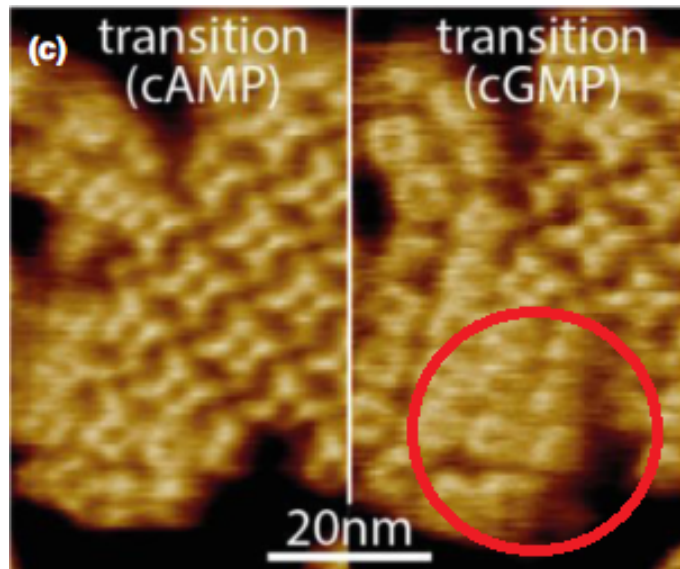


Figure B.2: (2019) Closeup of a measurement sample by Heath. et al [49]. In the right image, some lateral shifts to the left are present for the vertical (or slow scan) axis which is a result of drift. Parachuting is way more present in this image. The red circle within this image shows where it becomes very vague due to parachuting.

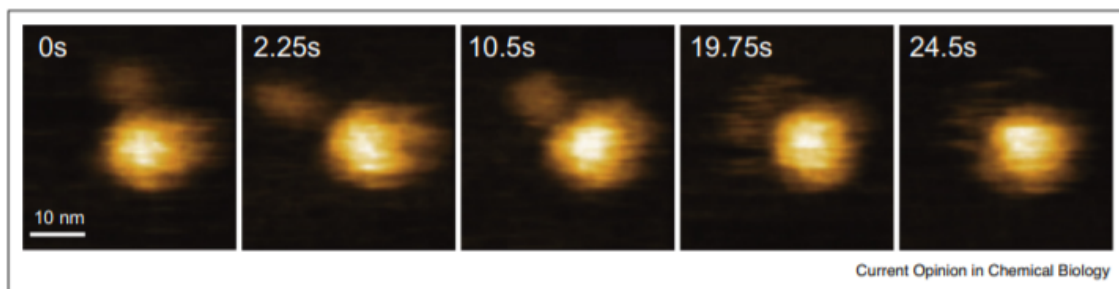


Figure B.3: (2019) measurements over time from the unfolding of the peptidoglycan binding domain of MotS by Ando [17]. In the first three pictures, parachuting can be seen very clearly. For the fourth and fifth pictures, it looks like the yellow dot moves towards the right as parachuting is less present. Furthermore, there are some skewed lateral stripes along the vertical axis which could be affected by drift or 'leftovers' from the unfolding of the layer binding.

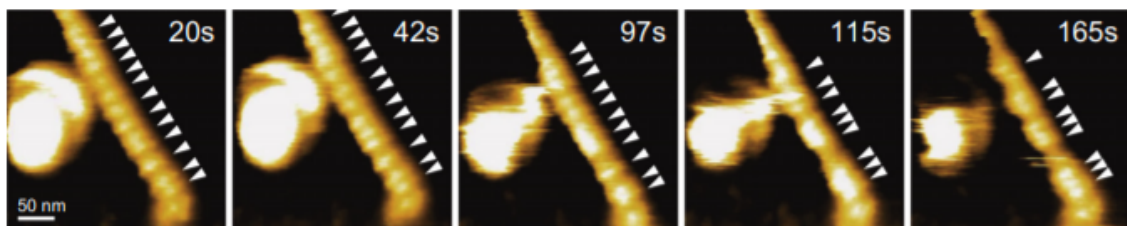


Figure B.4: (2019) measurements over time showing clustering of tube-surrounding dynamin helices by Ando [17]. At every time interval, parachuting is dominating the quality of the image. There are some horizontal white lines present as well, which is probably caused by thermal drift as these effects happen after quite some time.

Appendix C

System Identification

A more detailed version of the cantilever's state-space model using `format long` in Matlab:

$$\begin{aligned}x(k+1) &= Ax(k) + B\bar{u}(k) = \begin{bmatrix} 0.790759313084324 & 0.383036402188894 \\ -0.227722944697784 & 0.905868830507423 \end{bmatrix} x + \dots \\ &\quad \begin{bmatrix} 1.224875022208722 \\ 0.214194045245088 \end{bmatrix} (u_c(k) + F_{ts}(k) + \eta(k)) \quad (\text{C.1}) \\ y(k) &= Cx(k) = \begin{bmatrix} 0.033845312020526 \\ -0.010497580484316 \end{bmatrix} x\end{aligned}$$

Appendix D

Impulse Response PI controller

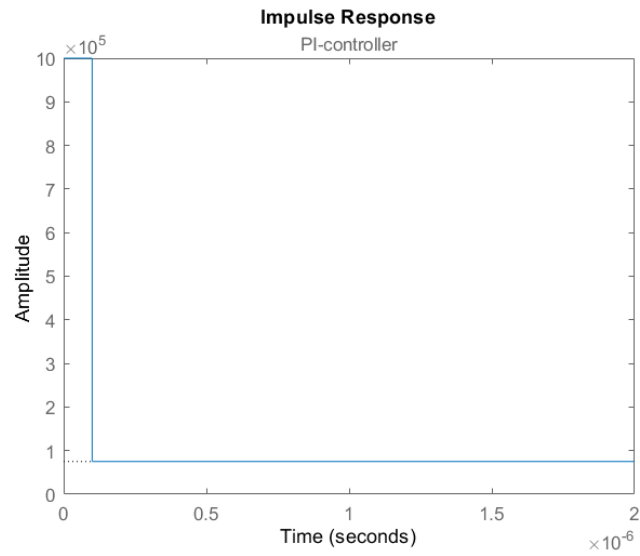


Figure D.1: The impulse response for the PI controller which is done by Matlab. There can be read that the time delay of the controller is $1e^{-5}$ seconds.

Appendix E

Data points and calculation Ratios

Table E.1 and E.2 show the data points that are chosen on figure 8.5 for the analysis done in table 8.1.

Time and error points chosen on the Adaptive Scanning curves			
d_{adap} (nm)	Scan speed ($\mu m/s$)	Time point (s)	Error (nm^2)
1	170	0.00966	0.01132
2	160	0.01376	0.01128
4	160	0.02126	0.01163

Table E.1

Time and error points chosen on the Conventional Scanning curve		
Scan speed ($\mu m/s$)	Time point (s)	Error (nm^2)
11	0.09091	0.01206
50	0.02000	0.05156
70	0.01429	0.07509
100	0.01000	0.10786

Table E.2

The calculation for the resolution ratio where the scanning time has been chosen the same:

$$\begin{aligned}
 d_{adap} &= 1nm : 0.00966s \approx 0.01000s \text{ at Conventional } V = 100\mu m/s \\
 \text{Resolution ratio at 1 nm: } &\frac{0.10786}{0.01132} = 9.52827 \approx 9.5 \\
 d_{adap} &= 2nm : 0.01376s \approx 0.01429s \text{ at Conventional } V = 70\mu m/s \\
 \text{Resolution ratio at 2 nm: } &\frac{0.07509}{0.01128} = 6.65691 \approx 6.7 \\
 d_{adap} &= 4nm : 0.02126s \approx 0.02000s \text{ at Conventional } V = 50\mu m/s \\
 \text{Resolution ratio at 4 nm: } &\frac{0.05165}{0.01163} = 4.44110 \approx 4.4
 \end{aligned} \tag{E.1}$$

The calculation for the scanning time ratio where the resolution has been chosen is the same as for the conventional scan speed, which is at $\approx 11 \mu m/s$ with an error of $0.01206 nm^2$:

$$\begin{aligned}
 \text{Scanning time ratio at 1 nm: } &\frac{0.09091}{0.00966} = 9.41097 \approx 9.4 \\
 \text{Scanning time ratio at 2 nm: } &\frac{0.09091}{0.01376} = 6.60683 \approx 6.6 \\
 \text{Scanning time ratio at 2 nm: } &\frac{0.09091}{0.02126} = 4.27611 \approx 4.3
 \end{aligned} \tag{E.2}$$

Appendix F

Repeatability table

Repeatability Analysis 10-250 $\mu m/s$			Repeatability Analysis 260-500 $\mu m/s$		
Scan Speed ($\mu m/s$)	Uphill	Parachuting	Scan Speed ($\mu m/s$)	Uphill	Parachuting
10	100%	100%	260	100%	100%
20	100%	100%	270	53%	99%
30	100%	100%	280	93%	90%
40	100%	53%	290	67%	100%
50	100%	100%	300	100%	100%
60	100%	100%	310	100%	100%
70	100%	100%	320	100%	100%
80	100%	100%	330	100%	100%
90	100%	100%	340	100%	99%
100	100%	100%	350	100%	100%
110	100%	53%	360	100%	100%
120	100%	50%	370	97%	98%
130	100%	100%	380	100%	100%
140	100%	100%	390	100%	100%
150	100%	100%	400	100%	100%
160	100%	100%	410	100%	100%
170	100%	100%	420	100%	100%
180	100%	100%	430	97%	99%
190	100%	100%	440	100%	100%
200	100%	63%	450	100%	99%
210	100%	100%	460	99%	100%
220	100%	100%	470	100%	100%
230	100%	100%	480	100%	100%
240	100%	100%	490	100%	90%
250	100%	100%	500	100%	100%

Table F.1

Appendix G

Time Delay table

Time Delay 10-250 $\mu m/s$				Time Delay 260-500 $\mu m/s$			
Scan ($\mu m/s$)	Speed	Uphill	Parachuting	Scan ($\mu m/s$)	Speed	Uphill	Parachuting
10		49	49	260		43	27
20		49	49	270 (47%-53%)		36-61	54
30		57	48	280		27	53
40 (53%-47%)		49	36-61	290 (33%-67%)		42-67	51
50		49	49	300		57	48
60		40	48	310		45	43
70		38	45	320		58	62
80		36	29	330		45	55
90		60	65	340		31	47
100		49	49	350		41	37
110 (53%-47%)		62	43-68	360		51	52
120 (50%-50%)		57	36-61	370		36	42
130		37	56	380		45	55
140		56	59	390		28	42
150		40	48	400		36	29
160		42	51	410		44	66
170		38	45	420		51	52
180		29	31	430		33	37
190		41	37	440		39	46
200 (63%-37%)		49	36-61	450		46	32
210		53	55	460		27	41
220		30	45	470		58	50
230		55	58	480		63	57
240		28	42	490		43	40
250		48	47	500		48	47

Table G.1

Appendix H

Glossary

List of Acronyms

AFM	Atomic Force Microscope
AM-AFM	Amplitude Modulation Atomic Force Microscopy
DOF	Degrees of Freedom
FPGA	Field-Programmable Gate Array
GT	Ground Truth
HS-AFM	High-Speed Atomic Force Microscope
HS-FW	High-Speed Forward
LIA	Lock-In Amplifier
NI	National Instruments
PI	Proportional Integral
PID	Proportional Integral Derivative
RT VI	Real-Time Virtual Instrument
VI	Virtual Instrument